Modeling the Multi-Isotopic Separation in a Gas Centrifuge and Enrichment Cascades

---

A PhD Dissertation

Presented to

the faculty of the School of Engineering and Applied Science

University of Virginia

In partial fulfillment

Of the requirements for the degree

Doctor of Philosophy

By

Wisher Paudel

May 2022

PHD COMMITTEE MEMBERS:

DR. HOUSTON WOOD, ADVISOR (MAE)

DR. ROGER FITTRO, CHAIR (MAE)
DR. DANIEL QUINN (MAE)
DR. CHRIS GOYNE (MAE)
DR. SEAN AGNEW (MSE)

Abstract

Possibility of nuclear warfare and the misuse of nuclear technology are pressing issues of the modern times. Despite best attempts by the International Atomic Energy Agency (IAEA) to limit the use of nuclear energy to peaceful purposes, there are looming threats of nuclear proliferation on a regular basis. Therefore, it is essential to be able to understand the science and model the technology behind the production of such weapons of mass destruction and to recognize any potential threats in a timely manner. To that goal, this work looks to build upon and refine the studies that have been conducted to model the gas centrifuges used in the development of fuel required to operate power reactors as well as create nuclear weapons. Such fuel is obtained by enriching the fissile uranium-235 isotope from the uranium hexafluoride (UF_6) gas mixture inside the high-speed centrifuges.

This research focuses on the study of fluid flow and isotopic diffusion of the UF_6 gas inside the rotor volume of a gas centrifuge. The primary objective is to develop a numerical model to simulate the concentration gradients of the different uranium isotopes present in the gas mixture. Previous work in this topic has primarily looked at the separation of two isotopes, ^{235}U and ^{238}U; however, uranium also consists of the ^{232}U, ^{234}U, and the ^{236}U isotopes that can affect the separative capability of the machine. Therefore, a two-dimensional multi-isotope separation model has been created by solving the diffusion transport equations using finite element analysis. The new 2-D model is unique to its counterparts in the past as it provides a holistic view of isotope transport inside the machine for any arbitrary number of isotopes that may be present in the gas mixture. In addition to the development of the multi-isotope model, this work also looks to refine the mass flow solution, specifically by evaluating the ideal distribution shapes of the sources of mass, momentum, and energy. This ensures that the simulated mass flow is the best representation of reality as well as provides the researcher with options to model the flow as desired. To ensure that the developed numerical models provide accurate results, verification measures including sensitivity analysis and uncertainty quantification are performed. Finally, the work is extended from a single centrifuge to cascades of centrifuges to simulate gas centrifuge enrichment plants (GCEPS) and to be able to identify any proliferation threats. Thus, the last section of the dissertation highlights how the IAEA can benefit from the glossary of existing as well as newly developed models and studies during verification of declared nuclear material.

Acknowledgments

I would like to first thank my advisor, Dr. Houston Wood for not only accepting me into graduate school but also believing in me with the nuclear project. When Dr. Wood told me about this research back in 2017, it seemed a bit daunting since it was very new to me. Looking back, I am glad I chose to work on it as the past five years have flown by and the experience has been extremely rewarding. I want to thank Dr. Wood for providing me with the necessary resources, connecting me with his previous students as well as many experts on the field, and allowing me to attend courses, seminars, and conferences. I did not know I would have the opportunity to travel as much as I did in graduate school and for that I am grateful to Dr. Wood and ROMAC in general.

I would also like to give my sincerest appreciation to the dissertation committee members: Dr. Roger Fittro, Dr. Chris Goyne, Dr. Dan Quinn, and Dr. Sean Agnew. Their interests and feedback on my work have helped me tremendously over the last couple of years to define my research objectives better.

I have been fortunate enough to collaborate with folks at Pacific Northwest National Lab for the past three years. This work would not have been entirely possible without their tremendous support and resources. I must thank my mentors at PNNL, Kim Burns, David Springfels, and Brittany Robertson, who ensured that I had everything I needed to do the work, not only during my internship at the lab but also continuously after leading up to the present day. I want to thank David especially for meeting with me every week for the past two years and for providing valuable feedback and perspective on my work. I am also grateful to Alex Misner for his time reviewing my papers and talks and for helpful comments on this dissertation.

I would like to thank my colleagues at ROMAC for making MEC 105 and MEC 115 my second home for the last five years. Thanks to Neal, Xin, Nathaniel, and Pedro for their company during many hours spent at my desk. It was also great to collaborate with everyone on either course work or ROMAC related research projects. I am also especially grateful to Cori Watson-Kassa for her help and guidance during my early days of graduate school. Cori allowed me to collaborate on her research while I was still an undergraduate student and convinced me to pursue graduate studies at ROMAC, which is one of the reasons I am writing this dissertation today. And I certainly cannot forget Lori Pedersen who has helped me with countless administrative needs over the last six years or so, making my grad school experience that much better.

Finally, I would like to thank my family for their love and support, without which I could not possibly have completed a PhD. My parents, Bishnu and Saraswati, and my brother, Bikal, have always been there for me anytime I needed their advice or help both with professional and personal matters.

Lastly, I want to thank my girlfriend, Erica, for her patience, love, and encouragement. Her constant support, especially during my long hours spent in the office, is what allowed me to push on and finish the work.

I also want to acknowledge the financial assistances obtained from the graduate fellowship through Nuclear Regulatory Commission, Graduate Teaching Assistance, and contract with the Pacific Northwest National Lab that ensured I had sufficient funds to complete my degree.

List of Figures

List of Tables

Acronyms

IAEA	International Atomic Energy Agency
UF_6	Uranium Hexafluoride
GCEPs	Gas Centrifuge Enrichment Plants
HALEU	High Assay Low Enriched Uranium
NPT	Treaty on the Non-Proliferation of Nuclear Weapons
CSA	Comprehensive Safeguards Agreement
CTBT	Comprehensive Test Ban Treaty
NU	Natural Uranium
PDEs	Partial Differential Equations
FEA/M	Finite Element Analysis/ Model
UQ	Uncertainty Quantification
SA	Sensitivity Analysis
V&V	Verification and Validation
DoE	Design of Experiment
QoI	Quantity of Interest
LHS	Latin Hypercube Sampling
PDF	Probability Density Function
PCE	Polynomial Chaos Expansion
MC	Monte Carlo
LRA	Low Rank Approximation
ES	Environmental Sampling
SWU	Separative Work Unit
LEU	Low Enriched Uranium
HEU	Highly Enriched Uranium

Table of Contents

Chapter 1

Introduction

1.1 History of Nuclear Weapons

The era of nuclear power and its unimaginable impact began roughly around Christmas time in 1938. Austrian physicist Lise Meitner, along with her nephew Otto Frisch, successfully explained the phenomenon observed by Meitner's fellow colleagues Otto Hahn and Fritz Strassman, who upon bombarding uranium with neutrons found isotopes of barium among the decay products [1]. Meitner and Frisch were able to determine that this observation was a result of the neutrons splitting the uranium atom, the process that came to be known as the nuclear fission. Soon after the discovery, it became apparent in the scientific community that the fission process could be controlled to initiate a chain reaction and in turn release enormous amount of energy. This revolutionary finding thus quickly became a dangerous weapon given the state of the world at the time.

The race to acquire energy from nuclear fission and develop destructive weapons accelerated at a rapid pace during World War II. Following the Japanese attack in Pearl Harbor and the United States' entry into the war, President Roosevelt authorized the formation of the Manhattan Project with the goal of combining research efforts to weaponize nuclear energy. The United States conducted its first nuclear test in July 1945 and subsequently dropped two atomic bombs on the cities of Hiroshima and Nagasaki in August 1945 that killed more than 100,000 people and leveled the two cities to ground. Following the conclusion of the war, the U.S. had hoped to keep its secrets of nuclear weapons; however, those secrets including the processes and the technology for building the atomic bomb quickly spread. By 1949, the Soviet Union conducted its first nuclear test, followed by the United Kingdom (1952), France (1960), and China (1964) [2] .

It became apparent that international efforts were necessary to prevent the threatening proliferation of nuclear weapons. In 1953, President Dwight D. Eisenhower addressed the general assembly of the United Nations urging the increasingly divided world to use "Atoms for Peace" and highlighting the necessity of an organization "to apply atomic energy to the needs of …peaceful activities [3] ." The speech led to the formation of the International Atomic Energy Agency (IAEA) and helped shape the agency's statute, which was unanimously approved by 81 nations in 1956. The primary objectives of the IAEA are "to accelerate and enlarge the contribution of atomic energy to peace, health, and prosperity" and to establish and apply safeguards to ensure that the nuclear technology is “not used in a way to further military purposes [4].”

As IAEA looked to establish its foothold in the nuclear realm for the decade following its inception, the United States and dozens of like-minded countries negotiated the Treaty on the Non-Proliferation of Nuclear Weapons (NPT) in 1968 [5]. The NPT entered into force in March 1970 and includes a total of 190 states-parties [6]. Under the NPT, non-nuclear-weapons States have agreed not to manufacture or acquire nuclear weapons while the nuclear-weapons States have committed not to assist any non-nuclear-weapons States to create or obtain such weapons. There are five nuclear-weapons States that are defined as the countries that manufactured and tested nuclear weapons or other nuclear explosive devices prior to the treaty. Along with the United States, these include the four nations mentioned above in China, France, Russia, and the United Kingdom. Under Article III of the NPT, each non-nuclear weapons state is required to sign a comprehensive safeguards agreement (CSA) with the IAEA which allows the agency to verify the states’ obligations under the Treaty and prevent diversion of nuclear energy from peaceful uses to weapons development. The countries that remain outside the Treaty are South Sudan, India, Israel, and Pakistan. The Democratic People’s Republic of Korea (DPRK) signed the Treaty in 1985; however, was found to be in non-compliance with its safeguards agreement in 1993 [7]. It eventually announced its withdrawal from the NPT in 2003. Per Article X of the NPT, party withdrawing from the treaty is required to notify all other parties three months in advance. There is not a consensus among the NPT parties and the DPRK on its actions and withdrawal methods, making it unclear whether the state has officially become a non-member [8]. The treaty was extended indefinitely in 1995 and calls for a review conference every five years to detail the progress being made and areas that require further improvements. To ensure that all the parties of the treaty fulfill their obligations, the IAEA assumes the specific role as an international safeguards inspectorate. The agency is primarily tasked with reviewing information provided by a State regarding the design of a facility and inspecting nuclear material inventory and facility operation.

The main purpose of safeguards is the timely detection of diversion of nuclear material. Depending on the State, the IAEA’s safeguards agreements can vary in their breadth, frequency, and verification methods. While the non-nuclear states are required to be part of the safeguards agreements under the NPT, the five weapon states have Voluntary Offer Safeguards Agreements in place that allow IAEA to safeguard nuclear materials in specific facilities offered by the State. The three out of four countries that are not part of the NPT- India, Pakistan, and Israel- have entered into the items-specific agreements with the IAEA. The large part of the Agency's verification methods involves nuclear material accountancy, the process of confirming the inventory of declared nuclear material. The IAEA also makes use of surveillance and containment measures such as utilizing seals to secure products and equipment for further analysis and security cameras for remote monitoring. These techniques are applied by carrying out on-site inspections at all declared nuclear facilities in a State. While such safeguards measures have traditionally been effective, there are also cases where particular States were able to elude the Agency and initiate undeclared clandestine operations including Iraq throughout the 1970s and 1980s [9] and Iran in the early 2000s [10]. The IAEA has since invested and relied on research and development to improve the safeguards approaches and technology. The overall goal of this particular research is to contribute to those research efforts and further upgrade IAEA's current capabilities.

Other international efforts to assist nuclear non-proliferation include the negotiation of the Comprehensive Test Ban Treaty (CTBT) in 1996 which seeks to prohibit any nuclear weapon test. The treaty has been signed by 185 nations; however, it has not and cannot enter into force until the five original nuclear weapons states as well as the non-signatories of the NPT ratify it [11] . More specifically regarding the safeguards, in 1997, the IAEA Board of Governors approved the Additional Protocol providing IAEA wide range of access to facilities to detect the presence of undeclared nuclear material and activities [12]. The IAEA as well as the international community in general are frequently analyzing the effectiveness of current treaties and safeguards measures to limit and/or decrease the number of nuclear weapons.

1.2 Nuclear Fuel Cycle

Before beginning the discussion on the key objectives of this work and how they align with non-proliferation, it is essential to provide a brief background on the nuclear fuel cycle. To understand how the nuclear fuel functions, the concept of fission needs to be defined further. The fission reaction occurs when a heavy nucleus splits spontaneously or on impact with another particle releasing free neutrons, gamma rays, and large amount of energy [13]. Some of the heavier atoms, those with atomic number, Z >100, can undergo fission on their own spontaneously; however, only specific nuclei including the isotopes ^{233}U and ^{235}U of uranium and ^{239}Pu of plutonium can sustain a fission chain reaction. These nuclei release neutrons when they split apart that can further induce fission of other nuclei. By controlling such a chain reaction, the nuclear power reactors harness energy required to generate electricity. The most common naturally occurring isotope that has a high fission probability is Uranium-235.

There are a series of steps required to obtain, process, utilize, and dispose of such fissile uranium material collectively known as the nuclear fuel cycle as shown in Figure 1.1. The cycle can be categorized into two separate branches based on their end goals. The front-end steps involve preparing uranium for use in nuclear reactors while the back-end steps feature managing the disposal of used or spent nuclear fuel. The front-end process begins with the extraction or mining of the uranium ore to produce the ore concentrate, U_3O_8, commonly referred to as "yellow cake." The ore concentrate is then converted to uranium hexafluoride (UF_6) gas, which is sent to an enrichment facility to increase the concentration of the fissile ^{235}U isotope. While there are nuclear reactor designs that use natural uranium as fuel, such as the pressurized heavy water reactor (PHWR) or CANDU as known in Canada, majority of the reactors in the world today require enriched uranium fuel with ^{235}U concentration between 3-5% [14]. UF_6 is the most convenient gaseous compound of uranium since it has a high vapor pressure at modest temperatures, and the fluorine gas only has one stable and naturally occurring isotope that exists in greater than trace quantities. Some of the physical properties of the gas compound at three different temperature values are listed in Table 1.1.

Table 1.1: Key physical properties of UF_6 gas [15]

Temperature (K)	273	300	323
Vapor pressure (torr)	17.7	128	527
Viscosity $(\eta)(\frac{Ns}{m^2})$	1.58e-5	1.72e-5	1.84e-5
Schmidt number $(\frac{\eta}{\rho D})$	0.79	0.79	0.79
Specific heat ratio (γ)	1.0704	1.0687	1.0666
Thermal conductivity $\left(\frac{W}{m*°\mathrm{C}}\right)$	61.1e-4	68.0e-4	73.9e-4

In its natural state, uranium contains 99.3% ^{238}U isotope and about 0.7% ^{235}U. To create fuel required for the reactors, Natural Uranium (NU) needs to be enriched in the 235-isotope up to 3-5%. One of the most popular methods to achieve enrichment is through gas centrifuges. It is imperative to understand and monitor this enrichment process since the same process that is used to create fuel for power reactors can also be used to enrich ^{235}U to weapons grade (> 90%). This makes the enrichment process a sensitive stage of the nuclear fuel cycle and is the primary focus of this work.

Once the uranium is enriched, it is cooled and allowed to solidify before being transported to reactor fuel assembly plant and converted into nuclear fuel. The solid UF_6 is heated and converted back to its gaseous form and chemically processed to uranium dioxide (UO_2) powder. The powder is compressed to create fuel pellets that are further stacked and sealed into metal tubes to form fuel rods. The fuel rods are then gathered together to construct a fuel assembly that allows the nuclear reaction to begin in the reactor core. After their use in the reactor, the fuel assemblies become highly radioactive and are removed and stored under water at the reactor site for several years. Once "cooled" in a few years' time, they are often sent for final storage in a permanent underground repository in many countries. The safe long-term treatment and disposal of nuclear waste is an ongoing area of research. In between the temporary storage on site and final disposition, the spent fuel can be reprocessed to obtain either uranium or plutonium for further enrichment and fuel fabrication [16]. While the reprocessing of spent fuel is not currently carried out in the United States, it is important to understand the effects of spent fuel on the other aspects of the cycle. To that end, the analysis within this dissertation will not only study the enrichment of natural uranium but also the spent reactor fuel.

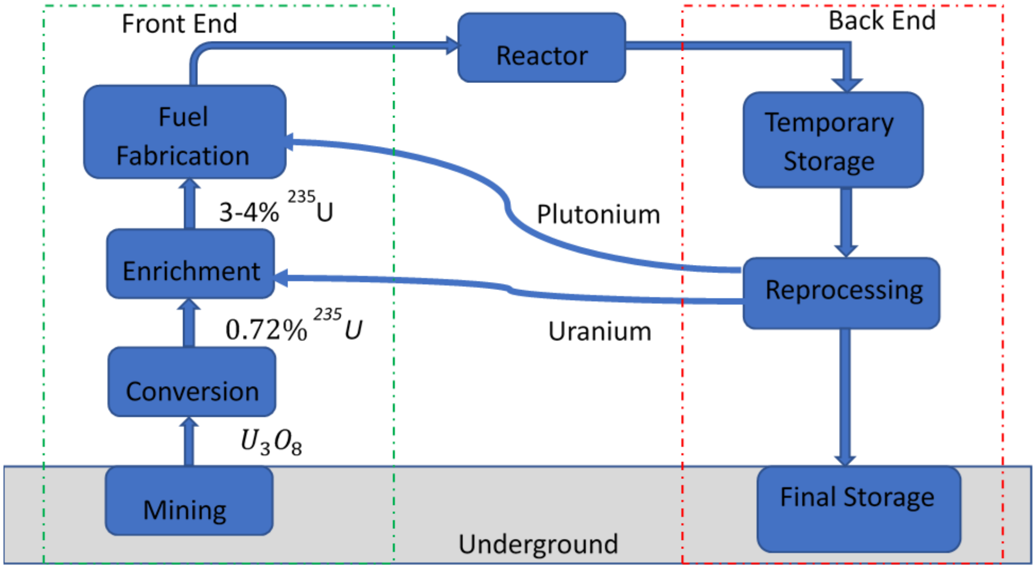

Figure 1.1: Nuclear fuel cycle entails obtaining, preparing, applying, and safely discarding radioactive nuclear fuel

1.3 Gas Centrifuge

Gas centrifugation is currently the most popular as well as more efficient method compared to the gaseous diffusion and electromagnetic processes used during World War II for separating and enriching desired isotopes. Gaseous diffusion method utilizes molecular diffusion through a porous barrier to separate the components of gas mixtures. This process was developed at a large-scale in the US to produce highly enriched uranium during World War II as part of the US Manhattan Project [17] [18]. Gaseous diffusion required many stages and significant amount of electrical power during operation to achieve desired enrichment. Because of this inefficiency and high associated cost, this process lost popularity over the years as technological advances were made to pursue alternative methods such as gas centrifuge.

The Manhattan Project also considered the technique of electromagnetic separation to isolate and collect ^{235}U. A device dubbed "calutron" was developed by Ernest Lawrence in 1941 that operated on the principles of mass spectrometry [19]. The technology was adopted by the U.S. government and utilized to produce enriched uranium needed for the bomb. Nonetheless, after the war, the slow enrichment process and continued maintenance issues with the technology saw the abandonment of the electromagnetic method, with preference given to gaseous diffusion.

Other isotope separation approaches that have been investigated include aerodynamic methods such as separation nozzles [20] and laser separation including Atomic Vapor Laser Isotope Separation (AVLIS) and Molecular Laser Isotope Separation (MLIS) [21]. Despite these technologies, gas centrifuges are still considered to provide the best combination of economic feasibility and efficiency.

The separation of isotopes by gas centrifuges was first discussed by Frederick Lindemann and Francis Aston in 1919 [22] . However, the first successful experiment was not conducted until 1934 by Professor Jesse Beams at the University of Virginia with the isotopes of chlorine. While Beams and his research cohort continued their centrifuge work throughout World War II as part of the Manhattan Project, the technology was not used in the war effort due to the lack of mechanically reliable high-speed bearings required for the machine at the time [23]. Following the war, the work on gas centrifuges continued, particularly in the USSR. An Austrian prisoner of war named Gernot Zippe suggested a pivot-magnetic bearing combination that proved efficient for high-speed operation and were implemented in the Soviet designs. Zippe was eventually released in 1956 and brought to the United States where he continued his work at the University of Virginia [24]. Zippe's work paved the way for the development of advanced gas centrifuges in the US as well as in Europe. Over the next several decades, gas centrifuge enrichment plants were built in many countries pursuing uranium enrichment, and thus centrifugation became a conventional method of operation worldwide.

The gas centrifuge achieves isotopic separation by the action of a centrifugal force field approximately 10^5 times greater than gravity. It is essentially a hollow rotor that is spun rapidly about its axis creating a large pressure gradient between the axis and the wall. The cross-sectional image of a nominal centrifuge is presented on Figure 1.2.

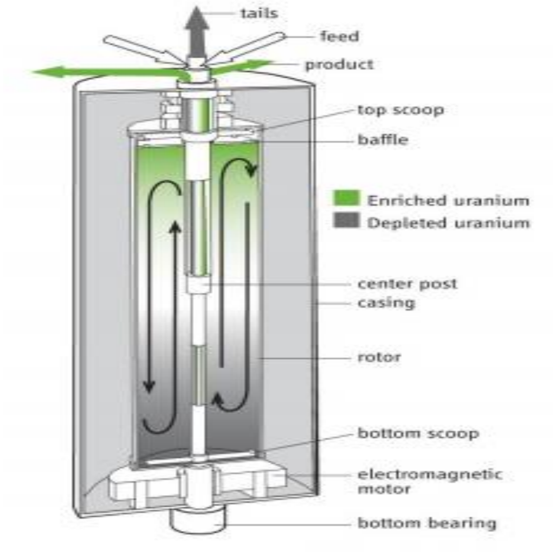

Figure 1.2: Cross-section of a typical countercurrent gas centrifuge showing flows into and out of the rotor [25]

During the uranium enrichment process, UF_6 gas is fed into the centrifuge rotor near the axis through a feed pipe and is removed using scoops with more ^{235}U on one end and more ^{238}U on the other. The top scoop is shielded from the separation chamber of the rotor by a baffle, which is a rotating perforated disk as shown in Figure 1.2. The outside surface of the centrifuge rotor is travelling at very high speeds, so it is enclosed in a vacuum casing to minimize drag. The casing can also contain an exploding or failing rotor. The vacuum inside is often maintained using molecular pumps that consists of smooth cylinder made of UF_6 resistant material with spiral grooves attached to the inside of the casing close to the rotor. The spiral grooves act as an effective mechanical seal channeling molecules away from the low-pressure end to the high-pressure end, thus reducing leakage of gas. Bearings are used on each end in order to constrain the rotor to spin about a specific position and reduce mass unbalance and mechanical vibrations. Most modern centrifuge designs use magnetic bearings that greatly reduce wear and energy consumption.

There exist various types of centrifuges characterized based on their functionality including the evaporative, concurrent, and countercurrent types. In an evaporative centrifuge, small drop of liquid is sent inside the rotor which forms a layer at the wall and creates a pool of isotopic mixture. A shaft located along the axis is used to remove the vapor consisting of the lighter isotope during operation. The pool of residual liquid at the wall contains the heavier isotopes in greater concentrations [26]. The evaporative centrifuge is not easily adaptable to continuous separation of desired isotopic mixtures since it operates by a batch process. In the concurrent method of gas centrifugation, the gas mixture is introduced at one end of the rotor and extracted from two streams at the other end, one near the axis and other near the wall. The isotopic concentrations of the two streams vary during operation, tending towards the radial equilibrium distribution [27]. The concurrent centrifuges require large feed flux and thus significant amount of power to achieve desired separation. Because of its ability to significantly improve the separation effect, the countercurrent gas centrifuge has been the preferred method for isotope separation and is the focus of this dissertation.

In the countercurrent centrifuge, the gas flow represents a perturbation to the isothermal solid-body rotation which can be driven by a combination of external, mechanical, and thermal drives. The external drive can be established through the introduction of material at the axis and withdrawal at the top and bottom of the centrifuge. The mechanical drive can occur if the end caps are rotated at different speeds from that of the centrifuge rotor or can result from the drag force exerted by the stationary scoop at the bottom. The thermal drive can be created by establishing a temperature gradient between the top and bottom end caps. These physical mechanisms force a countercurrent flow pattern inducing an axial and convective mass flux, which in turn increases the separation capabilities of the machine.

The radial pressure gradient allows the heavier isotope of uranium, ^{238}U to be concentrated near the wall and the lighter ^{235}U molecules to be concentrated near the axis as seen in Figure 1.3. However, the separation in the radial direction is quite small since the majority of the gas is confined very close to the rotor wall. In order to substantially increase the degree of separation, a circulating flow along the length of the centrifuge can be created. If one end of the centrifuge is heated, the warmer gas will rise and flow toward the opposite end along the axis, while the cooler gas will flow in along the wall to replace it. Additionally, the bottom scoop used for removing depleted material can slow the flow of gas, reducing the centrifugal force and allowing the gas to rise. As seen in Figure 1.4, these factors will thus allow the flow in the centrifuge up the center and down along the wall, creating an axial separation of lighter and heavier isotopes.

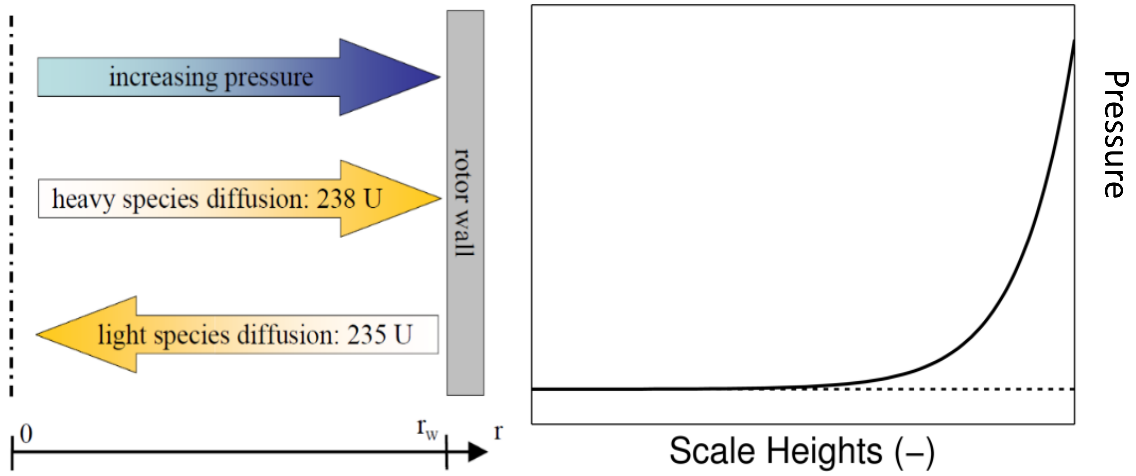

Figure 1.3: The radial separation of the lighter and heavier isotopes in the gas centrifuge rotor is dictated by the pressure gradient

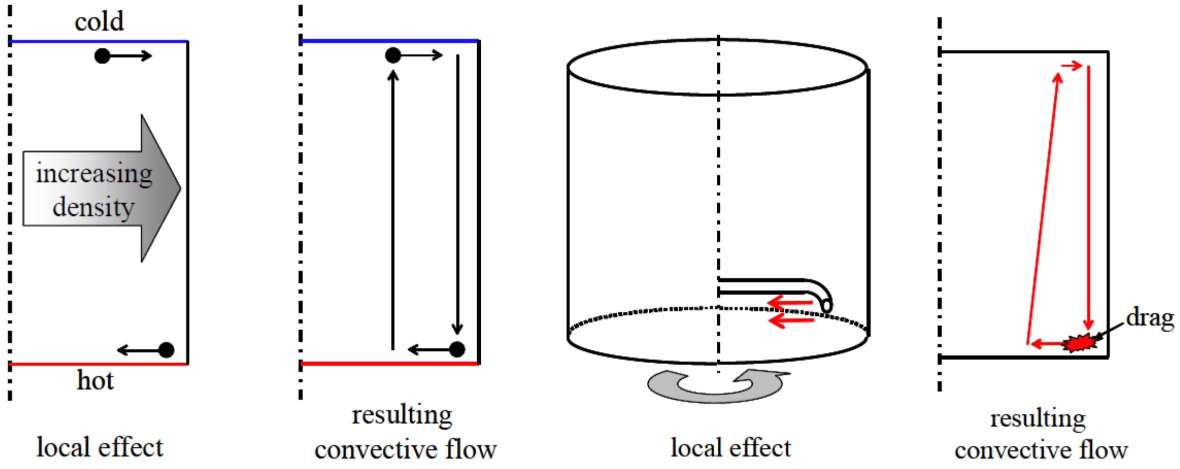

Figure 1.4: The axial separation of isotopes can be induced by creating a counter-current flow as a result of axial temperature gradient and scoop drag. (Fig. 1.3 and 1.4 taken from Doneddu Nov. 2004) [28]

The separative capability of a single centrifuge is not sufficient to mass produce enriched nuclear fuel required for power reactors. In practice, centrifuges are linked together in parallel and series to increase material throughput and enrichment and such arrangements is referred to as a cascade as shown in Figure 1.5. The centrifuges connected in parallel are collectively referred to as a stage. The cascade is divided into two sections, the enriching section where the desired product is extracted and the stripping section where the gas depleted in the ^{235}U isotope is collected. The enriching section includes the feed stage and all of the stages above while the stripping section includes the stages below the feed stage.

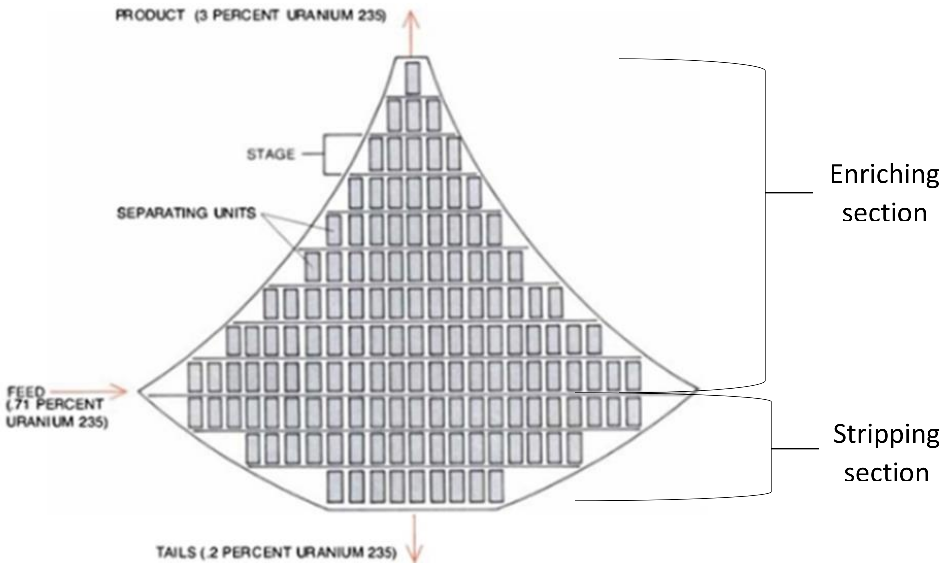

Figure 1.5: Arrangement of gas centrifuges in a 12-stage ideal cascade [29]

1.4 Objectives of the dissertation

Since gas centrifuges are presently the most widely used technology for uranium enrichment, it is important to add to literature the new methodologies and approaches in analyzing the fluid dynamics and isotopic diffusion in the interior regions of the machine. Keeping that in mind, this work looks to develop modeling tools to provide qualitative and quantitative understanding of the machine's functionality required to accurately evaluate a particular state's enrichment capability. This work looks to upgrade previously developed models, develop entirely new model, and ensure its validity, and apply the results to study various facility level scenarios. The main motivations and objectives of this work are summarized as follows:

1. Motivation: The numerical models calculating the UF_6 mass flow inside the centrifuge rotor do not explain the choice of mathematical functions used to represent the sources and sinks of mass, momentum, and energy.

Objective: Modify the mass flow solution to adapt to various types of functions for sources and sinks and quantify and identify the differences to justify the choice.

2. Motivation: The current open-source solutions of the diffusion equations inside a centrifuge rotor are limited to 1-D or 2-D binary mixtures. A more comprehensive solution can provide a holistic view of the isotopics inside the machine.

Objective: Develop a numerical model to solve 2-D multicomponent isotope diffusion in a gas centrifuge for any physical and operational parameters.

3. Motivation: There are no known open-source experimental data regarding the multi-component separation of uranium isotopes. This limits the options to validate the numerical models in literature.

Objective: Develop a methodology to perform sensitivity analysis and uncertainty quantification on the developed multi-component separation model to verify and validate the output of the code.

4. Motivation: There are limited studies in literature for the higher enriched nuclear fuel known as High Assay Low Enriched Uranium (HALEU) required for emerging advanced reactors that investigate the safeguards implications of such enrichment at Gas Centrifuge Enrichment Plants (GCEPs).

Objective: Develop a HALEU cascade based on centrifuge performance data from the new higher fidelity code and study the isotopic changes for several unintentional and intentional misuse scenarios.

To address these four key objectives, the dissertation is organized into seven chapters. Here are the summary of the chapters that make up this work.

Chapter 1: Introduction

The nuclear non-proliferation is explained through historical context and the nuclear fuel cycle. The brief background on the gas centrifuge machine is provided to highlight the motivations behind this work.

Chapter 2: Mass flow and isotopic diffusion inside a gas centrifuge

This chapter focuses specifically on the physics and mathematical derivations involved in defining the bulk mass flow as well as the diffusion of individual isotopes.

Chapter 3: Modeling the sources and sinks

Four different shape functions are used to define the sources and sinks of mass, momentum, and energy. Using the previously developed mass flow solution, the four functions are compared in terms of their results for flow streamlines and isotopic concentration distributions.

Chapter 4: Finite element solution of the 2-D multi-component diffusion equations

Detail discretization and finite element derivations of the diffusion equation are provided along with sample results for fictitious centrifuges.

Chapter 5: Sensitivity analysis and uncertainty quantification of the FEM model

A methodology to perform parametric study for sensitivity analysis is developed and the propagation of uncertainty from input parameters to the output is quantified using Matlab's open source UQLab module.

Chapter 6: High fidelity centrifuge and cascade model to study HALEU cascade

The single centrifuge performance is compared against the results obtained using previous 1-D solution. A HALEU cascade is designed using the new performance data and potential proliferation scenarios are compared against unexpected operational mishaps at a particular fictitious facility.

Chapter 7: Conclusions

The overall objectives of the research work are re-iterated and general findings are summarized. The impact of the work is highlighted, and potential future research topics are identified.

Chapter 2

Mass Flow and Isotopic Diffusion inside a Gas Centrifuge Rotor

2.1 Overview

As mentioned in Chapter 1 section 3, a comprehensive model of the interior of gas centrifuge includes set of equations detailing the fluid dynamics of the countercurrent motion as well as the diffusion equations derived for individual isotopes of the gas mixture. The solution of the gas dynamics provides average mass velocity, density, and temperature of the mixture, which are then applied in the solution of the isotopic diffusion. This chapter will walk through the theoretical work on the mass flow and diffusion inside a single centrifuge rotor. Following the derivations required to bolster the single machine discussions in the following chapters is an overview of the theory on the centrifuge enrichment cascades. The initial work on the hydrodynamics inside a gas centrifuge included numerous assumptions and analytical methods. It is beyond the scope of this dissertation to discuss all of those works. The interested readers are encouraged to refer to Soubbaramayer for his exhaustive review [30]. The focus here is on the use of boundary layer theory to formulate equations describing the flow field in rotating gases and numerical methods to solve those equations.

2.2 Theory of mass flow

The principle effort on boundary layer theory in gas centrifuge began in 1961 by a group led by Lars Onsager as a covert project under the United States Atomic Energy Commission [31]. Considering a cylindrical coordinate system, (r, θ, z), the complete set of governing equations in fluid dynamics includes the conservation of mass, momentum, energy, and state. Since the full set of these equations is nonlinear and complex, a simplified assumption that the flow can be separated into a base state, rigid body rotational flow, and a linearly perturbed flow was made. After linearization, the set of equations were non-dimensionalized as highlighted in Wood & Morton [32]. Next, the Onsager model separated the flow into two primary regions, the internal flow regions (includes the Stewartson [33] and the inner core region and the Ekman layers [34] at the top and the bottom as shown in Figure 2.1. The internal region is a vacuum where the molecular motions are governed by equations of rarefied gas dynamics, for example the Boltzmann Equation. Since there is no mass present there, it does not affect the isotopic separation. Therefore, the axial diffusion of heat and momentum are negligible and thus the associated terms are eliminated.

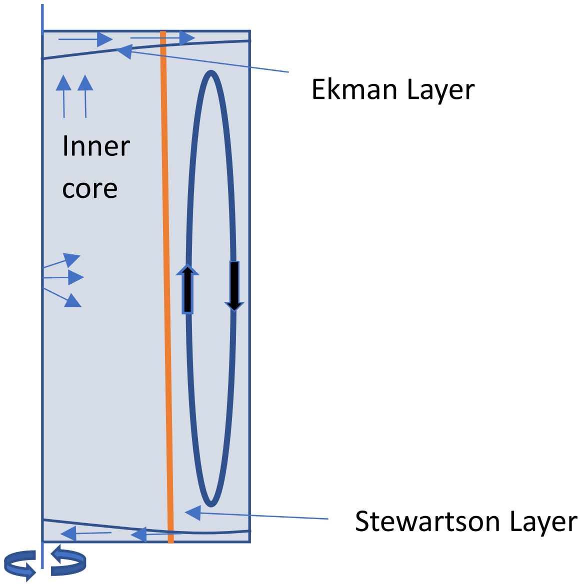

Figure 2.1: Boundary layers and flow diagram in the gas centrifuge rotor. Boundary at the top and bottom endcaps are given by thin Ekman layers and near the side wall by Stewartson layer

The effects of sources and sinks of mass, momentum, and energy interior to the fluid as well as on the boundaries were considered by including the source terms. Following Wood and Morton [32], the final equations with the source terms can be manipulated to form a single partial differential equation in terms of a master potential function, $\mathcal{X}$.

$$(e^x(e^x\mathcal{X}_{xx})_{xx})_{xx} + B^2\mathcal{X}_{yy} = F(x,y) \qquad (2.1)$$

where

$$F(x,y) = \frac{B^2A^2}{2ReS}\int_x^\infty (\mathcal{J}_y - 2\mathcal{V}_y)dx' - \frac{B^2}{4A^4}\int_x^\infty \int_0^{x'} (M_y dx"dx' - \frac{B^2A^2}{2ReS}\left[\left(e^x\mathcal{U}_y\right)_x + (e^x\mathcal{W})_{xx}\right] \qquad (2.2)$$

And

$x = A^2(1-\eta^2), \eta = \frac{r}{a} \rightarrow non - dimensionalized\ radial\ variable,$

$A = \frac{a\Omega}{(2RT_o)^{\frac{1}{2}}}, R = the\ specific\ gas\ constant, T_0 = uniform\ gas\ temperature,$

$a = radius\ of\ the\ centrifuge\ rotor, \Omega = angular\ velocity\ of\ the\ centrfuge\ rotor,$

$B = \frac{ReS^{\frac{1}{2}}}{4A^6}, Re = \ the\ Reynolds\ number,$

$S = 1 + \frac{PrA^2(\gamma-1)}{2\gamma},\ \gamma = \ the\ ratio\ of\ specific\ heats,$

$Pr = \frac{C_p\mu}{k}\ is\ the\ Prandtl\ number\ and\ C_p\ is\ the\ specific\ heat\ at\ constant\ pressure,$
$\mu\ is\ the\ viscosity\ of\ the\ gas, and\ k\ is\ its\ thermal\ conductivity$

Here, *M, U, V, W*, and *J* are sources and sinks of mass, radial momentum, angular momentum, axial momentum, and energy respectively. These terms are used to account for the presence of a scoop and the addition and withdrawal of gas.

A complete derivation and discussion of Equation (2.1) can be found in numerous articles including Wood & Morton [32], Babarsky & Wood [35], Wood & Sanders [36], and Wood, Jordan, and Gunzburger [37]. These equations have been approximately solved by a variety of techniques, including eigenfunction-expansion methods (Wood & Morton [32]), finite difference methods (Viecelli [38]), and finite-element methods (Gunzburger & Wood [39], Gunzburger, Wood, and Jordan [40], Bourn, Peterson, and Wood [41], Witt [42], and Thomas [43]). The flow models developed in [42] and [43] are used to determine the mass flux profile required as input to the isotope diffusion equations solved in this work.

Equation (2.1) does not take the curvature of the centrifuge rotor into account and is known to make the “pancake” approximation, which holds true for machines operating at high speeds. The effects of curvature are prominent at slower rotor speeds. In order to account for such cases, most of the theoretical work involving the addition of rotor curvature to Equation (2.1) was completed first by Maslen in 1979 [44] [45]. The modified version of the Onsager’s equation that includes these effects is often known as the Onsager-Maslen equation. Most recently, Witt obtained a numerical finite element solution of the Onsager-Maslen equation combined with sources terms described above to model the introduction and withdrawal of feed gas [42]. The updated flow equation with the inclusion of radial term to apply curvature effects can be written as

$$(e^{x}(\eta^{2}(e^{x}\mathcal{X}_{xx})_{x})_{x})_{xx}+\frac{Re^{2}}{16A^{12}Z^{2}}*\frac{\left(1+\widehat{K}\eta^{2}\right)}{\eta^{4}}\,\mathcal{X}_{yy}=\bar{S}+\overline{H} \tag{2.3}$$

where $Z=\frac{L}{a}$ *is the aspect ratio, L the cylinder length, and* $\widehat{K}$ *the Brinkmann number defined as*

$$\widehat{K}=\frac{a^{2}\Omega^{2}Pr}{4*C_{P}*T_{0}} \tag{2.4}$$

$\bar{S}$ and $\overline{H}$ are obtained by Witt in [42] as

$$\bar{S} = -\frac{Re^2}{64A^{16}Z^2} * \frac{\left(1+\widehat{K}\eta^2\right)}{\eta^4} \int_x^{x_T}\int_0^{x'} M_y dx''dx' - \frac{Re}{32A^{10}Z^2} * \left(\frac{e^x}{\eta} * U_y\right)_x$$
$$-\frac{Re^2}{64A^{14}Z^2} * \left(\frac{1}{\eta^4}\right)\int_x^{x_T} \eta' V_y dx' - \frac{Re}{16A^8Z} * (e^x W)_{xx} + \frac{Re^2\widehat{K}}{32A^{14}Z^2} * \left(\frac{1}{\eta^2}\right) * \int_x^{x_T} J_y dx'$$
$$-\frac{1}{48A^8Z^2} * \left(e^{2x}M_y\right)_x + \frac{1}{16A^8Z^2} * \left(\frac{e^x}{\eta} * \left(\eta^2\left(\frac{e^x}{\eta}\int_0^x M_y dx'\right)_x\right)_x\right)_x + \frac{1}{64A^{12}Z^4} * \left(\frac{e^{2x}}{\eta^2} * \int_0^x M_{yyy} dx'\right)_x$$
$$-\frac{1}{64A^{12}Z^2} * \left(\left(1 + \frac{4A^4\eta^4}{3}\right) * \frac{e^{2x}}{\eta^4} * \int_0^x M_y dx'\right)_x \qquad (2.5)$$

$$\overline{H} = -\frac{h(y)}{x_T^2} * (e^x(n^2(xe^x)_x)_x)_{xx} - \frac{Re^2}{48A^{12}Z^2} * \frac{\left(1 \;+\; \widehat{K}\eta^2\right)}{\eta^4}$$
$$* \frac{x^3 - x_T^3}{x_T^2} h''(y) \qquad (2.6)$$

where *h* is defined as

$$h(y) = \frac{1}{4A^4Z} * \int_0^{x_T} \bar{\rho}\bar{v}_Z(x,0)\, dx' + \frac{1}{2A^2}\eta(x_T, y)\int_0^y f(y')\, dy' + \frac{1}{4A^4} * \int_0^{x_T}\int_0^y M\, dy'dx' \qquad (2.7)$$

In Equations (2.5) - (2.7), x_T is the inner non-dimensional radial boundary or “top of the atmosphere,” which is chosen large enough to be independent of the solution. In most literature, $x_T = 15$ is considered sufficiently large and is the value used in the models developed here. The term ρv_z in Equation (2.7) represents the axial mass flux that is a key parameter required for the solution of the diffusion equation as will be discussed in the next section. Equations (2.3) - (2.7) describe the necessary physics of the fluid flow in the two-dimensional cross section of the gas centrifuge rotor.

Since Equation (2.3) is a sixth-order, partial differential equation, it requires six boundary conditions in the radial direction and two in the axial directions. The boundaries are located at the rotor wall, the “top of the atmosphere” towards the axis, and at the top and bottom end caps. At the rotor wall (x=0), there is no axial velocity because of the no-slip condition and no radial velocity since there cannot be mass flux through the rotor wall. A fixed temperature gradient is assigned at the rotor wall to help maintain the countercurrent motion. At the top of the atmosphere ($x=x_T$), there is no radial velocity, no radial gradient of axial velocity and temperature, and no change in the axial and circumferential components of velocity with radial position. In the near surface region of the top and the bottom end caps, Ekman boundary layers develop. The flow is considered radial in the Ekman layers and is described by the Carrier-Maslen boundary conditions as obtained in [42].

As mentioned, the solution of fluid dynamics exists in numerous forms in literature. The models used in this dissertation follow the finite element derivation of Equation (2.3) based on the work of authors previously discussed. The Galerkin finite element method (FEM) is used to solve the sixth order Onsager-

Maslen partial differential equation. The derivation begins with the definition of a residual, *R*, for a set of discrete points in the domain that can be expressed as

$$(e^{x}(\eta^{2}(e^{x}\mathcal{X}_{xx})_{x})_{x})_{xx}+\frac{Re^{2}}{16A^{12}Z^{2}}*\frac{\left(1+\widehat{K}\eta^{2}\right)}{\eta^{4}}\,\mathcal{X}_{yy}-\bar{S}-\bar{H}=\Re(\mathrm{x},\mathrm{y}) \tag{2.8}$$

The weak form, a relaxed version of the PDE reduced to a lesser degree, can be developed by multiplying Equation (2.8) by a smooth "weighted" function, $\widetilde{\mathcal{X}}$ and setting the residual to go to zero when integrated over the domain:

$$\iint_{x=0,y=0}^{x=x_T,y=1}\widetilde{\mathcal{X}}*\left[(e^{x}(\eta^{2}(e^{x}\mathcal{X}_{xx})_{x})_{x})_{xx}+\frac{Re^{2}}{16A^{12}Z^{2}}*\frac{\left(1+\widehat{K}\eta^{2}\right)}{\eta^{4}}\,\mathcal{X}_{yy}-\bar{S}-\bar{H}\right]dydx=\ 0 \tag{2.9}$$

Following some lengthy algebraic manipulations and applying integrations by parts along with the previously defined boundary conditions, Equation (2.9) is simplified as

$$B\left(\mathcal{X},\widetilde{\mathcal{X}}\right)=F\left(\widetilde{\mathcal{X}}\right) \tag{2.10}$$

where

$$\begin{aligned}B\left(\mathcal{X},\widetilde{\mathcal{X}}\right)=&\int_{0}^{x_T}\int_{0}^{1}\eta^{2}(e^{x}\mathcal{X}_{xx})_{x}\left(e^{x}\,\widetilde{\mathcal{X}}_{xx}\right)_{x}dy\,dx+\int_{0}^{x_T}\int_{0}^{1}\frac{Re^{2}}{16A^{12}Z^{2}}*\frac{\left(1+\widehat{K}\eta^{2}\right)}{\eta^{4}}*\mathcal{X}_{y}\,\widetilde{\mathcal{X}}_{y}\,dy\,dx\\&+\int_{0}^{x_T}\frac{\left(1+\widehat{K}\eta^{2}\right)^{\frac{3}{4}}}{\eta^{4}}e^{\frac{x}{2}}*\left(\mathcal{X}_{x}\,\widetilde{\mathcal{X}}_{x}|_{y=0}+\mathcal{X}_{x}\,\widetilde{\mathcal{X}}_{x}|_{y=1}\right)dx\end{aligned} \tag{2.11}$$

$$\begin{aligned}F\left(\widetilde{\mathcal{X}}\right)=&-\textstyle\int_{0}^{x_T}\int_{0}^{1}\widetilde{\mathcal{X}}\,\tilde{S}\,dy\,dx-\int_{0}^{x_T}\int_{0}^{1}\widetilde{\mathcal{X}}H\,dy\,dx-\frac{Re}{32A^{10}Z^{2}}\int_{0}^{1}\widetilde{\mathcal{X}}\,|_{x=0}\theta(y)dy\\&+\textstyle\int_{0}^{x_T}\left[\widetilde{\mathcal{X}}|_{y=1}G^{+}(x)-\widetilde{\mathcal{X}}|_{y=0}G^{-}(x)\right]dx\ +\left(10*\frac{\left(1-\frac{1}{A^{2}}\right)}{x_T^{2}}\right)\int_{0}^{1}\widetilde{\mathcal{X}}|_{x=0}h(y)dy\\&-\textstyle\left(2*\frac{(x_T+1)}{x_T^{2}}\right)e^{2x_T}*\int_{0}^{1}\eta^{2}\widetilde{\mathcal{X}}_{xx}|_{x=x_T}h(y)dy\end{aligned} \tag{2.12}$$

$G^{+[-]}(x)$ in Equation (2.12) is acquired from the Carrier-Maslen boundary conditions at the top and the bottom end caps and are given by:

$$\begin{aligned} G^{+[-]}(x) = &-\left(\frac{Re^2}{48A^{12}x_T^2Z^2} * \frac{\left(1+\widehat{K}\eta^2\right)}{\eta^4}\right) * (x^3 - x_T^3)h'(1[0]) \\ &+[-]\frac{Re^{\frac{3}{2}}}{4A^8x_T^2Z} * \left(\frac{\partial}{\partial x} * \frac{\left(1+\widehat{K}\eta^2\right)^{\frac{3}{4}}}{\eta^2}\, x^2 e^{\frac{x}{2}}\right) h(1[0]) + \frac{Re}{16A^{10}Z^2} * \frac{\partial}{\partial x}\left(\sqrt{\left(\frac{\left(1+\widehat{K}\eta^2\right)}{\eta}\right)}\, v_r^{+[-]}\right) \\ &-\frac{Re}{32A^{10}Z^2} * \left(\frac{\partial \phi^{+[-]}}{\partial x}\right) + [-]\frac{Re^{\frac{3}{2}}}{8A^{10}Z} * \frac{\partial}{\partial x} * \left(\frac{\left(1+\widehat{K}\eta^2\right)^{\frac{3}{4}}}{\eta^2} * e^{\frac{x}{2}}\psi^{+[-]}\right) \\ &-\frac{Re^2}{64A^{16}Z^2} * \frac{\left(1+\widehat{K}\eta^2\right)^2}{\eta^4}\int_x^{x_T}\int_0^{x'} \bar{S}_M|_{y=1[0]}dx''\,dx' - \frac{Re^2}{64A^{14}Z^2}\left(\frac{1}{\eta^4}\right) * \int_x^{x_T}\eta'\bar{S}_\theta|_{y=1[0]}dx' \\ &+\frac{\left(Re^2\,\widehat{K}\right)}{32A^{14}Z^2} * \left(\frac{1}{\eta^2}\right)\int_x^{x_T}\bar{S}_E|_{y=1[0]}dx' \end{aligned} \qquad (2.13)$$

Where ψ is the stream function that is related to the axial mass flux and the master potential as follows

$$\rho v_z = -2A^2Z * \frac{\partial \psi}{\partial x} = 4A^4Z * \left(\frac{\partial^2 \mathrm{X}}{\partial x^2}\right) \qquad (2.14)$$

The general FEM solution of the Equation (2.10) involves a linear combination of the basis functions, $\phi_k(x,y)$,

$$\mathcal{X}(x,y) \approx \sum_{k=1}^{K} a_k\phi_k(x,y), \qquad (2.15)$$

where *K* is the total degrees of freedom defined by the total number of FE grid points, a_k are arbitrary constants, and ϕ_k is the basis function associated with grid *k*. The 2D basis functions can be written as product of separate one-dimensional basis functions in each direction as

$$\phi_k(x,y) = \sigma_i(x)\lambda_j(y) \qquad (2.16)$$

Thus, Equation (2.15) can be rewritten in terms of 1D basis functions as follows

$$\mathcal{X}(x,y) \approx \sum_{k=1}^{K} a_k\phi_k(x,y) \approx \sum_i\sum_j a_k\sigma_i(x)\lambda_j(y) \qquad (2.17)$$

Since the simplified weak form of Equation (2.3) has three derivatives in the x-direction as shown in Equation (2.11), a linear combination of any arbitrary cubic spline functions can be used to approximate the basis function in the x-direction. Likewise, the weak form only has one derivative in the y-direction and thus linear splines can serve as appropriate basis functions. The details of these functions are presented by Witt [42]. In equation (2.17), the total degrees of freedom, *K*, is determined as

$$K = (M-1) * (N+1), \qquad (2.18)$$

where *M* = number of grid points in the x-direction and *N* = number of grid points in the y-direction.

Meanwhile, *k*, comes from the following:

$$k = (N+1)(i-1) + (j+1) \tag{2.19}$$

Equation (2.10) can be re-written entirely in terms of the basis functions.

Let,

$$\widetilde{\mathcal{X}}(x,y) \approx \sum_{\tilde{k}=1}^{K} a_{\tilde{k}} \phi_{\tilde{k}}(x,y) \tag{2.20}$$

Then Equation (2.10) becomes

$$B\left(\sum_{k=1}^{K} a_k \phi_k(x,y), \sum_{\tilde{k}=1}^{K} a_{\tilde{k}} \phi_{\tilde{k}}(x,y)\right) = F\left(\sum_{\tilde{k}=1}^{K} a_{\tilde{k}} \phi_{\tilde{k}}(x,y)\right). \tag{2.21}$$

After some manipulations, Equation (2.21) can be written as a matrix equation to solve of the unknown constants, a_k, as

$$[A]\vec{C} = \vec{D}, for\ k = 1,2, \dots K, and\ \tilde{k} = 1,2, \dots K \tag{2.22}$$

$$A_{\tilde{k},k} = B(\phi_{\tilde{k}}, \phi_k) \tag{2.23}$$

$$C_{\tilde{k}} = a_{\tilde{k}} \tag{2.24}$$

$$D_{\tilde{k}} = F(\phi_{\tilde{k}}) \tag{2.25}$$

The solution of the matrix equation requires solving for $B(\phi_{\tilde{k}}, \phi_k)$ and $F(\phi_{\tilde{k}})$. Equation (2.23) can be written for $\phi_{\tilde{k}}$using Equation (2.11) and Equation (2.25) using Equation (2.12) in terms of several integrals as done by Witt.

$$A_{\tilde{k},k} = I_1 + I_2 + I_3 \tag{2.26}$$

$$D_{\tilde{k}} = I_4 + I_5 + I_6 + I_7 + I_8 \tag{2.27}$$

Where

$$I_1 = \int_0^{x_T} \int_0^1 \eta^2 \left(e^x \phi_{k_{xx}}\right)_x \left(e^x \tilde{\phi}_{k_{xx}}\right)_x dydx\,, \tag{2.28}$$

$$I_2 = \int_0^{x_T} \int_0^1 \frac{Re^2}{16A^{12}Z^2} * \frac{\left(1 + \widehat{K}\eta^2\right)}{\eta^4} \phi_{k_y} \phi_{\tilde{k}_y}\, dydx\,, \tag{2.29}$$

$$I_3 = \frac{Re^{\frac{3}{2}}}{4A^8 Z} * \int_0^{x_T} \frac{\left(1 + \widehat{K}\eta^2\right)^{\frac{3}{4}}}{\eta^2} * \left(e^{\frac{x}{2}}\right) * \left(\phi_{k_x} \phi_{\tilde{k}_x}|_{y=0} + \phi_{k_x} \phi_{\tilde{k}_x}|_{y=1}\right) dx\,, \tag{2.30}$$

$$I_4 = -\int_0^{x_T} \int_0^1 \phi_{\tilde{k}} \bar{S}\, dydx \tag{2.31}$$

$$I_5 = -\int_0^{x_T} \int_0^1 \phi_{\tilde{k}} \overline{H}\, dydx \tag{2.32}$$

$$I_6 = -\frac{Re}{32A^{10}Z^2} \int_0^1 \phi_{\tilde{k}}|_{x=0}\theta(y)\, dy \tag{2.33}$$

$$I_7 = \int_0^{x_T} \left(\phi_{\tilde{k}}|_{y=1}G^+(x) - \phi_{\tilde{k}}|_{y=0}G^-(x)\right) dx \tag{2.34}$$

$$I_8 = (10 * \frac{(1-A^{-2})}{x_T^2} * \int_0^1 \phi_{\tilde{k}}|_{x=0}h(y)\, dy - \frac{\left(2*(x_T+1)\right)}{x_T^2} e^{2x_T} * \int_0^1 \eta^2 \phi_{\tilde{k}_{xx}}|_{x=x_T} h(y) dy \tag{2.35}$$

A two-point gaussian quadrature is used to solve the integrals above. The mass flow code is written in Matlab©, and the built-in algorithms are used to solve the matrix problem in Equation (2.22). Once the coefficients $a_{\tilde{k}}$ in Equation (2.24) are determined, the master potential X can be evaluated from Equation (2.17) and the physical flow parameters including the axial mass flux and streamfunctions are calculated per Equation (2.14). This mass flux matrix is later used as an input to the isotopic diffusion model.

The terms $\bar{S}$ and $\overline{H}$ include the source terms adapted from the conservation of mass, momentum, and energy. To relate these terms to physical parameters, the source of mass is indicated by *M*, the source of momentum is $\boldsymbol{F_s} = (F_r, F_\theta, F_z)$, and the sources of work and heat are *W* and *Q*. The mass that enters the rotor interior has temperature T_s, and velocity $\boldsymbol{V_s} = (V_r, V_\theta, V_z)$. The quantities in Equations (2.4) - (2.7) are related to the physical variables and scaled and non-dimensionalized for the FEM code as follows. The approach is similar to that described in [46] [47].

$$M_0 = \frac{\left(M_0 * \frac{A^3}{\pi a^3 Z}\right)}{\rho_w \Omega} \tag{2.36}$$

$$U_0 = \frac{\left((M_0 * v_r + F_r\ ) * \left(\frac{A^3}{\pi a^3 Z}\right)\right)}{\rho_w \Omega^2 a} \tag{2.37}$$

$$V_0 = \frac{[(v_\theta - \Omega a) M_0 + F_\theta] * \left(\frac{A^3}{\pi a^3 Z}\right)}{\rho_w \Omega^2 a} \tag{2.38}$$

$$W_0 = \frac{\left([M_0 v_z + F_z] * \left(\frac{A^3}{\pi a^3 Z}\right)\right)}{\rho_w \Omega^2 a} \tag{2.39}$$

$$J_0 = \frac{\left(\left\{Q + W - qF_s + M_0 * \left(\frac{(V_s - q)^2}{2} - c_p * (T_0 - T_s)\right)\right\} * \left(\frac{A^3}{\pi a^3 Z}\right)\right)}{\rho_w a^3 \Omega^3} \tag{2.40}$$

The values of the source strengths described above vary depending on the specific countercurrent drive being modeled. More specifically, if the feed is being modeled, the components of $\boldsymbol{F}_s$ in Equations (2.37) - (2.40) are ignored and the strengths are purely the functions of mass flow rate at the feed location. Likewise, if the scoop drag force is being modeled, the mass flow terms go to zero and the strengths are based on $\boldsymbol{F_s}$. The local velocity of the gas is presumed to be prescribed from the solid body rotation such that $\boldsymbol{q} = (0, \Omega r, 0)$. In this work, the feed is modeled as a source of mass given by Equation (2.36) and scoop force modeled as a sink of angular momentum indicated as -V_0. The mass is assumed to exit the interior through pores in boundary located at the position of scoop extraction holes. Each of the flow drive solutions can be obtained individually and combined to establish an overall fluid dynamic in the rotor interior. Thus, the right-hand side vector of the FEM solution in Equation (2.27) is a linear combination of I_4, I_6, and I_7 for the purpose of this work. It is important to note that Equations (2.36) - (2.40) only represent the magnitudes of the sources and sinks. The distribution of these sources can be modeled using different mathematical functions. The original version of the mass flow code written by Witt and Thomas makes use of the Dirac delta function to model the spread of the sources.

The effect of the choice of the function types on the mass flow solution as well as the isotopic diffusion is highlighted in Chapter 3 of this dissertation.

2.3 Isotopic Diffusion

Once the dynamics of the feed gas inside the centrifuge are understood, it is necessary to examine how the individual isotopes of the mixture behave. For a gas with *n* isotopes, the transport is governed by a set of *n* diffusion equations with proper boundary conditions. These equations are complex nonlinear two-dimensional partial differential equations (PDEs) that are highly demanding to solve via analytical methods. The authors in literature have manipulated the PDEs through simplifying assumptions, such as negligible radial isotopic distribution and various numerical techniques. A finite difference method (FDM) for solving the convection-diffusion equation for a binary isotopic gas mixture was presented by Kai [48]. Computations are made for the UF_6 gas in centrifuges with openings for feed, product, and waste on the end plates. Soubbaramayer [30] published another numerical method to obtain good approximations of the separation factors for the same binary mixture. In 1988, an analytical method for solving the same equation was demonstrated by Makihara and Ito [49] that showed a close agreement with the 2-D FDM proposed by Kai. Most recently, the binary isotopic mixture has been explored by Thomas [43] using similar FDM as Kai.

The increase in global interests in gas centrifuge separation for multicomponent isotopic mixture arose in the late 1980s and 1990s due to an increase in world-wide production of stable and radioactive isotopes [50] [51]. In 1992, Harink-Snijders [52] extended the theory of Soubbaramayer [30] for solving the diffusion equation to multi-component isotope mixtures and developed an iteration method to solve the newly obtained equations. Ying & Guo [53] and Levin & Ying [54] further studied the effect of multicomponent mixture on the separative performance of a gas centrifuge. Wood, Mason, and Soubbaramayer reduced the set of nonlinear PDEs that govern the diffusion-convection of each isotope to a set of nonlinear ordinary differential equations (ODEs) using the method of radial averaging [47]. A method of iteration introduced by Harink-Snijders [52] is used to solve the nonlinear equations and several optimization studies are conducted based on the solutions obtained.

The derivation of the transport vector, $\boldsymbol{\phi_k}$ of isotope *k* inside the rotor is attained from the fusion of three elementary phenomena that include the pressure diffusion ϕ_k^P, back diffusion ϕ_k^B, and convection ϕ_k^C such that:

$$\boldsymbol{\phi_k} = \boldsymbol{\phi_k^P} + \boldsymbol{\phi_k^B} + \boldsymbol{\phi_k^C} \tag{2.41}$$

Pressure diffusion is caused due to the difference in molecular weights of the isotopes as well as radial pressure gradients described in Chapter 1. Back diffusion is a function of mass density gradient in both the radial and axial directions. Convection is a function of axial mass flux created due to feed flow, scoop drag, and axial temperature difference also discussed in Chapter 1. The radial and axial components of each term from Equation (2.41) can be expressed as follows:

$$\phi_k^P\left(\frac{DM_k}{RT} * \left(\frac{\partial P_k}{\partial r}\right), 0\right) \tag{2.42}$$

$$\phi_k^B\left(-D * \left(\frac{\partial \rho_k}{\partial r}\right), -D * \left(\frac{\partial \rho_k}{\partial z}\right)\right) \tag{2.43}$$

$$\phi_k^C(\rho_k V_r, \rho_k V_z) \tag{2.44}$$

The mass density of isotope *k* is related to its mole fraction and the total mass density of the gas by

$$\rho_k = \rho N_k, where\ \rho = \sum_{j=1}^{n} \rho_j\ \ and\ \sum_{j=1}^{n} N_j = 1 \tag{2.45}$$

The mass density ρ, the pressure *p*, the temperature *T*, and the molecular mass *M* of the gas is related by the ideal gas law as $p = \frac{\rho RT}{M}$. In steady state, the gas remains in thermal equilibrium and has the same angular velocity as the rotor. The balance of the centrifugal and pressure forces further allows the equilibrium of the gas. This balance can be expressed by the following relationship:

$$\frac{\partial P_k}{\partial r} = \rho_k \Omega^2 r = \rho \Omega^2 r N_k \tag{2.46}$$

Substituting Equations (2.45) and (2.46) into (2.42) - (2.44) results in the radial and axial components of the transport vector introduced in (2.41) for each isotope.

$$\phi_{k,r} = \rho D * \frac{\Omega^2 r}{RT} M_k N_k - \rho D * \left(\frac{\partial N_k}{\partial r}\right) - \rho D * \left(\frac{\Omega^2 r}{RT}\right) N_k * \sum_{j=1}^{n} M_j N_j + \rho V_r N_k \tag{2.47}$$

$$\phi_{k,z} = -\rho D * \left(\frac{\partial N_k}{\partial z}\right) + \rho V_z N_k \tag{2.48}$$

The steady-state conservation law for isotope *k* is given by the divergence of the transport vector as

$$div\ \boldsymbol{\phi_k} = \frac{1}{r}\left(\frac{\partial}{\partial r}\right)(r\phi_{k,r}) + \frac{\partial}{\partial Z}\phi_{k,z} = 0 \tag{2.49}$$

For a constant gas diffusion coefficient (ρD), the diffusion equation for isotope *k* is obtained using the continuity equation as

$$-\rho D * \frac{\partial^2 N_k}{\partial Z^2} - \rho D * \left(\frac{1}{r}\right)\left(\frac{\partial}{\partial r}\right) * \left[r * \frac{\partial N_k}{\partial r} - \frac{\Omega^2 r^2}{RT}\left(M_k - \sum_{j=1}^{n} M_j N_j \right) N_k \right]$$
$$+\rho V_z * \frac{\partial N_k}{\partial Z} + \frac{1}{r}\rho V_r \left(\frac{\partial N_k}{\partial r}\right) = 0 \qquad (2.50)$$

There are four boundary conditions associated with Equation (2.50). In the radial direction, there is no radial transport at the rotor wall and on the axis. At r=a,

$$\frac{\partial N_k}{\partial r} - \frac{\Omega^2 a}{RT} * \left(M_k - \sum_{j=1}^{n} M_j N_j \right) N_k = 0 \qquad (2.51)$$

At r=0:

$$\frac{\partial N_k}{\partial r} = 0. \qquad (2.52)$$

In the axial direction, the isotope transport equals a constant. The constant varies depending on the end cap as it considers the removal of the enriched and depleted material from the centrifuge. At z=0,

$$\int_0^a \phi_{k,z} 2\pi r \, dr = \int_0^a \left(-\rho D * \frac{\partial N_k}{\partial Z} + \rho V_z N_k \right) 2\pi r \, dr = -F(1-\theta) N_{w,k} \qquad (2.53)$$

At $z = z_H$:

$$\int_0^a \phi_{k,z} 2\pi r \, dr = \int_0^a \left(-\rho D * \frac{\partial N_k}{\partial Z} + \rho V_z N_k \right) 2\pi r \, dr = -F\theta N_{p,k} \, , \qquad (2.54)$$

where *F* is the feed rate, $N_{w,k}$ and $N_{p,k}$ are the concentrations of isotope *k* at the tails and product streams respectively. These end concentrations are related to the concentration at the feed point by the following overall species balance equation for isotope *k*.

$$N_{F,k} = \theta N_{P,k} + (1-\theta) N_{w,k} \qquad (2.55)$$

For a gas mixture of *n* isotopes, *n* equations like Equation (2.50) together with *n* boundary conditions similar to Equations (2.51) - (2.54) need to be solved to determine the isotopic concentrations at specific radial and axial points. This set of diffusion equations is solved by Wood et. al by radially averaging the concentrations to reduce the dimensions of the PDE to 1-D ordinary differential equation in the axial direction. The radially averaged mole fraction of isotope *k* is given by

$$\overline{N_k} = \frac{1}{\pi a^2} * \int_0^a N_k 2\pi \, r dr \qquad (2.56)$$

The term $\overline{N_k}$ in the above equation varies only in the axial coordinate *z*. The solution is detailed by Wood et. al [47] and also utilized by Ying et. al [55]. While the radial averaging method solves the diffusion equations readily, it only determines the axial separation of the isotopes in the centrifuge. The solutions in literature that utilize two-dimensional solutions such as finite differences and finite volume are limited to solving the binary mixture problems, considering two dominant isotopes. Therefore, a full two-dimensional multi-component solution of the problem is obtained in Chapter 4 of this dissertation using a finite element method. The 2-D code is verified against the above mentioned 1-D radial averaged values. Because of the lack of experimental data available in open-source literature for this problem, a methodology is developed to perform sensitivity analysis and uncertainty quantification to ensure the accuracy of the solutions and detailed in Chapter 5.

2.4 Centrifuge Cascades

As briefly discussed in Chapter 1, gas centrifuges are arranged together in cascades to meet the production demand of required quantity and concentrations of enriched uranium fuel. The cascade theory is developed from the solutions of equations derived by satisfying material balances and combined with the separation in a single stage. The stages of the centrifuge cascade can be arranged in numerous ways; however, the most common arrangement in separation plants is the symmetric, countercurrent scheme. In such a cascade, the product out of a particular stage is fed into the next upstream stage while the tails or depleted material is sent back to the previous downstream stage for further enrichment. A general stage diagram of a symmetric countercurrent cascade is shown in Figure 2.2. The overall separation achieved in the cascade depends on several parameters such as the stage separation factor, the number of stages, and the rate at which the material flows in and out of each stage. The material, usually the gas of interest such as UF_6, flows into the feed stage *n* of the cascade at a designed rate *F* and isotopic composition N_F. Passing through all of the machines and stages, the material is enriched in the desired isotope at one end and extracted from the cascade at rate *P* with composition N_P. The depleted material flows through the tails or waste stream at rate *W* and composition N_W. The stages are numbered consecutively in the positive direction for the enriching section and in the negative direction for the stripping section starting from the feed stage.

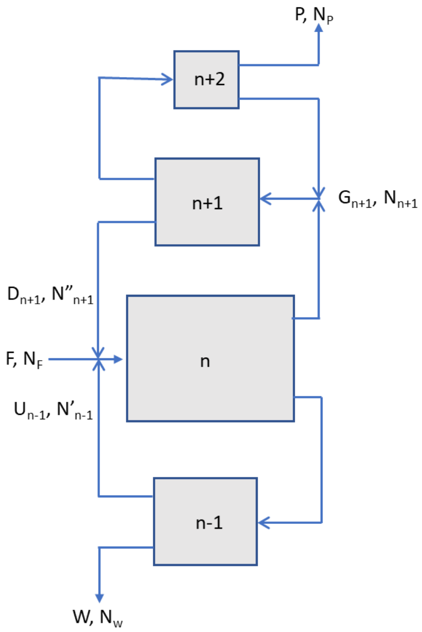

Figure 2.2: Schematic of an example symmetric countercurrent cascade with three enriching stages and one stripping stage

The flow and isotopic composition must satisfy the balance of material over the entire cascade. Assuming insignificant amount of material losses via piping and a steady state operation, the overall and material balance in the cascade are given by

$$F = P + W \tag{2.57}$$

$$FN_{Fi} = PN_{Pi} + WN_{Wi}, \tag{2.58}$$

where the subscript *i* refers to the isotope of interest. The balance equations above can be used similarly in the interior of the cascade at each stage. For stage n,

$$G_n = U_n + D_n \tag{2.59}$$

$$G_n N_{n,i} = U_n N'_{n,i} + D_n N"_{n,i} \tag{2.60}$$

where G_n is the stage feed rate, U_n is the upflow rate, D_n is the downflow rate, $N_{n,i}$ is the stage feed concentration of isotope *i*, $N'_{n,i}$, is the stage upflow concentration of isotope i, and $N''_{n,i}$ is the stage downflow concentration of isotope *i.* The stage cut can be defined as the ratio of upflow rate to feed rate as

$$\theta_n = \frac{U_n}{G_n} \tag{2.61}$$

For a multicomponent mixture of isotopes with *J* different isotopes, the abundance ratio of each component is defined with respect to a key component *k,* ^{235}U in a UF$_6$ mixture, as follows

$$R_i = \frac{N_i}{N_k}, i = 1,2, \dots, J \qquad (2.62)$$

The overall stage separation factors then can be defined as

$$\gamma_{n,i} = \frac{R_i'}{R''_i} = \frac{N'_i}{N'_k} * \frac{N_k''}{N_i''} \qquad (2.63)$$

The stage separation factors can be rearranged and combined with the balance equations above to obtain the cascade gradient equations. To determine the concentrations of individual isotopes at each stage, a multicomponent productivity analysis is required, which is an iterative process that begins with an initial guess for the cascade product concentrations. The solution procedure has been outlined in detail by Von Halle [56] and most recently by Migliorini [57]. The definitions and model developed by Migliorini is utilized in this dissertation to perform the cascade analyses using gas centrifuge data obtained from the 2D multicomponent diffusion code. The details of the cascade studies are presented in Chapter 6.

Chapter 3

The Effect of Source Function Types on the Mass Flow and Isotopic Distribution

3.1 Overview

As delineated in Chapter 2, the gas flow models inside a centrifuge domain are derived using the sources and sinks of mass, momentum, and energy. The system of equations governing the flow are combined to give non-homogeneous form of Onsager-Maslen equation without the pancake approximation, which is solved using finite element analysis. This chapter focuses on the analysis of source distribution and strength for feed injection and the tails and product withdrawal via boundaries. Four different types of shape functions for the axial spreading of the sources and sinks are evaluated and their impact on the flow and isotopic distributions are compared. The non-dimensionalized strength values are defined by Equations (2.36) – (2.40) in Chapter 2. In the radial direction, the source distribution is assumed to be given by a delta function while in the axial direction, the four different cases considered include triangular, linear step, Gaussian, and delta functions. The triangle and the Gaussian are anticipated to be more realistic representation of the flow shapes and provide smoother distributions. In order to facilitate the comparison of these three functions, mass flow and concentration gradient plots are generated for hypothetical centrifuges.

There are numerous studies in literature that make use of the sources and sinks to model fluid dynamics. In this chapter, the focus is on the definitions of the functions used to model them. The geometry of source distribution has been removed and simplified distribution functions are used [36]. While different studies used different types of these distribution functions to model the sources, there is not a study in literature that evaluates the effects of such functions on the fluid flow and in turn isotope separation. Therefore, four different types of shape functions are derived to simulate the radial and axial spreading of sources and sinks and their impact on mass flow as well as diffusion is compared to determine the most ideal shape. For a more quantitative comparison, the normalized root-mean square difference of the stream function and concentration gradients for each type are evaluated and analyzed. A large portion of this chapter appears in the paper titled "The Effect of Source Function Types on the Mass Flow and Isotopic Distribution inside a Gas Centrifuge" in the *Proceedings of the INMM & ESARDA Joint Virtual Annual Meeting 2021* [58].

3.2 Definitions of the Sources

The fluid dynamics model used is the Onsager-Maslen equation with curvature effects and the inclusion of internal source/sink terms given in Equations (2.3) – (2.7). The finite element solution for mass flow derived by Witt and enhanced by Thomas is used to test the effects of various source types. The strength and distribution of these sources can be approximated by the feed entry and the tails-withdrawal scoop by separate analyses. The same simplifying assumptions made by Wood & Sanders regarding an idealized model of the feed interacting with the rotating gas is utilized here as well [36]. These assumptions include the fact that the gas enters the centrifuge rotor in an angularly symmetric process, the feed gas collides with the rotating gas and becomes indistinguishable after one collision, and the gas enters a vacuum as it exits the hole in the feed pipe and spreads in the axial direction before colliding with the rotating gas. The shape function for such axial spreading is the matter of analysis in this work. The source terms can be generalized mathematically as

$$S(x,y) = S_0 G(x) H(y), \tag{3.1}$$

where S_0 is the strength, $H(y)$ is the axial distribution and $G(x)$ is the radial distribution. Equation (3.1) is used as an approximation of the mass, momentum, and energy terms in the right-hand side of Equation (2.3). In the radial direction, the distribution is modeled by the Dirac delta function chosen because of its convenient mathematical analysis. Therefore, in Equation (3.1),

$$G(x) = \delta(x - x^*), \tag{3.2}$$

where x^* is the radial location of the source and x is defined in scale heights. For the axial distribution, the four different functions mentioned previously will be used. A simplified visual representation of three of the four functions as they enter the rotor interior are shown in Figure 3.1.

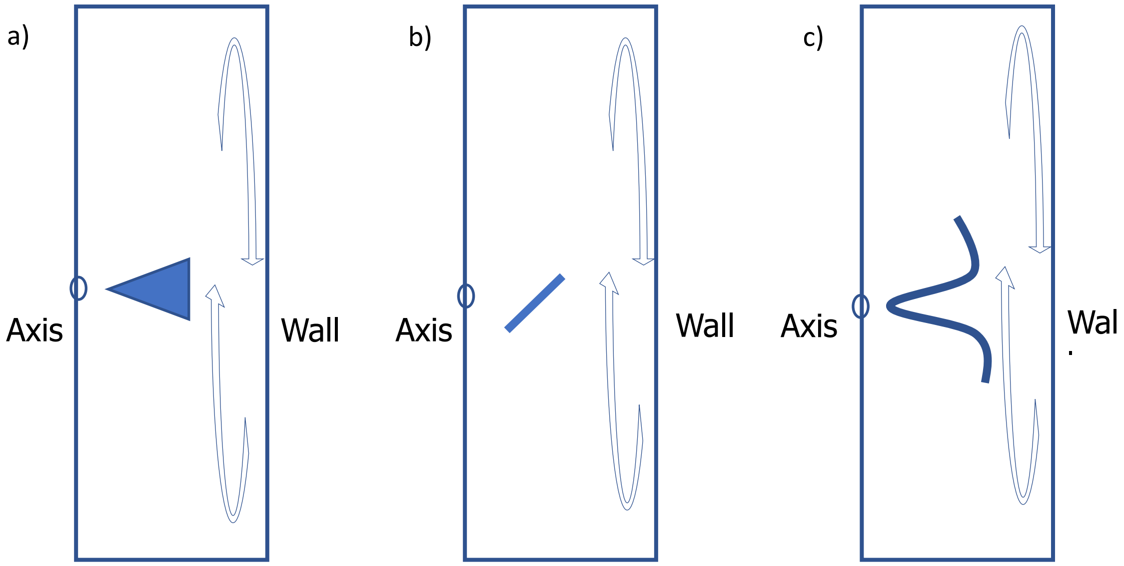

Figure 3.1: Simplified visual representation of the three new sources (a) Triangular (b) Linear step (c) Gaussian

The analytical integrations for each source in the finite element calculations are included in the next section.

3.3 Source Derivations

3.3.1 Triangular Source

The description of the triangular shape of the distribution function is taken from Wood & Sanders [36]. The axial source distribution in Equation (3.1) is given by

$$H(y) = \begin{cases} 0 & (|y - y^*| > 0.5) \\ -4|y - y^*| + 2 & (|y - y^*| \leq 0.5) \end{cases} \tag{3.3}$$

where y^* is the axial location of the source and y is defined as the length divided by the rotor radius, i.e., $y = \frac{z}{a}$. $H(y)$ is a triangle of unit base with an altitude of 2. This function becomes a concentrated source for a centrifuge with larger aspect ratio as will be considered for this study.

In order to apply the above source function to the finite element solution of Equation (2.3), the right-hand side vector in Equation (2.22) needs to be modified. Recall the matrix equation from Chapter 2:

$$[A]\vec{C} = \vec{D},\ \textit{where}\ A_{k,k^*} = I_1 + I_2 + I_3\ \textit{and}$$
$$D_{k^*} = I_4 + I_5 + I_6 + I_7 + I_8 \tag{3.4}$$

Here, $k = 1,2,3 \ldots .K\ and\ k^* = 1,2,3, \ldots K$,

$K = (M-1) * (N-1)$, where

$M = \#\ grid\ points\ in\ the\ radial\ direction, N = \#\ grid\ points\ in\ the\ axial\ direction.$

The eight integrals that make up Equation (3.4) were reported in Chapter 2. The focus here is on I_4 to account for the effects of sources and sinks in the mass flow. I_4 is given by

$$I_4 = -\int_0^{x_T}\int_0^1 \phi_{k^*}\bar{S}\,dy\,dx\,, \tag{3.5}$$

where $\phi_k(x,y) = \sigma_i(x)\lambda_j(y)$ is the product of the finite element shape functions given by σ in the radial direction and λ in the axial direction.

$$\bar{S} = -\frac{Re^2}{64A^{16}Z^2} * \frac{1+\hat{k}\eta^2}{\eta^4}\int_x^{x_T}\int_0^{x'}\frac{\partial S_M}{\partial y}\,dx"dx' \tag{3.6}$$

Equation (3.6) is given here only for the mass source. The four different source functions will solely evaluate the mass distribution at the feed. The momentum exerted by the scoop and mass sinks at the exits will be kept consistent with the analysis performed by Witt. Additionally, to simplify the derivations, the feed is modeled as a source of mass and scoop as a sink of angular momentum.

From Equation (3.6), the derivative term, $\frac{\partial S_M}{\partial y}$ for the triangular function defined in Equation (3.3) is obtained as:

$$\frac{\partial S_M}{\partial y} = S_0 * \delta(x-x^*) * \frac{\partial H}{\partial y} \tag{3.7}$$

$$\frac{\partial H}{\partial y} = \begin{cases} 0 & (|y-y^*| > 0.5) \\ -\dfrac{4y-2}{|y-y^*|} & (|y-y^*| \le 0.5) \end{cases} \tag{3.8}$$

Plugging Equation (3.8) into Equation (3.7),

$$\bar{S} = -\frac{Re^2}{64 * A^{16} * Z^2} * \frac{1+\hat{K}\eta^2}{\eta^4} * S_0 * \frac{\partial H}{\partial y} * \left(\int\limits_x^{x_T}\int\limits_0^{x'}\delta(x'-x^*)\,dx''\,dx'\right) \tag{3.9}$$

The double integral in Equation (3.9) can be simplified further down to:

$$\bar{S} = -\frac{Re^2}{64*A^{16}*Z^2} * \frac{1+\hat{K}\eta^2}{\eta^4} * S_0 * \frac{\partial H}{\partial y} * \left(\int_x^{x_T} x' * \delta(x'-x^*)\,dx'\right) \tag{3.10}$$

Plugging Equation (3.10) into Equation (3.5) yields the expression for I_4.

$$I_4 = \frac{Re^2}{64A^{16}Z^2} * \frac{1+\hat{k}\eta^2}{\eta^4} * S_0 \int_0^{x_T} \sigma(x) * \begin{gathered} \left(\int_x^{x_T} x' * \delta(x'-x^*)\, dx'\right) dx \\ * \int_{y^*-0.5}^{y^*+0.5} -\frac{4y-2}{|y-y^*|}\big(\lambda(y)\big) dy \end{gathered} \tag{3.11}$$

A new Matlab script is developed to solve Equation (3.11), which is then used as the right-hand side vector of the finite element problem given by Equation (3.4). The integrals in Equation (3.11) are evaluated numerically using the built in Matlab© solvers.

3.3.2 Linear Step Function Source

The axial distribution of the source of this type is defined by Wood [46] as follows:

$$H(y) = \begin{cases} 0 & 0 \le y < y^* - 1.5 \\ y & y^* - 1.5 \le y \le y^* + 1.5 \\ 0 & y^* + 1.5 < y \le y_T \end{cases} \tag{3.12}$$

Equation (3.12) is a slightly modified version of the same expression defined in [46] where a constant value of $H(y)$ is replaced with a variable, y in and around the axial location of source. This change was necessary to ensure that the axial derivative of H exists as required by Equation (3.7). Thus, following the same derivation as for the triangular source, the expression for I_4 can be evaluated as follows:

$$\frac{\partial H}{\partial y} = \begin{cases} 0 & 0 \le y < y^* - 1.5 \\ 1 & y^* - 1.5 \le y \le y^* + 1.5 \\ 0 & y^* + 1.5 < y \le y_T \end{cases} \tag{3.13}$$

Plugging $\frac{\partial H}{\partial y}$ into Equation (3.9) and the resulting expression for $\bar{S}$ into Equation (3.5) yields:

$$I_4 = \frac{Re^2}{64A^{16}Z^2} * \frac{1+\hat{k}\eta^2}{\eta^4} * S_0 \int_0^{x_T} \begin{gathered} \sigma(x) * \left(\int_x^{x_T} x' * \delta(x'-x^*)\, dx'\right) dx \\ * \int_{y^*-1.5}^{y^*+1.5} 1 * \big(\lambda(y)\big) dy \end{gathered} \tag{3.14}$$

3.3.3 Gaussian Distribution Source

The expression for the gaussian source is taken from Gunzburger, Wood, and Jordan [40].

$$S_M = S_0 e^{-\alpha[(x-x^*)^2+(y-y^*)^2]} \tag{3.15}$$

A value of α was chosen such that $S_M = 10^{-6} * S_0$ at $(x-x^*)^2 + (y-y^*)^2 = 1$. Thus,

$$\begin{gathered} S_M = 10^{-6}S_0 = S_0 * e^{-\alpha*1} \rightarrow \\ \alpha = -\,ln(10^{-6}) \end{gathered} \tag{3.16}$$

Equation (3.15) is different than the other sources in that the radial source is also a Gaussian instead of a delta function. To be consistent with the rest of the functions, a delta source in the radial direction and a Gaussian in the axial is evaluated.

$$S_M = S_0\delta(x - x^*) * e^{-\alpha*(y-y^*)^2} \tag{3.17}$$

$$\frac{\partial S_M}{\partial y} = S_0\delta(x - x^*) * -2\alpha(y - y^*)e^{-\alpha((y-y^*))^2} \tag{3.18}$$

$$\bar{S} = -\frac{Re^2}{64 * A^{16} * Z^2} * \frac{1 + \widehat{K}\eta^2}{\eta^4} * \left(\int\limits_{x}^{x_T}\int\limits_{0}^{x'} \frac{\partial S_M}{\partial y} dx"dx'\right) \tag{3.19}$$

$$I_4 = \frac{Re^2}{64A^{16}Z^2} * \frac{1 + \hat{k}\eta^2}{\eta^4} * S_0 \int_0^{x_T} \begin{matrix} \sigma(x) \; * \left(\int_x^{x_T} x' * \delta(x' - x^*)\, dx'\right) dx \,* \\ \int\limits_0^1 \lambda(y) * -2\alpha(y - y^*)e^{-\alpha*((y-y^*))^2}\, dy \end{matrix} \tag{3.20}$$

3.3.4 Delta Source

The last model of the source distribution is produced using delta functions in both the radial and axial directions. This model is utilized by the finite element solution developed by Witt [42]. Since the previous authors have not outlined their reasoning for selecting a particular function type in their analysis, this work seems essential in understanding the effects of each on the derived mass flow and diffusion solutions. The derivations of the I_4 integral using the delta functions is obtained as follows:

$$S_M = S_0\delta(x - x^*)\delta(y - y^*) \tag{3.21}$$

$$\frac{\partial S_M}{\partial y} = S_0\delta(x - x^*)\delta'(y - y^*) \tag{3.22}$$

$$\bar{S} = -\frac{Re^2}{64 * A^{16} * Z^2} * \frac{1 + \widehat{K}\eta^2}{\eta^4} * S_0 * \delta'(y - y^*) * \left(\int\limits_{x}^{x_T}\int\limits_{0}^{x'} \delta(x" - x^*)\, dx"dx'\right) \tag{3.23}$$

$$\bar{S} = -\frac{Re^2}{64 * A^{16} * Z^2} * \frac{1 + \widehat{K}\eta^2}{\eta^4} * S_0 * \delta'(y - y^*) * \int_x^{x_T} \boldsymbol{H_e}(x' - x^*)dx', \tag{3.24}$$

where $\boldsymbol{H_e}$ is the Heaviside function.

$$\bar{S} = -\frac{Re^2}{64 * A^{16} * Z^2} * \frac{1 + \widehat{K}\eta^2}{\eta^4} * S_0 * \delta'(y - y^*) * \begin{cases} x_T - x^*, & x \le x^* \\ x_T - x, & x > x^* \end{cases} \tag{3.25}$$

Plugging Equation (3.25) into Equation (3.5) and simplifying the resulting expression yields

$$I_4 = \frac{Re^2}{64A^{16}Z^2} * \frac{1+\hat{k}\eta^2}{\eta^4} * S_0 * \left[x_T * \int_0^{x_T} \sigma(x)\,dx - x^* \int_0^{x^*} \sigma(x)\,dx - \int_{x^*}^{x_T} x * \sigma(x)\,dx\right] * \int_0^1 \lambda(y) * \delta'^{(y-y^*)} dy \qquad (3.26)$$

Using the properties of the delta function, the y-integral in Equation (3.26) can be simplified further as

$$I_4 = \frac{Re^2}{64A^{16}Z^2} * \frac{1+\hat{k}\eta^2}{\eta^4} * S_0 * \left[x_T * \int_0^{x_T} \sigma(x)\,dx - x^* \int_0^{x^*} \sigma(x)\,dx - \int_{x^*}^{x_T} x * \sigma(x)\,dx\right] * \lambda'(y^*) \qquad (3.27)$$

Therefore, using Equations (3.11), (3.14), (3.20), and (3.27), new Matlab scripts are developed for each to solve the finite element solution of the mass flow.

3.4 Results

The effects of the source functions on the mass flow and isotopic diffusion are explored inside hypothetical Rome [59] and Iguacu [60] centrifuges. The physical and operating parameters for these machines can be found readily in literature and have been reiterated in Table 3.1.

Table 3.1: Machine parameters for the Rome and Iguacu centrifuges. The simulations are conducted at the operating rotor speed of 600 m/s. The countercurrent flow drive parameters for this case were taken from Thomas [32].

Parameter	**Variable**	**Unit**	**Rome**	**Iguacu**
Radius	a	m	0.25	0.06
Length	z_H	m	5	0.48
Average gas temperature	T	K	320	300
Wall pressure	p	$torr$	100	60
Cut	θ	$-$	0.5	0.5
Speed	v	$\frac{m}{s}$	600	600
Feed flow rate	F	$\frac{mgUF_6}{s}$	70	30
ΔT_{Wall}	-	K	6.92	11.68
Scoop drag	-	$Dynes$	1983	854

The values of the countercurrent flow drive parameters including the feed flow rate, end-to-end temperature difference at the rotor wall, and the drag forced exerted by the stationary scoop on the rotating gas are taken from the ideal calculations performed in [43] for the machines spinning at 600 m/s. For the total flow drive solution, the feed entry is modeled as a source of mass, where each of the four different functions are used to simulate the spread of the mass source, and the scoop is modeled as a sink of angular momentum, which is represented as a point at the location of the scoop extraction

Table 3.2 Isotopic abundance of natural uranium

Isotope	[%]
^{234}U	0.0054
^{235}U	0.72
^{238}U	99.2746

hole using delta functions in both the radial and axial directions. The streamlines of the countercurrent flow and the corresponding concentration gradient for the ^{235}U uranium isotope obtained for each source are presented in Figures 3.2-Figures 3.9. Figures for Rome machines are presented first followed by Iguaçu. Natural uranium (NU), defined in Table 3.2, is used at the feed for the diffusion equation solved using finite element analysis as discussed in Chapter 4 and also documented in [61].

The streamlines of the mass flow solution using each of the four different source functions have been presented at the top of Figures 3.2-3.9. The x-axis represents the non-dimensional radial direction of the centrifuge from x=0 at the wall to x=15 at the “top of the atmosphere.” It is assumed that x-values greater than 15 marks the region in the rotor that remains a vacuum at the high speed rotation analyzed in this research. Since the equations of continuity are not valid in a vacuum, the gas flow and isotopic diffusion plots only present results in the continuum i.e. up until x=15. The term “top of the atmosphere” comes from the analogy made to compare the separation phenomena inside the operating centrifuge to the variations in the composition of gases with increasing altitude above the surface of the Earth. Heavier gases tend to travel to higher pressure zones towards the surface and lighter species travel in the opposite direction towards the top of the atmosphere.

The y-axis in Figures 3.2-3.9 is the axial dimension divided by the rotor height, Z_h that goes from bottom of the machine at y=0 to the top at y=1. It can be observed that much of the flow for each case is concentrated very near the rotor wall between x=0 and x=2. The color bar indicates the peaks and troughs of the countercurrent flow field with higher elevation corresponding to increasing magnitude shown on the right. For each source, the gas enters the centrifuge rotor at the axial midpoint and at roughly around x=12. The point where the feed interacts with the rotating gas can be visually observed in all the figures between x=10 and x=8. The gas exits the rotor both at the top and the bottom surfaces at x=10.

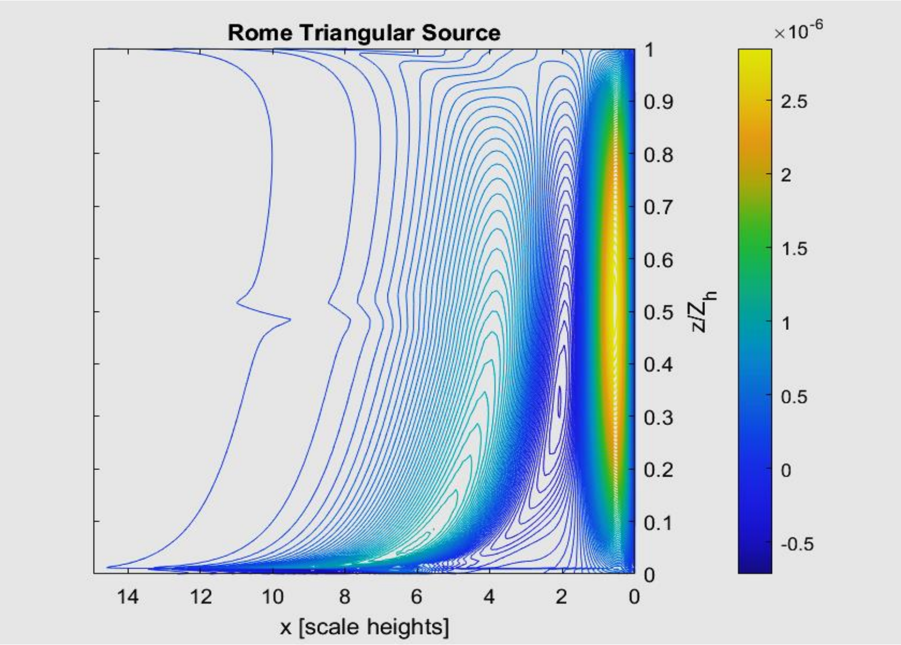

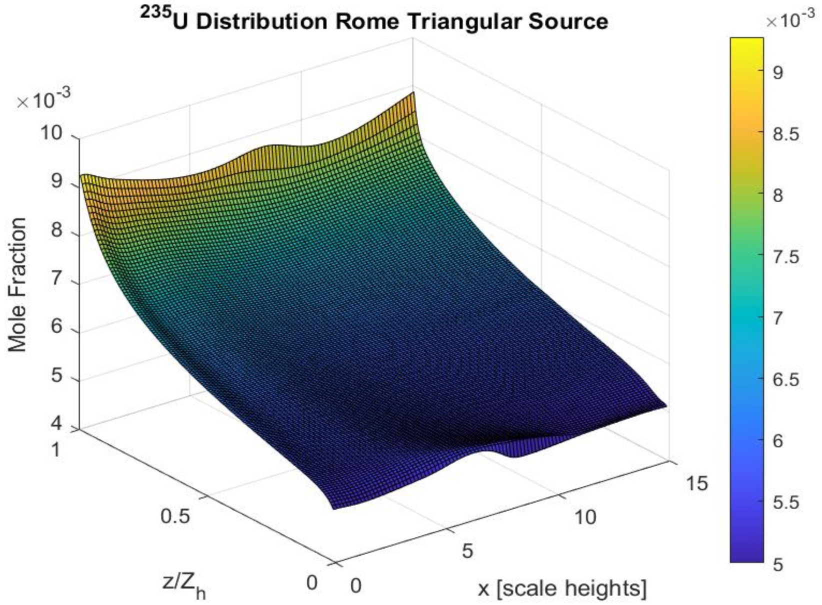

Figure 3.2: Streamlines of the total drive flow solution obtained using triangular mass source at the feed (top) and the corresponding ^{235}U concentration gradient (bottom)

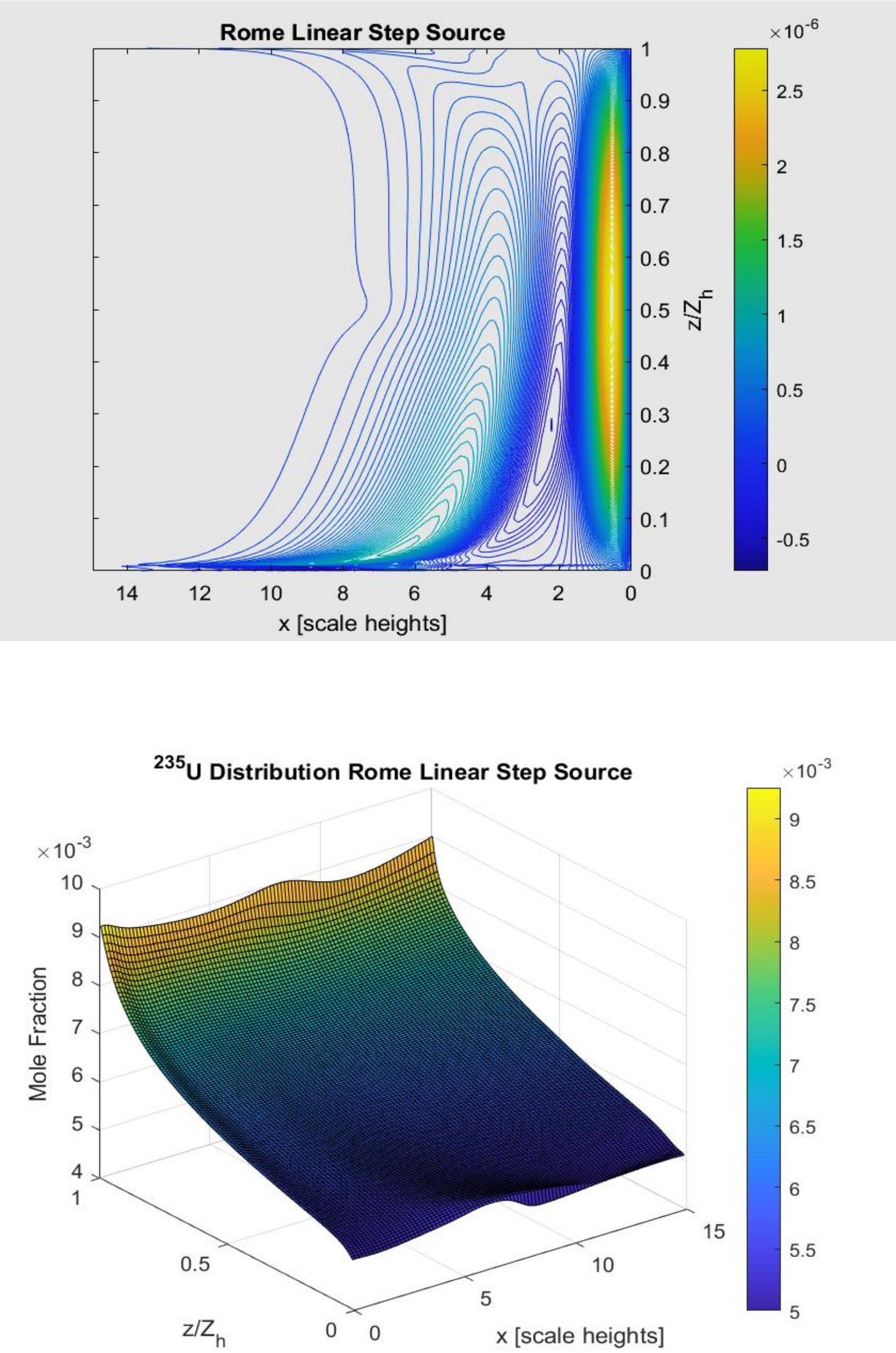

Figure 3.3: Streamlines of the total drive flow solution obtained using linear step mass source at the feed (top) and the corresponding ^{235}U concentration gradient (bottom)

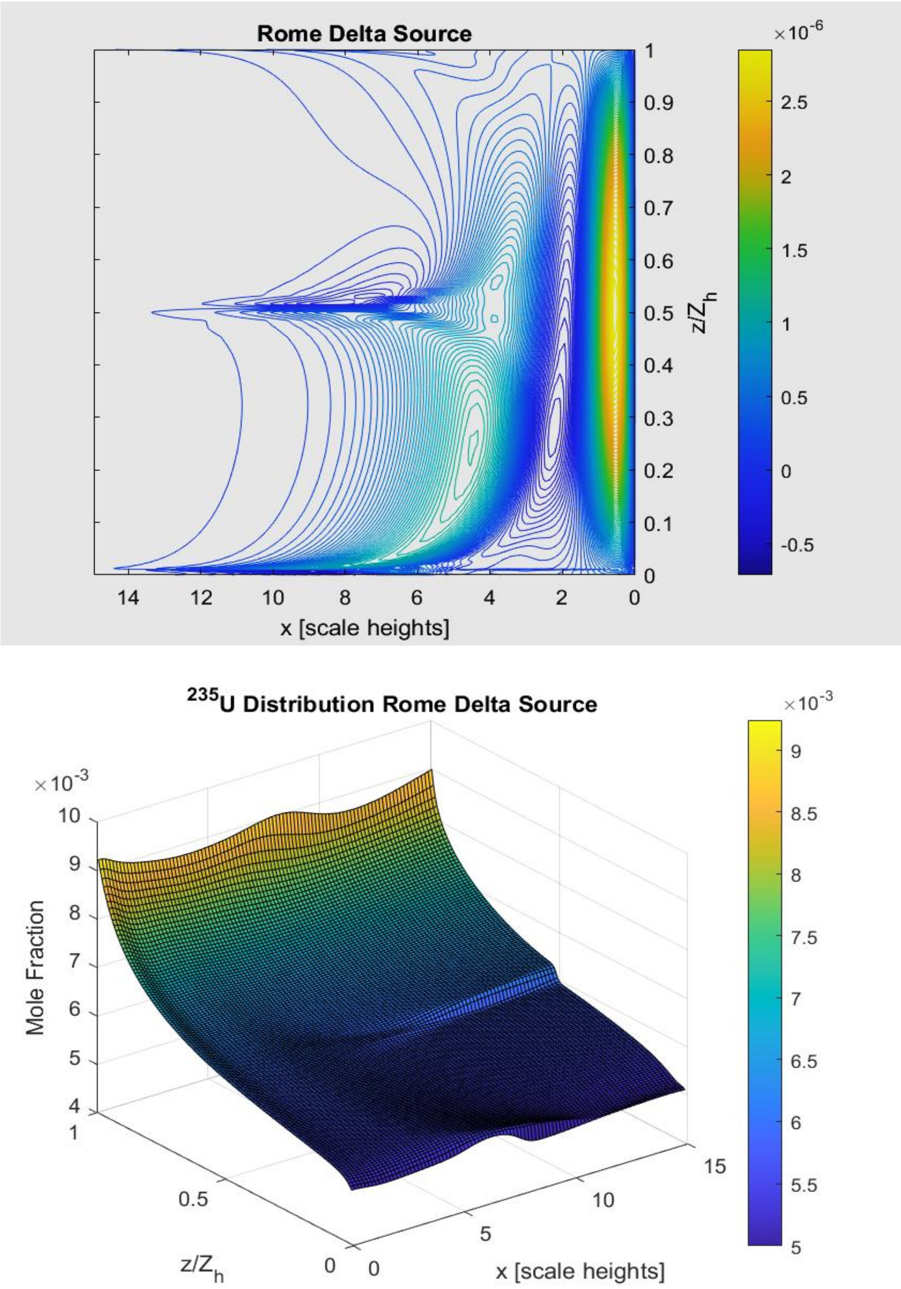

Figure 3.4: Streamlines of the total drive flow solution obtained using delta function mass source at the feed (top) and the corresponding ^{235}U concentration gradient (bottom)

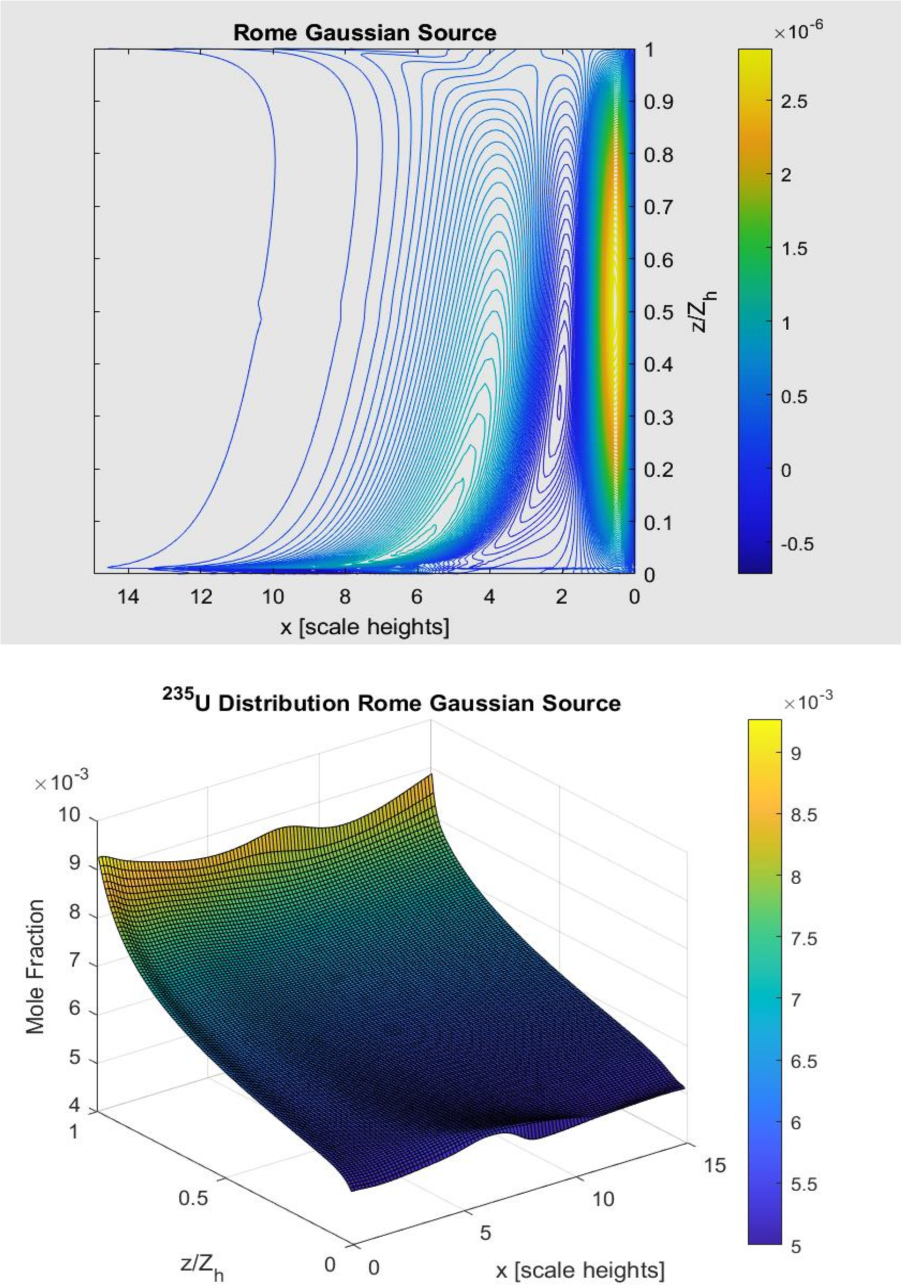

Figure 3.5: Streamlines of the total drive flow solution obtained using Gaussian mass source at the feed (top) and the corresponding ^{235}U concentration gradient (bottom)

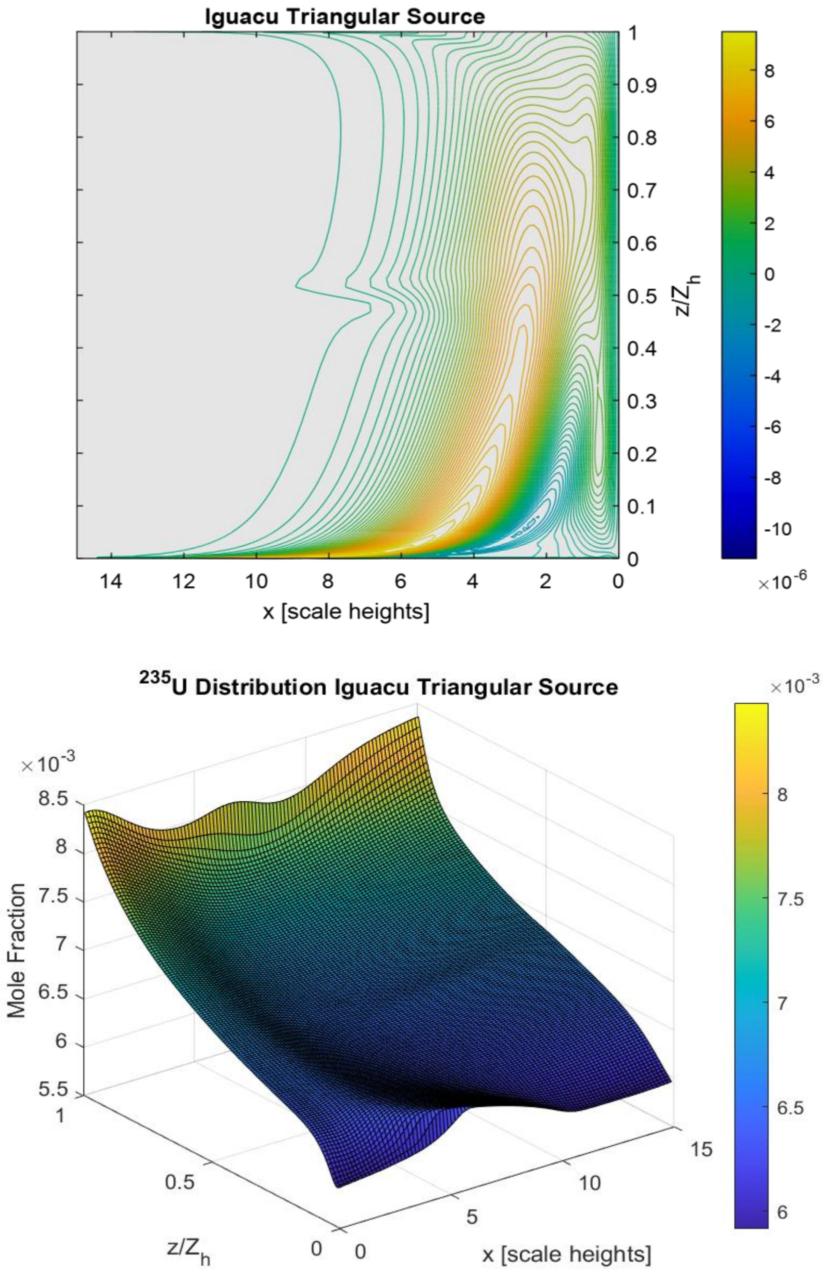

Figure 3.6: Streamlines of the total drive flow solution obtained using triangular mass source at the feed (top) and the corresponding ^{235}U concentration gradient (bottom) using Iguaçu centrifuge

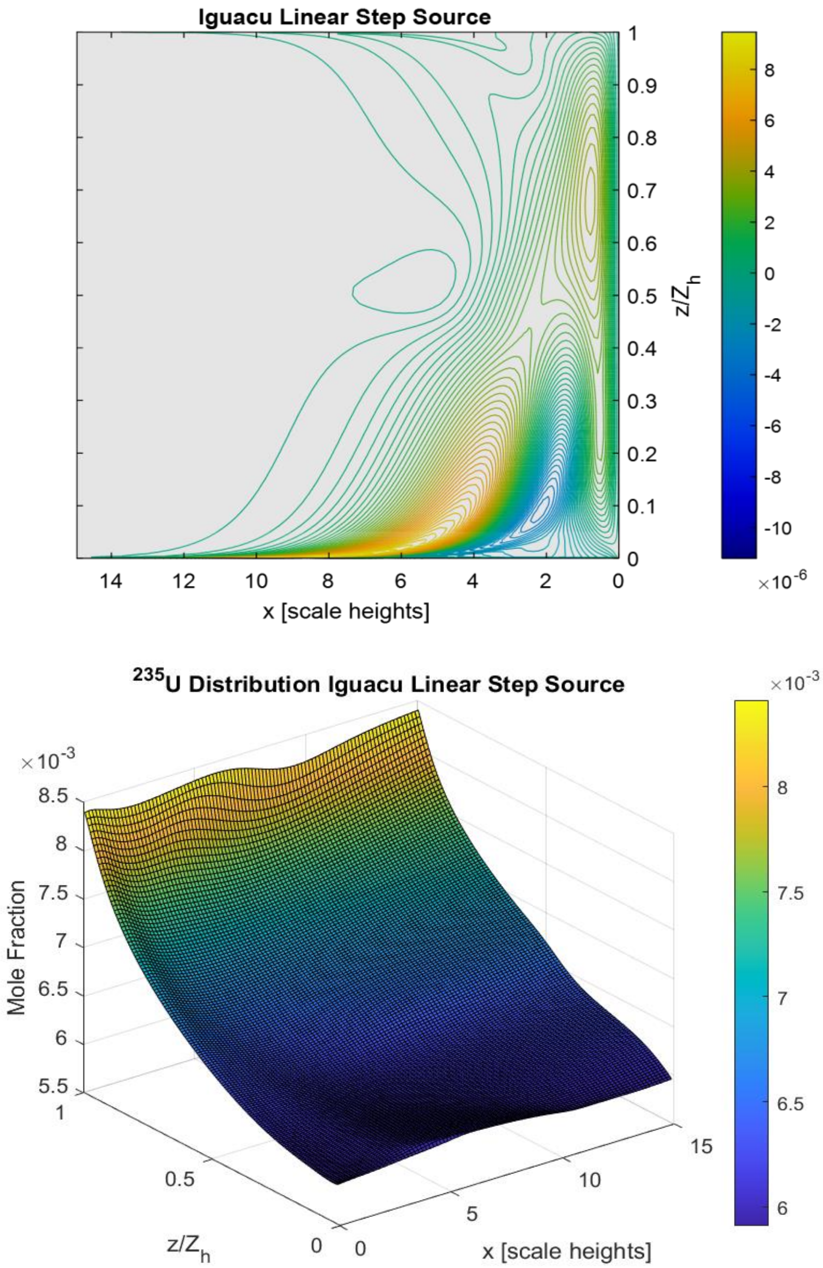

Figure 3.7: Streamlines of the total drive flow solution obtained using linear step mass source at the feed (top) and the corresponding ^{235}U concentration gradient (bottom) using Iguaçu centrifuge

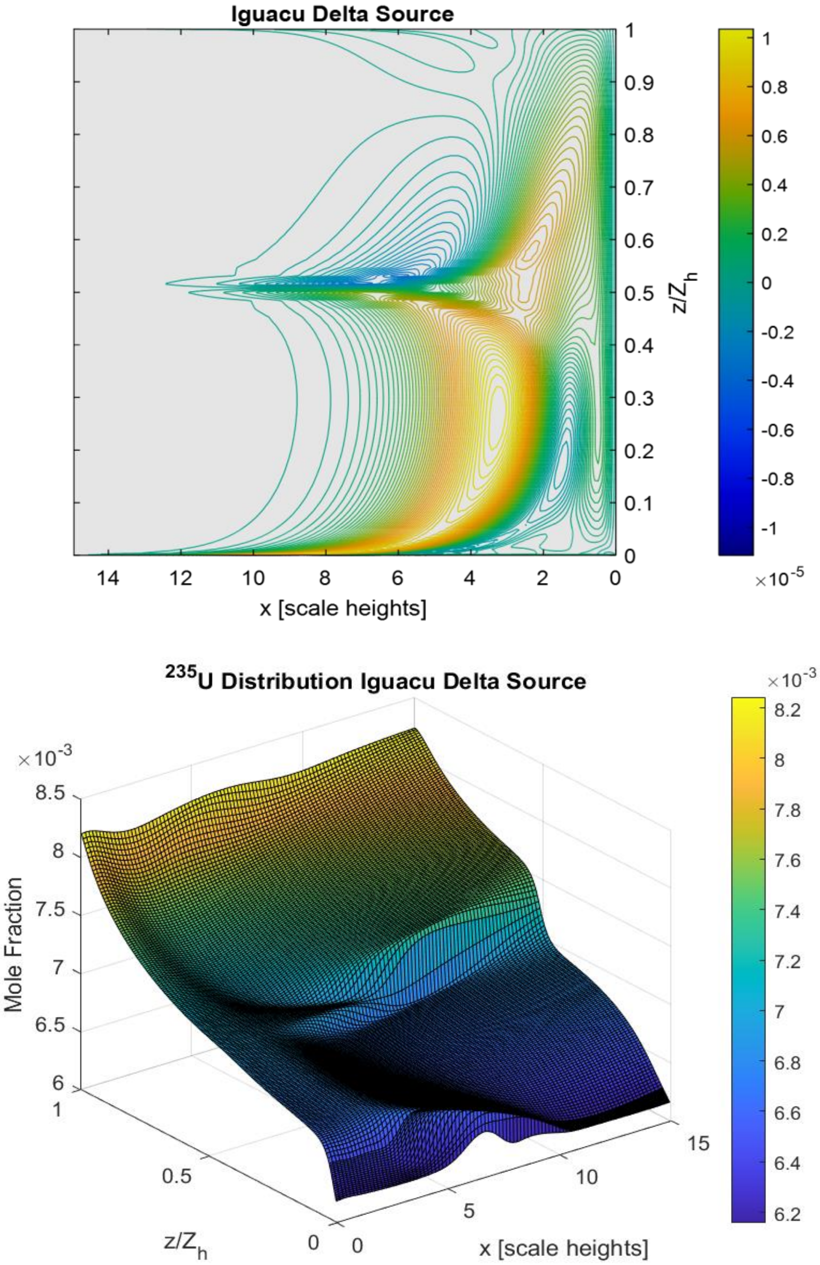

Figure 3.8: Streamlines of the total drive flow solution obtained using delta mass source at the feed (top) and the corresponding ^{235}U concentration gradient (bottom) using Iguaçu centrifuge

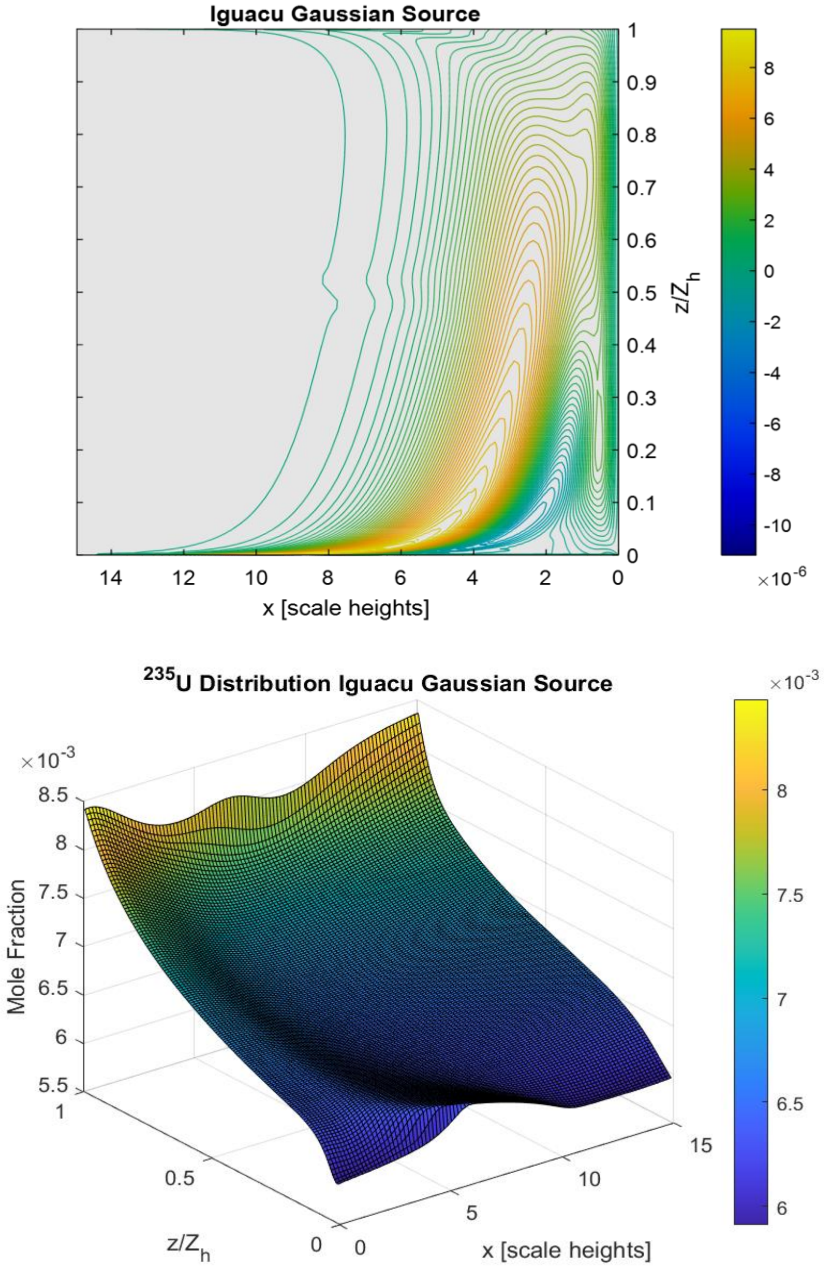

Figure 3.9: Streamlines of the total drive flow solution obtained using Gaussian mass source at the feed (top) and the corresponding ^{235}U concentration gradient (bottom) using Iguaçu centrifuge

The key distinction between the effects of the different functions on the countercurrent flow is on the severity of the separation of the upstream and downstream flows. The streamlines generated using the delta function in Figure 3.4 and Figure 3.8 show the sharpest division of the flow at the axial midpoint between the two halves of the centrifuge. This result is expected based on the mathematical derivation applied using the delta function as highlighted in Equations (3.21) -(3.27). The source defined in

Equation (3.21) has the Dirac delta function in both directions. While the discontinuous nature of the delta function is accounted for in the radial direction by smoothing its effects using integrations, it is elevated further in the axial direction by the derivative in Equation (3.22). This discontinuity in flow is translated onto the diffusion equation via the axial mass flux term and results in the sharp gradient around the axial midpoint as seen in the concentration distribution plot on the right side of Figure 3.4. The use of other source types reduces this nonphysical break in the concentration plots. Based on visual inspection of the flow streamlines and concentration surface plots, the linear step mass source function provides the smoothest solutions followed by the triangular source and the Gaussian. This can be explained by the fact that the finite element derivation of the flow equations makes use of the linear shape functions in the axial directions and thus the linear step source serves as the best fit to the approximation of the countercurrent flow. The Gaussian source can be improved to provide the smoothest solution by selecting a smaller value of the decay constant, α, which would prevent the source from deteriorating at a rapid rate and resulting in accelerated change.

To better quantify the variability between the sources, the normalized root-mean-square (RMS) difference of the stream functions and the ^{235}U concentration gradients is calculated. The normalized RMS, *d*, is given by the following equation:

$$d = \left[\frac{\int_0^{y_T}\int_0^{x_T}(\psi_1 - \psi_2)^2\,dx\,dy}{\int_0^{y_T}\int_0^{x_T}\psi_1^2\,dx\,dy}\right]^{\frac{1}{2}}, \qquad (3.28))$$

where ψ_1 is the stream function and/or concentration gradient matrix of source type 1 and ψ_2 is the corresponding matrix of source type 2.

Table 3.3 and Table 3.4 quantify the differences between each of the four sources and their effects on the flow and isotope diffusion for the two centrifuges. The delta function diverges the most from the rest of the sources as seen from Figure 3.4 and 3.8 and for the reasons discussed above. The triangular and Gaussian sources are analogous with the smallest RMS values, which can be anticipated due to their comparable shapes. The normalized RMS values for the concentration distribution are an order of magnitude smaller than those for the stream functions, which indicates the effect of the sources is greater on the mass flow than on the isotopic concentrations. This is expected since the 2-D diffusion equation only includes the axial mass flux term from the mass flow solution. While the isotopic separation is partially influenced by the mass flux, it is also affected greatly by the molecular weight differences between the isotopes and the gas density gradient in the centrifuge rotor volume that are not influenced by the type of source functions. The differences are greater for the smaller Iguaçu machine compared to the bigger Rome. This indicates that the aspect ratio of the machine affects the distribution of the flow inside the rotor. The smaller the rotor length, the lesser the axial distance available for the feed to spread as it enters the interior and interacts with the rotating flow. Thus, the mass flow and diffusion equations are more sensitive to the source functions used to model such axial spreading leading to greater differences shown in Table 3.4

Table 3.3: Normalized RMS of the stream function and concentration gradient between each of the sources for the Rome machine

Source Types, (ψ_1 $vs.$ ψ_2)	***d*** **(Stream Function)**	***d*** **(^{235}U Concentration Distribution)**
Triangle vs. Gaussian	0.009584	0.001318
Triangle vs. Linear Step	0.15313	0.01304
Linear Step vs. Gaussian	0.15298	0.01293
Triangle vs. Delta	0.19373	0.0150
Gaussian vs. Delta	0.18399	0.0140
Linear Step vs. Delta	0.26827	0.01360

Table 3.4: Normalized RMS of the stream function and concentration gradient between each of the sources for the Iguaçu machine

Source Types, (ψ_1 $vs.$ ψ_2)	***d*** **(Stream Function)**	***d*** **(^{235}U Concentration Distribution)**
Triangle vs. Gaussian	0.03802	0.00211
Triangle vs. Linear Step	0.5682	0.03824
Linear Step vs. Gaussian	0.5634	0.03670
Triangle vs. Delta	0.4675	0.1083
Gaussian vs. Delta	0.4377	0.1089
Linear Step vs. Delta	0.6446	0.1149

3.5 Conclusions

Four different mathematical functions were taken from literature and incorporated into the finite element solution for the mass flow inside a gas centrifuge to comprehend their effects on the source distribution. These source functions alter the streamlines of the flow as well as the isotopic concentration distribution with the greatest changes seen with the Dirac delta function. The discontinuity of the delta function needs to be lessened using smoothing techniques such as the one described in Wood and Sanders [36]. The other three sources provide relatively similar flow solutions. The impact on the concentration distribution is less than that on the mass flow since it is dictated not only by mass flux but also by the pressure and back diffusion of isotopes. The linear step function and the Gaussian distribution provide the smoothest countercurrent flow solutions and are anticipated to be the best representation of the physics in the gas centrifuge. The solutions presented in the rest of this dissertation utilizes the linear step function to model the mass source at the feed. This was done since this function allows the smoothest solutions even at higher values of feed rates while the rest of the sources tend to introduce the abnormality described above as the strength of the source increases. Future work can include the modification of the mass flow model that can accept any arbitrary function type with continuous derivatives of users' choosing to represent the sources and sinks of mass, momentum, and energy.

Chapter 4

Two-Dimensional Multi-Isotope Separation Using Finite Element Analysis

4.1 Overview

The background regarding the diffusion equation inside the centrifuge rotor and some of the key numerical models on the topic were discussed in Chapter 2. Following the enhancement of the mass flow solution as presented in Chapter 3, the axial mass flux matrix obtained is used to develop a more comprehensive solution of the isotopic diffusion here. A finite element model of a gas centrifuge is created to compute the optimal two-dimensional multi-isotope separation. The flow field generated using Onsager-Maslen equation without the pancake approximation is used as an input to the diffusion equation for each uranium isotope in the initial form of partial differential equations (PDE). The PDEs are reduced to their weak forms and the resulting integrals evaluated using gauss quadrature. The systems of equations are solved using an optimization routine to satisfy the overall mass and concentration balance inside the machine. The solutions provide a holistic view of isotopic diffusion inside the centrifuge and the ability to quantify the molecular fraction of various uranium isotopes at a given radial and axial location at any desired initial and operating conditions. While several authors in the past have solved the multi-isotope diffusion problems using 1-D approximations, there are no known 2-D finite element models in literature. The findings of this work, therefore, are not only significant for the applications of nuclear non-proliferation but also a great analytic tool for nuclear scientific community.

The primary objective of this chapter is to quantify the separative capability of any arbitrary centrifuge given certain physical and operating parameters. This process involves mapping the spread of individual isotopes present in the feed gas and determining the concentration of each at every location in the centrifuge rotor. As cited in Chapter 2, the problem of isotopic diffusion inside a gas centrifuge has been studied previously in literature. However, the solutions are limited to binary mixtures of the ^{235}U and ^{238}U isotopes [48] [49] or 1-D simplifications of the multicomponent mixtures [52] [53] [54] [47]. A full two-dimensional distribution of isotopes in the centrifuge domain is important in minimizing uncertainties associated with determining machine's separation capability obtained from the simplified models.

It is also essential to account for multiple isotopes in the gas mixtures because in its natural state UF_6 consists of not only the ^{235}U and ^{238}U isotopes but also the ^{234}U isotope. Furthermore, recycled uranium can also contain traces of the ^{232}U and ^{236}U isotopes that are not considered in the binary mixture separation models. The ability to analyze multi-component mixtures provides flexibility in the use of the developed model to study the separation of stable or non-radioactive isotopes [50] [51], further demonstrating the influence of this work. Therefore, a higher fidelity model of the multi-component isotopic diffusion in a gas centrifuge has been developed using Finite Element Analysis (FEA). Majority of this chapter has been published in the *Journal of Physics* under the title "Two-Dimensional Multi-Isotope Separation in a Gas Centrifuge Using Finite Element Analysis" [61].

From Chapter 2, the non-linear 2-D partial differential equation describing the diffusion of isotope *k* in a gas mixture can be obtained as follows:

$$-\rho D * \frac{\partial^2 N_k}{\partial z^2} - \rho D * \frac{1}{r} * \frac{\partial}{\partial r}\left[r * \frac{\partial N_k}{\partial r} - \frac{\Omega^2 r^2}{RT}\left(M_k - \sum_{j=1}^{n} M_j N_j \right) * N_k \right] + \rho V_z * \frac{\partial N_k}{\partial z} = 0 \qquad (4.1)$$

Equation (4.1) neglects the radial convection term $\rho V_r * \frac{1}{r}\left(\frac{\partial N_k}{\partial r}\right)$ from the continuity equation of fluid dynamics based on the assumption that the radial component V_r of the velocity is predominant over the axial component V_z only in the very thin Ekman layers near the end caps of the machine. The boundary conditions are listed in Equations (2.51) – (2.54). The definitions of the appropriate variables for Equation (4.1) are as follows:

ρD → Constant self-diffusion coefficient for UF_6, N_k → Mole fraction of isotope *k*, Ω → Angular velocity of the centrifuge, R → The specific gas constant, T → The average temperature of the gas, M_k → The molecular weight of the kth component, ρV_z → Axial mass flux obtained from Onsager's equation without the pancake approximation including the source and sink terms, (r, z) → The radial and axial directions of the centrifuge domain respectively.

Two important parameters used to quantify the separation capability of a gas centrifuge are the overall separation factor, γ, and the separative work, ΔU.

$$\gamma = \frac{N_P}{1-N_P} * \frac{1-N_W}{N_W} \qquad (4.2)$$

N_P and N_W are the concentrations of the ^{235}U isotope at the product and the tails, respectively.

$$\Delta U = F\, \theta V(N_P) + (1 - \theta)\, V(N_W) - V(N_F), \qquad (4.3)$$

where F is the feed flow rate, θ is the cut, and V is the value function [30].

4.2 Finite Element Approximation

The above-described set of 2-D nonlinear partial differential diffusion equations can be solved numerically using FEA. The centrifuge domain is described in Figure 4.1.

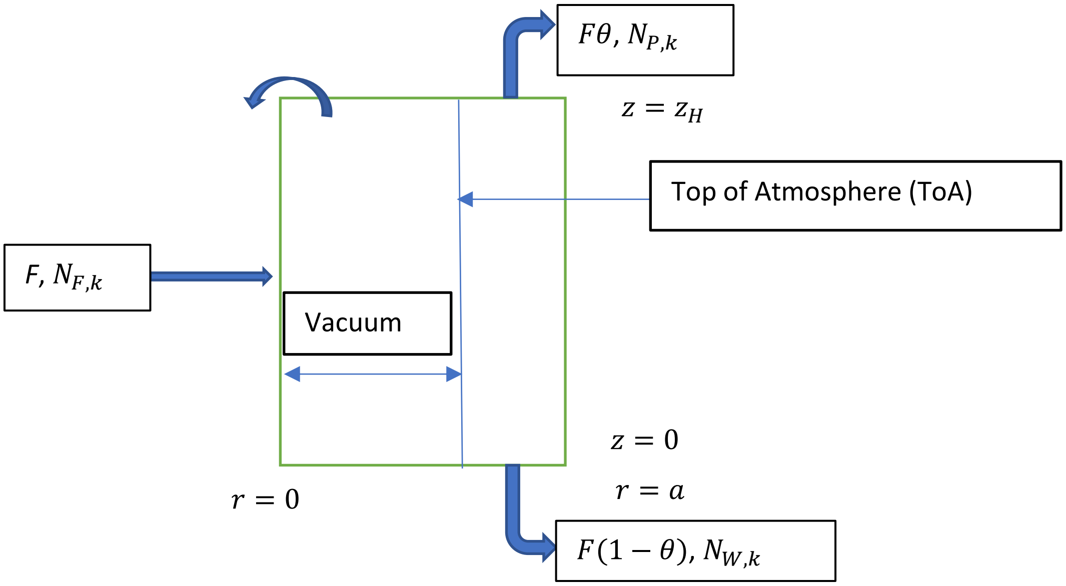

Figure 4.1: Centrifuge domain with one feed port and two extractors.

The 2-D axisymmetric centrifuge domain defined in Figure 4.1 can be discretized into several four-node rectangular elements. A sample element with its four nodes labelled is presented below in Figure 4.2 . The illustration of a sample mesh with centrifuge domain divided into rectangular elements can be seen in Figure 4.3 . It is imperative to determine the ideal number of elements required for accurate solution derivation. For this purpose, a mesh independence study has been conducted and will be discussed in the next section.

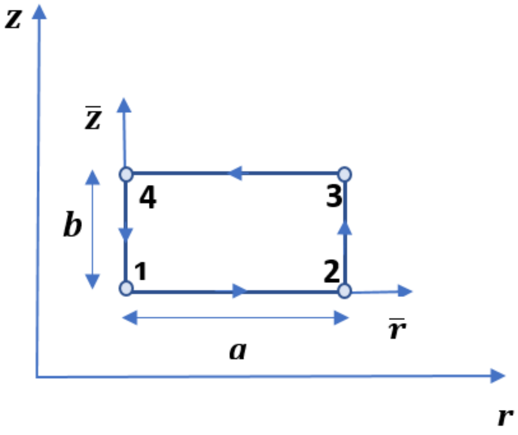

Figure 4.2: Linear four-node rectangular element

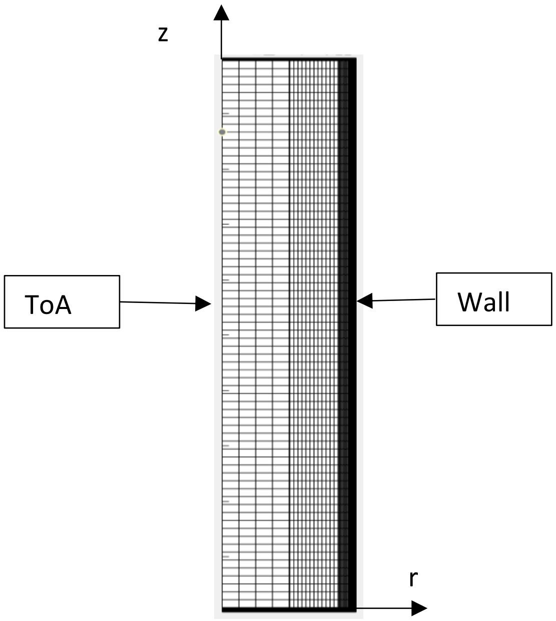

Figure 4.3. A sample mesh of the rectangular elements used to approximate the centrifuge domain. More elements are prescribed near the wall of the machine to capture the gradient effects.

Utilizing the above mesh, the diffusion equation can be simplified to solve for each individual element prior to solving for the entire domain. To ensure that Equation (4.1) can be solved element wise, it is important to develop its "weak" formulation to reduce the order of differentiation. Let,

$$H_k = \frac{\Omega^2}{RT}\left(M_k - \sum_{j=1}^{n} M_j N_j\right) \tag{4.4}$$

The weak form of Equation(4.1) above can be computed by first multiplying the entire equation by an arbitrary weighting function, $w(r, z)$, and integrating the product over the computational domain of the centrifuge.

$$\iint w(r,z) * \left(\frac{\partial^2 N_k}{\partial z^2} + \frac{1}{r} * \frac{\partial}{\partial r}\left[r * \frac{\partial N_k}{\partial r} - H_k * r^2 N_k \right] - \frac{\rho V_z}{\rho D} * \frac{\partial N_k}{\partial z} \right) d\Omega \; = 0 \qquad (4.5)$$

Taking each term separately and conducting integration by parts results in the following expressions:

$$\iint w * \frac{\partial^2 N_k}{\partial z^2} * r dr dz = \int_{r=0}^{r=a} \left(w \frac{\partial N_k}{\partial z} /_{0}^{z_H} - \int_0^{z_H} \frac{\partial N_k}{\partial z} * \frac{\partial w}{\partial z} dz \right) r \, dr \qquad (4.6)$$

$$\iint \mathrm{w} \left(\frac{\partial}{\partial \mathrm{r}} \left[\mathrm{r} \frac{\partial \mathrm{N_k}}{\partial \mathrm{r}} - \mathrm{H_k} \mathrm{r}^2 \mathrm{N_k} \right] \right) dr dz = \int_{\mathrm{z=0}}^{\mathrm{z=z_H}} \begin{pmatrix} \mathrm{w*r} \left(\frac{\partial \mathrm{N_k}}{\partial \mathrm{r}} - \mathrm{H_k r N_k} \right) | \begin{matrix} \mathrm{a} \\ 0 \end{matrix} - \\ \int_0^{\mathrm{a}} \left(\frac{\partial \mathrm{N_k}}{\partial \mathrm{r}} - \mathrm{H_k r^2 N_k} \right) \left(\frac{dw}{dr} \right) \mathrm{r \, dr} \end{pmatrix} dz \qquad (4.7)$$

$$- \frac{\rho \mathrm{V_z}}{\rho D} * \iint \mathrm{w} * \frac{\partial \mathrm{N_k}}{\partial \mathrm{z}} r dr dz = - \frac{\rho \mathrm{V_z}}{\rho D} * \int \mathrm{w*N_k} | \begin{matrix} \mathrm{z_H} \\ 0 \end{matrix} - \int_0^{\mathrm{z_H}} \mathrm{N_k} \, dw \, dz \, r \, dr \qquad (4.8)$$

Applying the appropriate boundary conditions and combining the terms, the weak form is obtained as follows

$$\iint_{r=0,z=0}^{\mathrm{r=a,z=z_H}} \frac{\partial \mathrm{N_k}}{\partial \mathrm{z}} * \frac{\partial \mathrm{w}}{\partial \mathrm{z}} + \frac{\partial \mathrm{N_k}}{\partial \mathrm{r}} * \frac{\partial \mathrm{w}}{\partial \mathrm{r}} - \mathrm{H_k * r^2 N_k} \left(\frac{\partial \mathrm{w}}{\partial \mathrm{z}} \right) - \frac{\rho \mathrm{V_z}}{\rho D} \left(\frac{\partial \mathrm{w}}{\partial \mathrm{z}} \right) \mathrm{N_k} r \, dr \, dz = 0 \qquad (4.9)$$

4.3 Interpolation Functions

The FEM approximates $N_k(r, z)$ over an element Ω^e as $N_k^e(r, z)$. N_k^e must be differentiable as required in the weak form of the problem, the polynomials used to represent N_k^e must be complete and all terms in the polynomial should be linearly independent. For an element with four nodes as shown in Figure 4.2, the polynomial

$$N_k^e(r, z) = c_1 + c_2 r + c_3 z + c_4 r z \qquad (4.10)$$

can be used to interpolate the mole fraction of isotope *k* in an element *e*. In Equation, $c_i's$ are arbitrary constants to be determined later. The interpolation function should represent the nodal variables at the four nodal points of the element. Therefore, substituting the *r* and *z* values at each nodal point gives

$$\begin{Bmatrix} N_{k1} \\ N_{k2} \\ N_{k3} \\ N_{k4} \end{Bmatrix} = \begin{bmatrix} 1 & r_1 & z_1 & r_1 z_1 \\ 1 & r_2 & z_2 & r_2 z_2 \\ 1 & r_3 & z_3 & r_3 z_3 \\ 1 & r_4 & z_4 & r_4 z_4 \end{bmatrix} * \begin{Bmatrix} c_1 \\ c_2 \\ c_3 \\ c_4 \end{Bmatrix} \tag{4.11}$$

Here, r_i and z_i are the coordinate values at the i^{th} node and N_{ki} is the nodal value of mole fraction of isotope *k*. The constants $c_i's$ can be obtained by multiplying both sides of Equation (4.11) by the inverse of the matrix. Substituting the resulting equations for the constants back into Equation (4.10) results in

$$N_k^e = \sum_{i=1}^{4} \psi_i^e(r,z) N_{ki} \tag{4.12}$$

where $\psi_i^e(r,z)$ are the shape functions for linear rectangular element:

$$\psi_1^e = \left(1-\frac{r}{a}\right)\left(1-\frac{z}{b}\right), \quad \psi_2^e = \frac{r}{a}\left(1-\frac{z}{b}\right), \quad \psi_3^e = \frac{r}{a}\left(\frac{z}{b}\right), \quad \psi_4^e = \left(1-\frac{r}{a}\right)\left(\frac{z}{b}\right) \tag{4.13}$$

Here *a* and *b* are the element length and width respectively as illustrated in Figure 4.2. Letting the weighting function $w(r.z) = \sum_{i=1}^{4} \psi_i N_{ki}$ and substituting into Equation(4.9), the weak form of the diffusion equation can be re-written in terms of the shape functions for each element. The double integral in the weak form of the equation is evaluated using Gaussian quadrature to obtain the element stiffness matrix, $[K^e]$. Such process is repeated for every element in the centrifuge mesh and each of the individual element matrices are assembled into the system stiffness matrix, $[K]$. The system stiffness matrix is a diagonally dominant sparse matrix whose size is equal to system degrees of freedom (sdof) x (sdof). The total system degrees of freedom are evaluated by multiplying the total number of unknowns per node by the total number of nodes in the mesh. Thus, the system equation to be evaluated can be written as follows:

$$[K]_{sdof*sdof} * \{N_k\}_{sdofx1} = \{f\}_{sdofx1} \tag{4.14}$$

The mole fraction of isotope *k* is unknown everywhere in the centrifuge domain except for the nodes corresponding to the feed region, where the feed values are known. This ensures that the right-hand side vector *f* in Equation (4.14) is non-zero. The solution of Equation (4.14) is obtained by solving for the concentration vector using Matlab's "mldivide" function.

$$\{N_k\}_{sdof\ x\ 1} = [K]_{sdof*sdof} \backslash \{f\}_{sdof\ x\ 1} \tag{4.15}$$

A complete finite element derivation of the diffusion equation is provided in Appendix I. The newly developed code named *MultiPort* builds the coefficient matrix and force vector and solves the matrix in

Equation (4.15) using built-in algorithms. The built-in routine selects the most appropriate method from several different solving techniques, including QR decomposition, a triangular solver, a permutated triangular solver, LDL decomposition, LU decomposition, a Hessenberg or Cholesky solver, a diagonal solver, or a banded solver depending on the characteristic of the coefficient matrix, K. A flow diagram highlighting the key features and workflow of *MultiPort* is presented in Appendix II. The finite element solver is designed to satisfy several physical properties of the diffusion equation to ensure convergence. The key criteria required to ensure accurate solution are as follows:

1) The sum of the molecular weights of the isotopes multiplied by the concentrations of each at every nodal point equals the molecular weight of the gas. For UF_6 mixture, $\sum_{i=1}^{n} M_i * N_i = 352 \frac{kg}{mol}$, where n= total number of isotopes present, M_i= molecular weight of each isotope *i* and N_i= mole fraction of isotope *i*.
2) The sum of the concentration of all of the isotopes at every nodal point is 1: $\sum_{i=1}^{n} N_i = 1$.
3) The overall balance of isotopic species is established.

$$N_{F,K} = \theta N_{P,K} + (1-\theta) N_{W,K} \tag{4.16}$$

Here, $N_{F,K}$, $N_{P,K}$, and $N_{W,K}$ are the concentrations of isotope k at the feed, product, and tails end respectively. Equation (4.16) needs to be satisfied for all the isotopes present in the gas mixture for the solution to converge.

4.4 Results

The output of the new finite element model, *MultiPort,* has been examined using hypothetical gas centrifuges. The physical as well as the operating parameters of Rome [62], Iguacu [60] , and Darmstadt [63] machines found in literature are described previously in Chapter 3 and reiterated in Table 4.1 below. The diffusion results here are presented for the Rome and Iguacu machines operated at 600 m/s and Darmstadt machine at 800 m/s.

Table 4.1: Physical properties of the fictitious gas centrifuges

Parameter	Variable	Unit	Rome	Iguaçu	Darmstadt
Radius	a	*m*	0.25	0.06	0.25
Length	z_H	*m*	5	0.48	15
Average gas temperature	T	*K*	320	300	340
Wall pressure	p	*torr*	100	60	500
Cut	θ	-	0.5	0.5	0.10227

The isotopic composition of the UF_6 gas at the feed is given in Table 4.2. These values for spent reactor uranium fuel are specified in ASTM C787-06 Standard Specification for Uranium Hexafluoride for Enrichment found in *Nuclear Material Safeguards for Uranium Enrichment Plants* [64].

Table 4.2. Isotopic composition of the feed gas [molecular %].

Isotope	**%**
^{232}U	10^{-9}
^{234}U	0.02
^{235}U	0.9
^{236}U	0.4
^{238}U	98.68

Before Equation (4.1) can be solved, the solution of the mass flow is required. As detailed in Chapter 3, for this work, the gas flow field inside the centrifuges was generated using the *CurvSOL* code developed by Witt [42] and later modified by Thomas [43]. The optimal values of the linear wall temperature, scoop drag force, and the feed rate were combined to simulate the total drive effects in the UF_6 gas flow. *CurvSOL* includes the sources and sinks of mass, momentum, and energy and considers the effect of rotor curvature in the obtained solutions. The mass that is introduced by the feed at the axial midpoint is removed through scoops located at the top and the bottom ends of the machine. The bottom scoop is modeled as a sink of angular momentum while the top scoop is modeled as a boundary since it is shielded from the gas flow region by a baffle. Using the mass flux profile and the centrifuge mesh, *MultiPort* solves either the binary or the multi-component mixture based on the user input. A mesh independence study was conducted to evaluate the appropriate number of elements required for the centrifuge domain. The results are shown in Table 4.3.

Table 4.3. Mesh independence study to determine the optimal number of FEA nodes.

# of nodes	$\boldsymbol{\gamma}$	**% diff**	$\boldsymbol{\Delta U\left(\frac{SWU}{yr}\right)}$	**% diff**
4750	1.678	2.483	47.401	10.915
9500	1.721	0.510	52.874	2.727
19000	1.729	0.554	54.336	2.308
28500	1.739	0.596	55.605	2.118
38000	1.749	0.0229	56.795	0.0772
47500	1.749	0.672	56.751	2.382
57000	1.761	0.238	58.119	0.826
66500	1.765		58.601	

The total number of 38000 nodes or the 95x400 grid size, 95 nodes in the radial direction and 400 nodes in the axial direction, is deemed sufficient for the centrifuges in consideration. Any further increase in the number of nodes results in insignificant changes (less than 1%) of the separation parameters but larger than 20% increase in convergence time.

The 3-D surface plots of the individual isotopic diffusion are presented below for the Rome machine distribution. The surface plots in Figure 4.4 and Figure 4.6 show the concentration of specific isotope at the given radial and axial position inside the rotor volume. The x-axis is the non-dimensional radial location in scale heights from x=0 at the wall and x=15 at the “top of the atmosphere.” The y-axis shows the non-dimensional axial locations with y=0 at the bottom and y=1 at the top. The concentration of the isotope is given in the z-axis in molecular fraction.

(a)

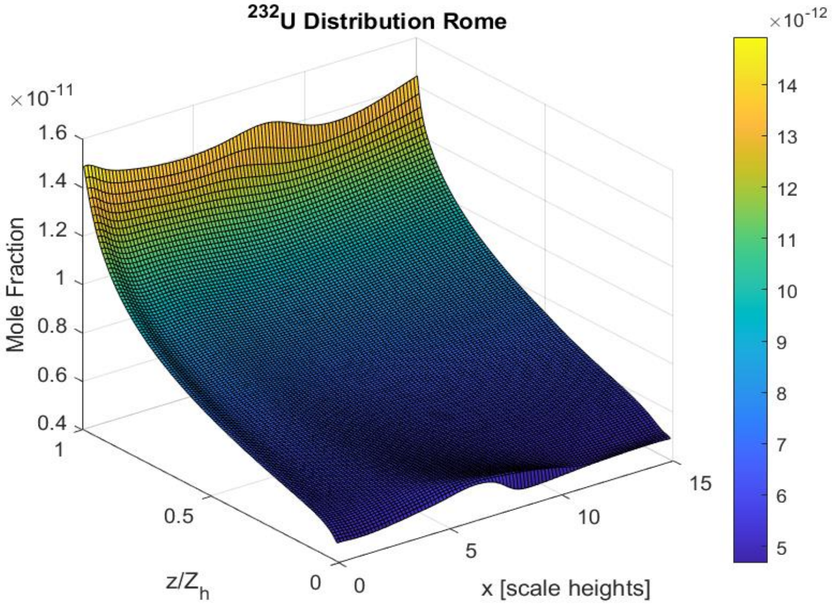

(b)

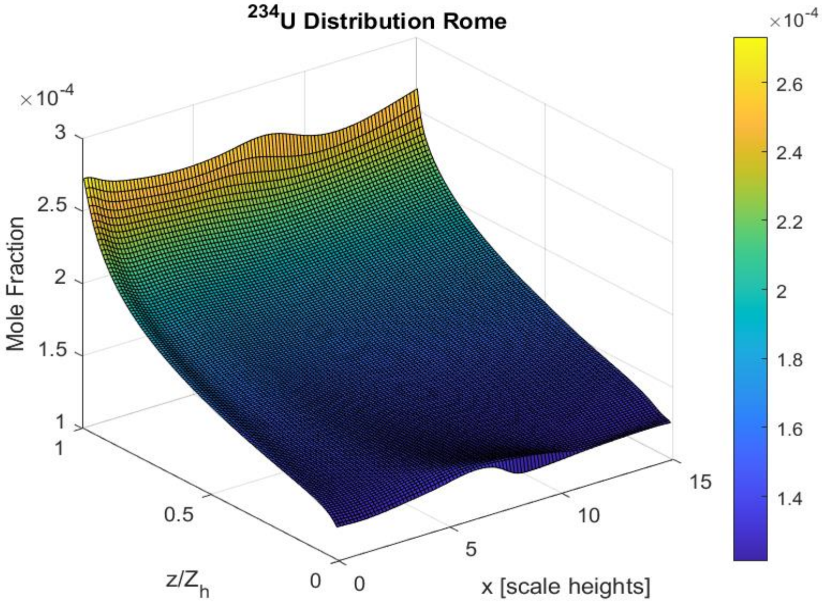
^{234}U Distribution Rome
Mole Fraction
$\times 10^{-4}$
3
2.5
2
1.5
1
z/Z$_h$
1
0.5
0
x [scale heights]
0
5
10
15
$\times 10^{-4}$
2.6
2.4
2.2
2
1.8
1.6
1.4

(c)

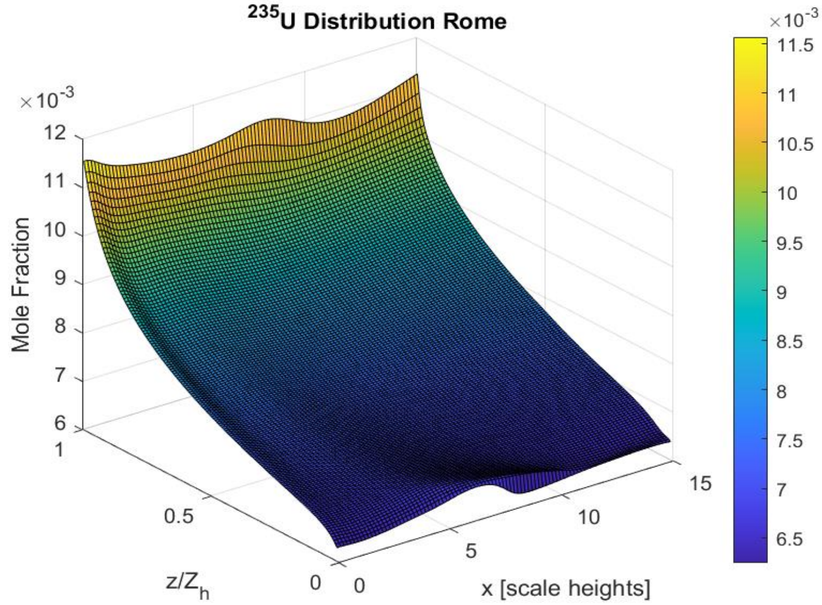
^{235}U Distribution Rome
Mole Fraction
$\times 10^{-3}$
12
11
10
9
8
7
6
z/Z$_h$
1
0.5
0
x [scale heights]
0
5
10
15
$\times 10^{-3}$
11.5
11
10.5
10
9.5
9
8.5
8
7.5
7
6.5

(d)

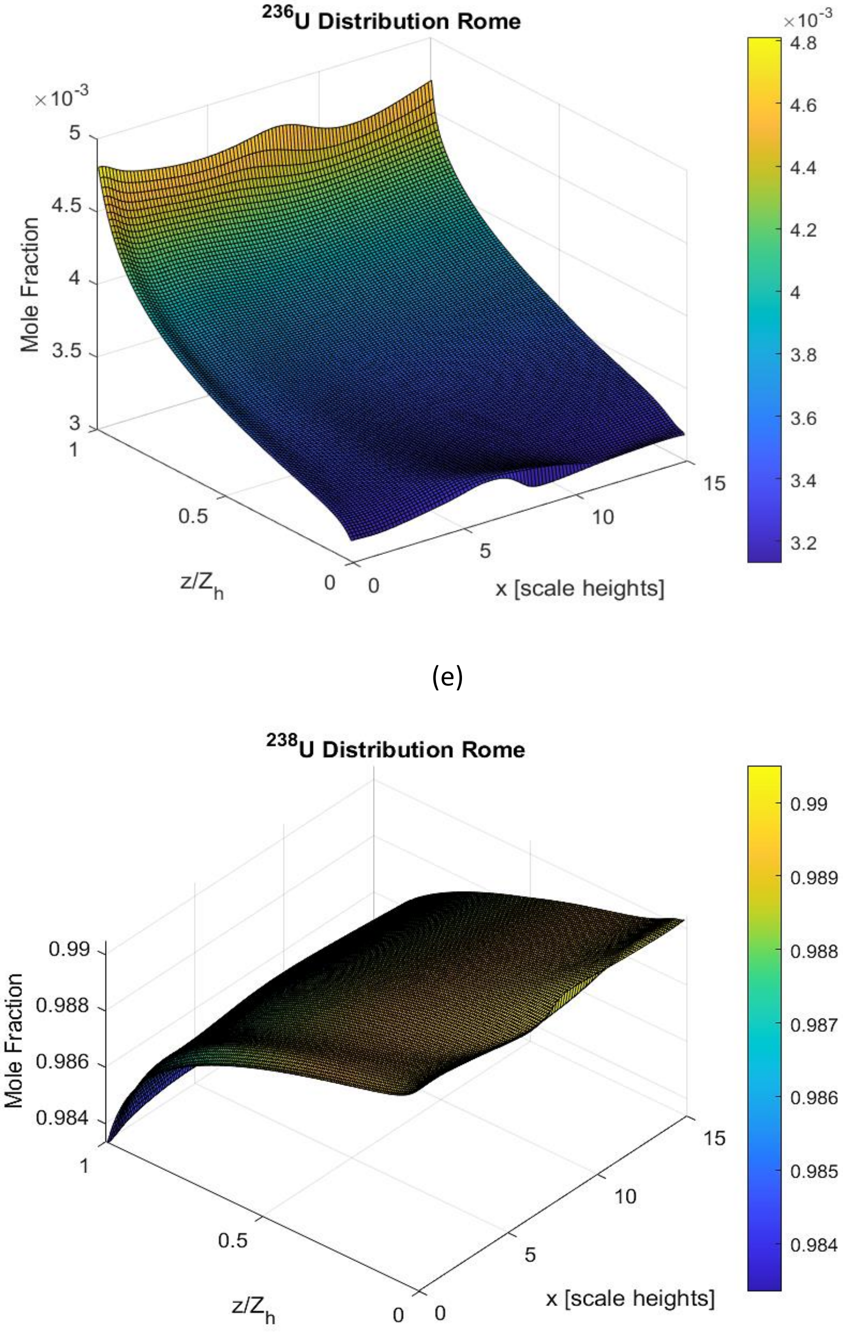

Figure 4.4: The 3-D surface plots showing the spread of individual uranium isotopes (a) ^{232}U, (b) ^{234}U, (c) ^{235}U, (d) ^{236}U, and (e) ^{238}U inside the Rome centrifuge rotor

The isotopic distribution plots show great agreements with the expected physics that the higher concentration of the lighter isotope is at the top end of the centrifuge rotor while a higher concentration of the heavier isotope is at the bottom end. For the ^{235}U surface plot in Figure 4.4(c), the concentration of the isotope increases with increasing axial distance from the feed location at the axial midpoint towards the top while decreases with decreasing distance towards the bottom. The radial separation is noticeably minimal compared to the axial, with approximately only 5% increase in concentration between the rotor wall and the top of the atmosphere. The shape of the isotopic distribution plots for the minor isotopes ^{232}U, ^{234}U, and ^{236}U agree with that of ^{235}U. For the heavier ^{238}U isotope, the distribution is reversed with higher concentrations toward the bottom end of the machine and lower toward the top. One of the novel features of the new model is the ability to obtain radial variation of the isotopic concentrations, which was not possible in the older diffusion models. Figure 4.5 and Figure 4.7 show the radial distribution of the isotopes at four different axial points in the centrifuge rotor. On the bottom half of the machine, the heavier isotopes are heavily concentrated while at the top half, the lighter isotopes can be found in greater concentrations. The lighter isotopes are enriched at a greater rate towards the axis on the right while the heavier near the wall on the left. The radial variations at the end plates are negligible between the wall and the top of the atmosphere. This can be attributed to the fact that most of the flow at the ends is around the extraction points located radially somewhere in-between the wall and the axis.

(a)

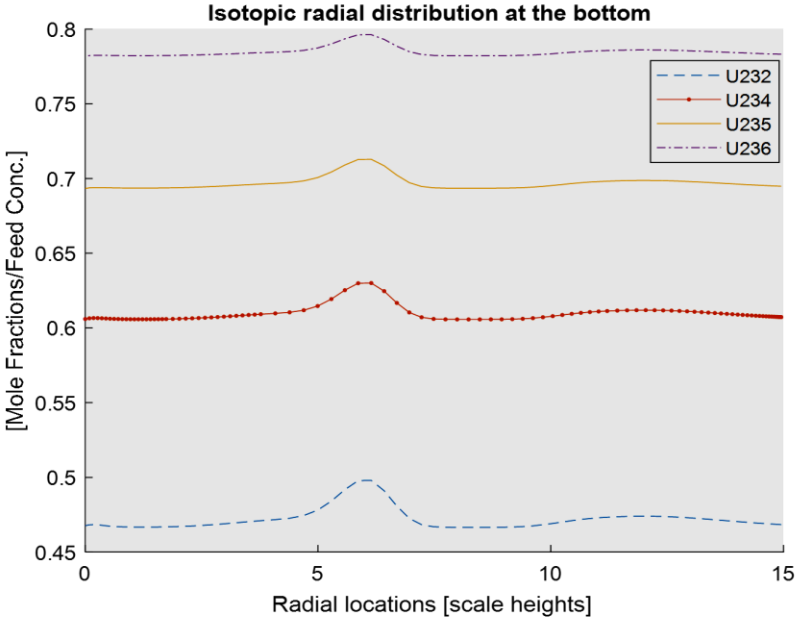

(b)

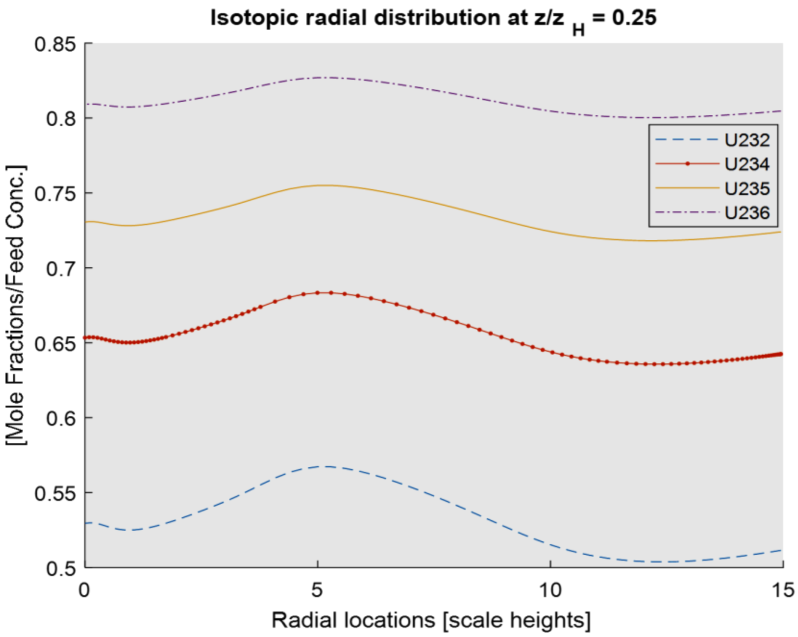
Isotopic radial distribution at z/z H = 0.25
[Mole Fractions/Feed Conc.]
0.85
0.8
0.75
0.7
0.65
0.6
0.55
0.5
0
5
10
15
Radial locations [scale heights]
U232
U234
U235
U236

(c)

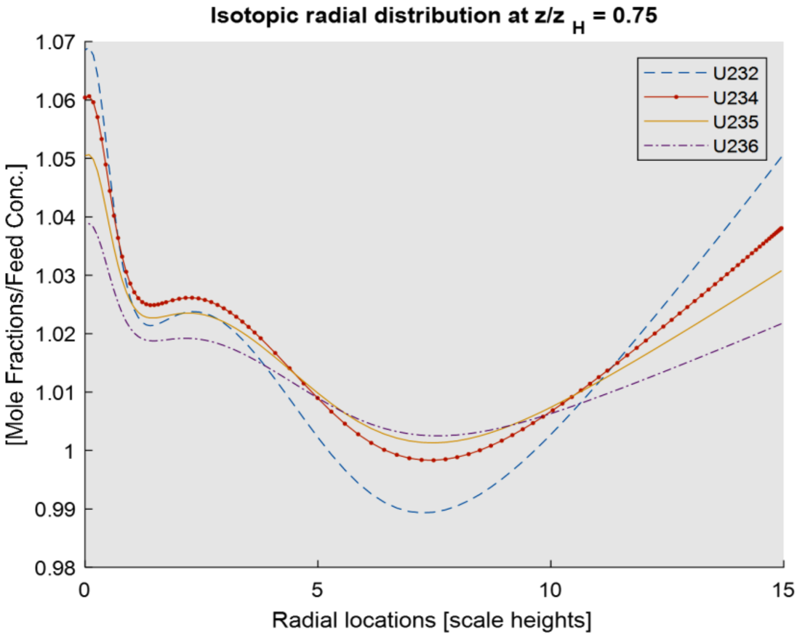
Isotopic radial distribution at z/z H = 0.75
[Mole Fractions/Feed Conc.]
1.07
1.06
1.05
1.04
1.03
1.02
1.01
1
0.99
0.98
0
5
10
15
Radial locations [scale heights]
U232
U234
U235
U236

(d)

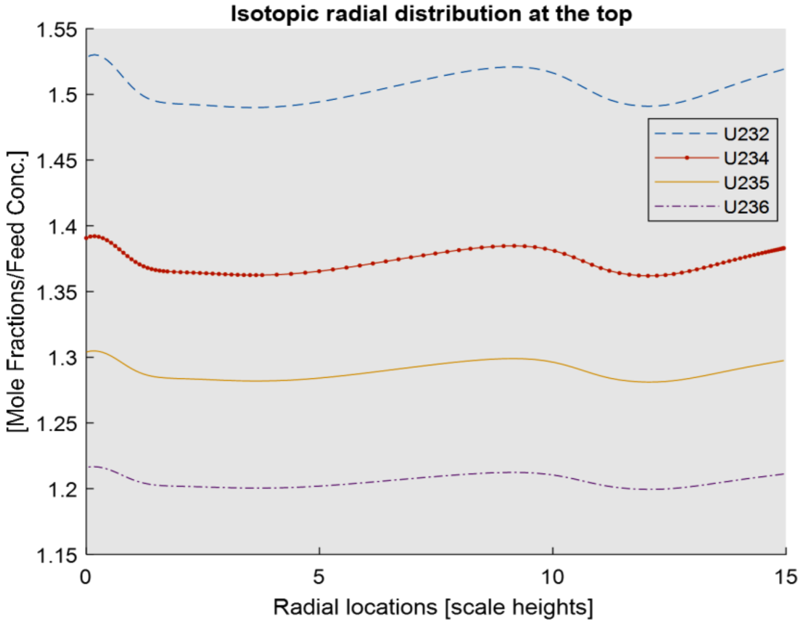

Figure 4.5: Radial concentration distributions normalized using the feed concentrations of the four minor uranium isotopes at four different axial locations (a) y=0, (b) y=0.25, (c) y=0.75, and (d) y=1 for the Rome machine.

The separation of isotopes in the Iguaçu rotor with the same feed assay as Rome machine above is presented below. The general trends of isotopic distribution are similar to the Rome case with lower magnitude of separation and the radial variations in the separation chamber.

(a)

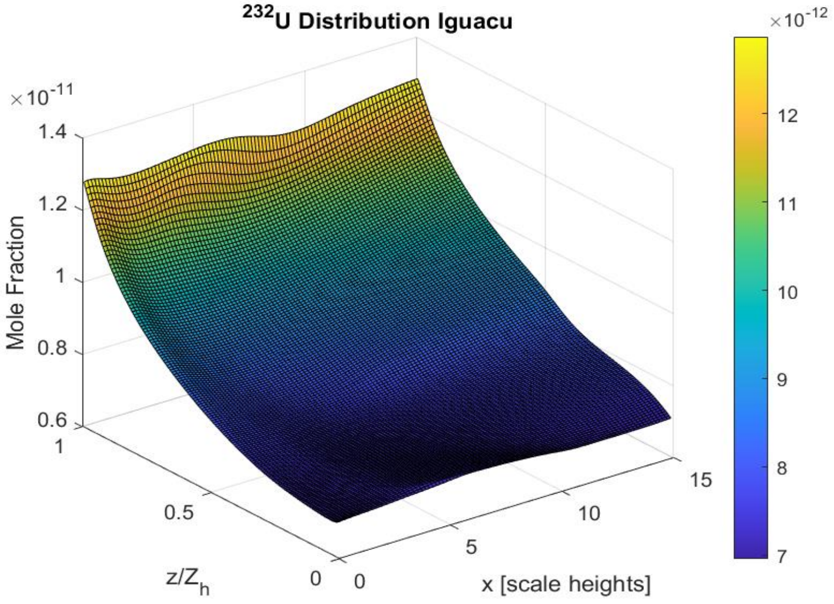

(b)

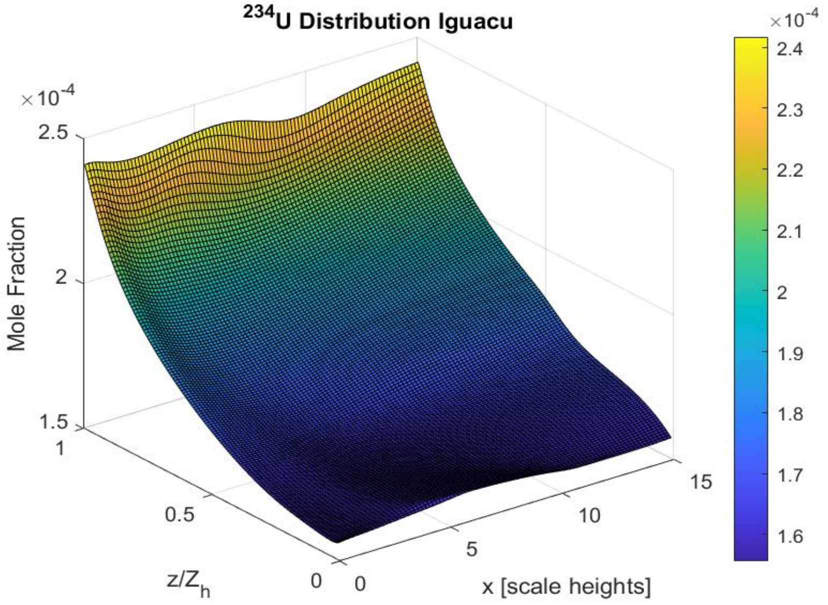

^{234}U Distribution Iguacu
×10^{-4}
2.5
2
1.5
Mole Fraction
1
0.5
0
z/Z$_h$
0
5
10
15
x [scale heights]
×10^{-4}
2.4
2.3
2.2
2.1
2
1.9
1.8
1.7
1.6

(c)

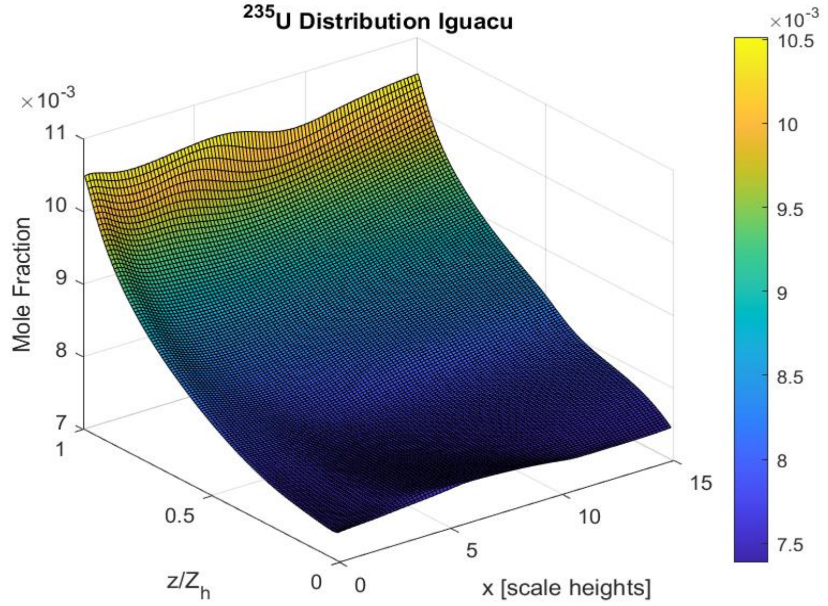

^{235}U Distribution Iguacu
×10^{-3}
11
10
9
8
7
Mole Fraction
1
0.5
0
z/Z$_h$
0
5
10
15
x [scale heights]
×10^{-3}
10.5
10
9.5
9
8.5
8
7.5

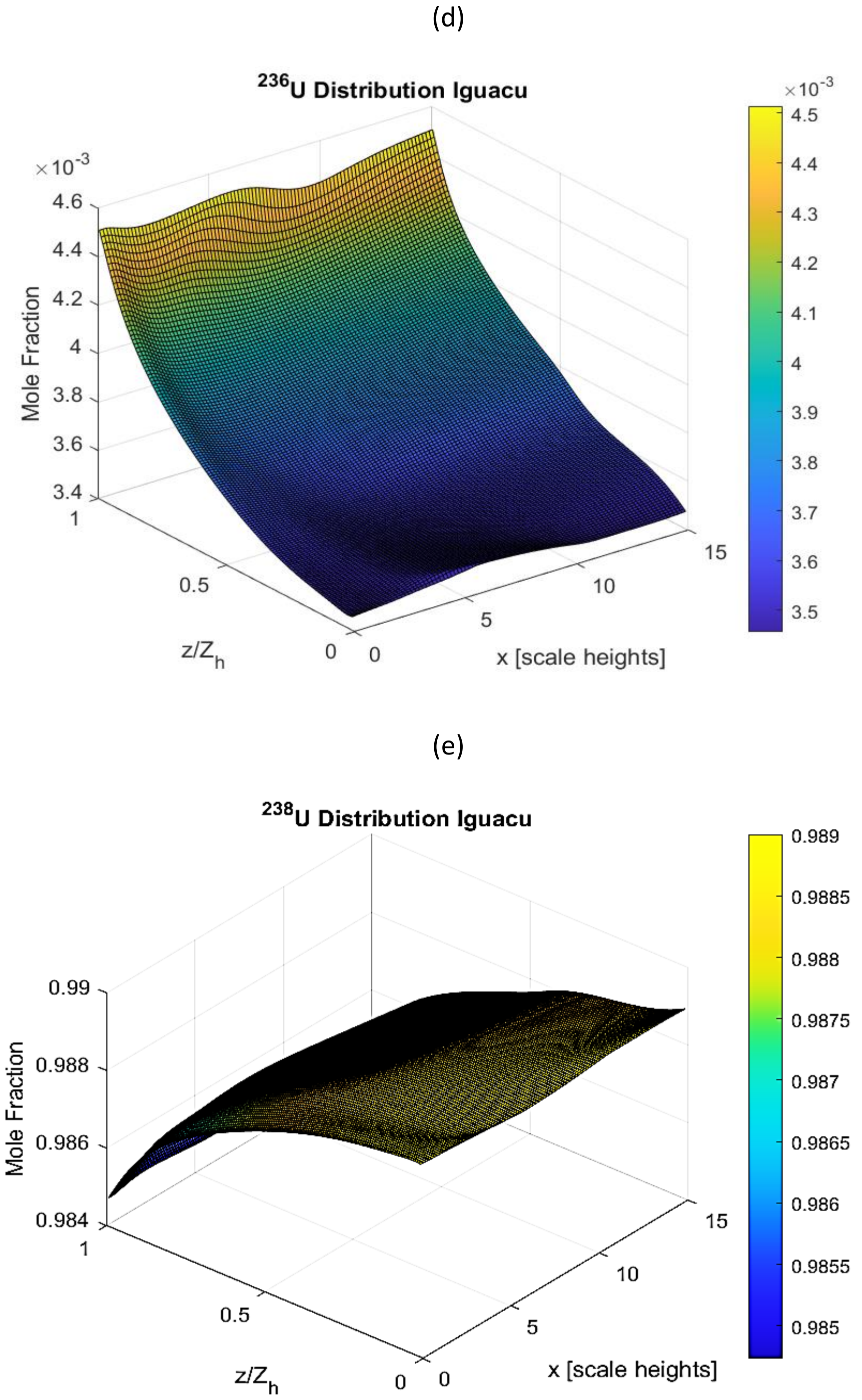

Figure 4.6: The 3-D surface plots showing the spread of individual uranium isotopes (a) ^{232}U, (b) ^{234}U, (c) ^{235}U, (d) ^{236}U, and (e) ^{238}U inside the Iguaçu centrifuge rotor

(a)

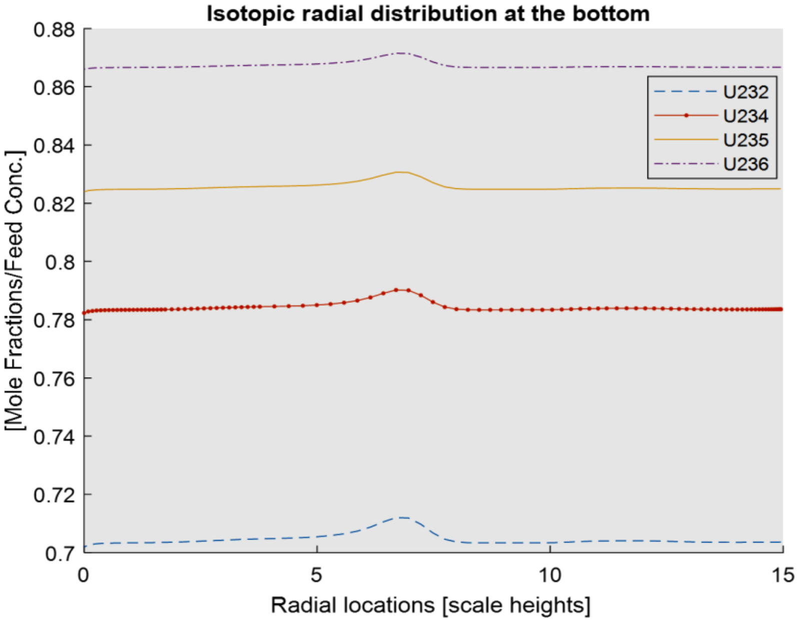

Isotopic radial distribution at the bottom
[Mole Fractions/Feed Conc.]
0.88
0.86
0.84
0.82
0.8
0.78
0.76
0.74
0.72
0.7
0
5
10
15
Radial locations [scale heights]
U232
U234
U235
U236

(b)

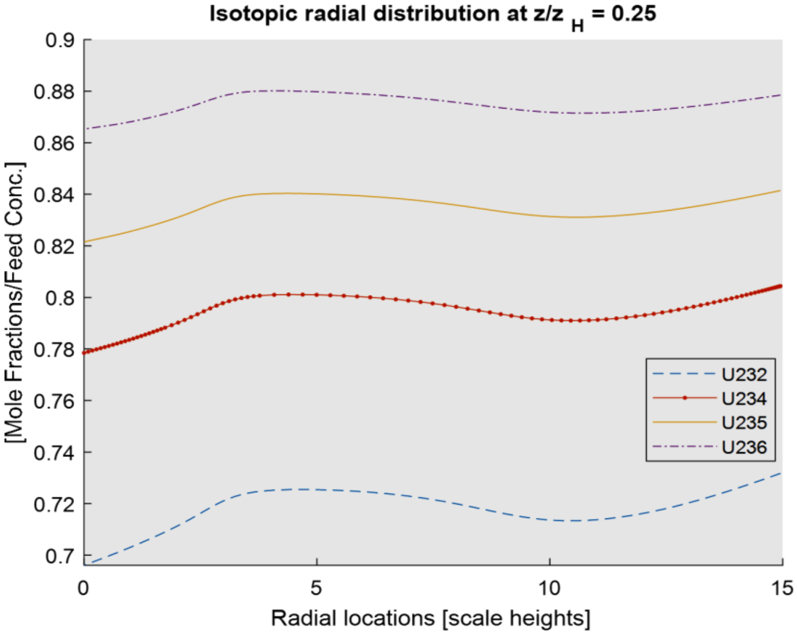

Isotopic radial distribution at z/z $_H$ = 0.25
[Mole Fractions/Feed Conc.]
0.9
0.88
0.86
0.84
0.82
0.8
0.78
0.76
0.74
0.72
0.7
0
5
10
15
Radial locations [scale heights]
U232
U234
U235
U236

(c)

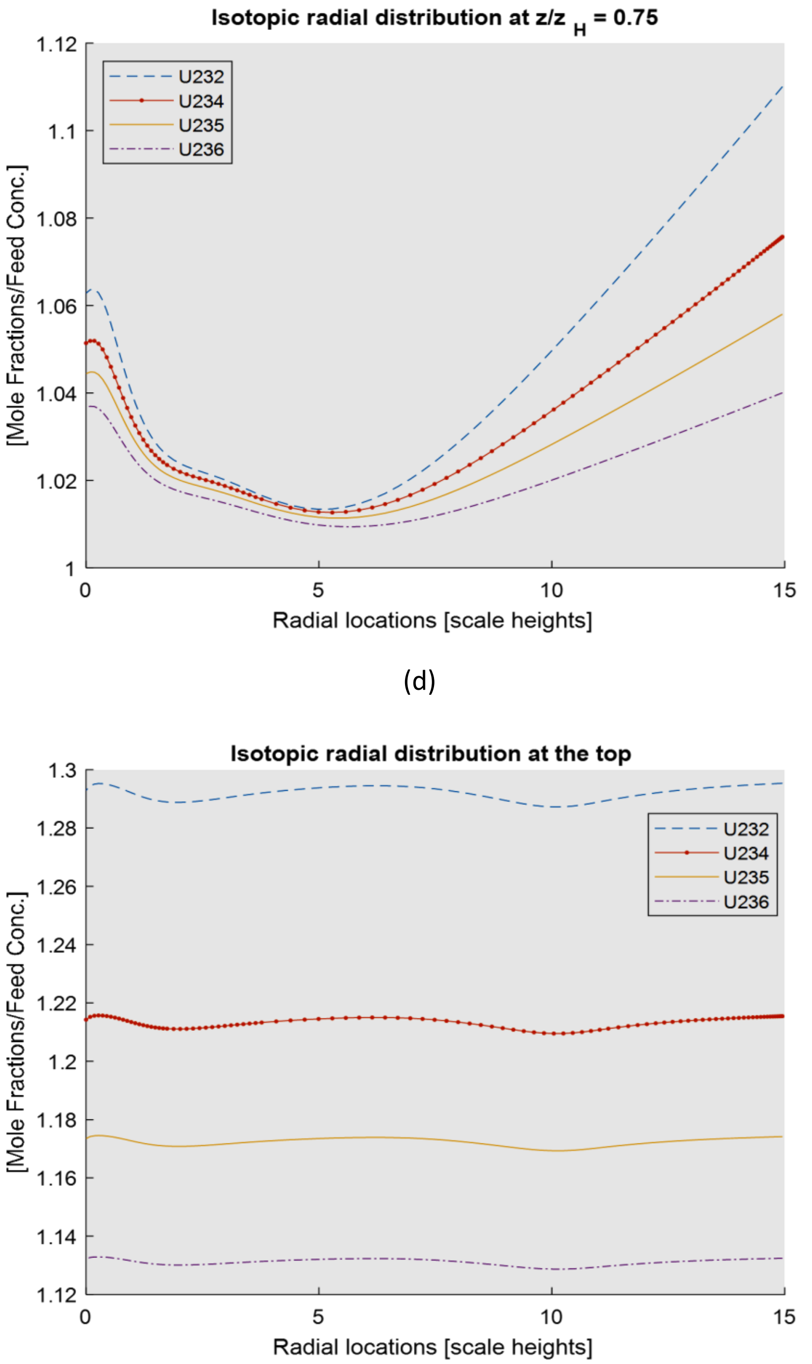

Figure 4.7: Radial concentration distributions normalized using the feed concentrations of the four minor uranium isotopes at four different axial locations (a) y=0, (b) y=0.25, (c) y=0.75, and (d) y=1 for the Iguaçu machine

The new 2-D model of the diffusion equations has been verified by comparing the results with the previously available simplified code. The comparison was done by radially averaging the solutions of the above output and comparing with the 1-D model [47]. The concentration values reported by the new *MultiPort* code are within 10% of the radially averaged concentrations obtained from the 1-D model. Since there are no known open-source experimental data available for the separation of uranium isotopes, the code has been verified against the experiments performed for the separation of stable isotopic mixtures. More specifically, the enrichment of chromium isotopes is simulated using the Darmstadt machine and compared against the values obtained by Szady [51]. The process gas employed was chromyl-fluoride (CrO_2F_2). The properties of the gas and the isotopic composition of the feed are defined in [47] as presented in Table 4.4 below. The isotope of interest is Chromium-50 and the cut of the machine is set at 0.10227 to target its enrichment. The countercurrent flow parameters used here are the same defined in [47]. It is important to note that the exact parameters of the centrifuge used by Szady in his experiments are unknown. However, since the work took place in Oak Ridge, Tennessee with American centrifuge designs, Darmstadt machine is assumed to be a great approximation of the actual centrifuge. While a direct comparison of the separation results cannot be performed here, it can be seen that the isotopics presented show excellent agreements. The streamlines of the feed flow followed by the isotopic distributions are included below in Figures 4.8-4.10.

Table 4.4: Properties of chromyl-fluoride used in the simulation for the separation of chromium isotopes

Parameter	Unit	Value	
Average gas temperature	K	315	
Gas pressure at the wall	Torr	50	
Molecular weight	g/mol	122	
Viscosity	Kg/(m*s)	1.40e-5	
Thermal conductivity	W/(m*k)	0.00675	
Ratio of specific heats	-	1.12	
Schmidt number	-	0.75	
Isotopic composition of the feed	[atm %]	Cr-50	4.35%
		Cr-52	83.79%
		Cr-53	9.50%
		Cr-54	2.46%

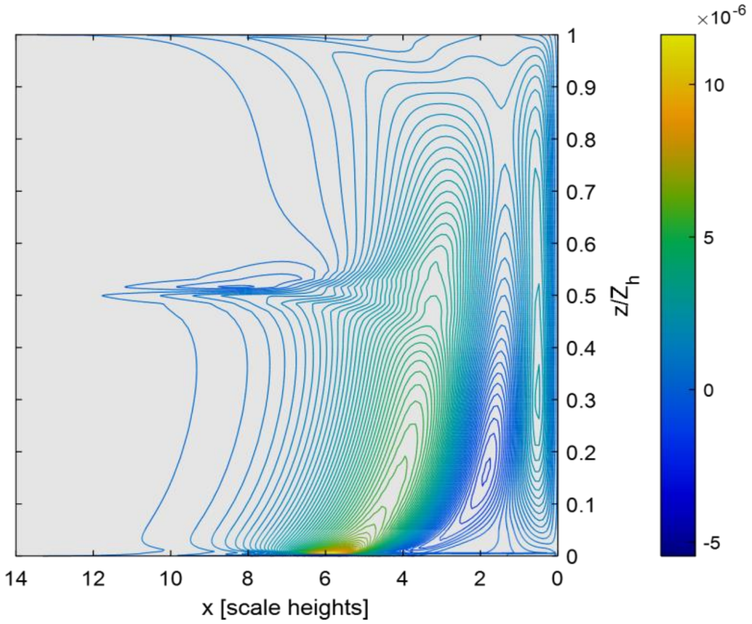

Figure 4.8: Streamlines of the flow for chromyl-fluoride gas inside the Darmstadt machine rotor. The feed rate is 50 mg/s and the scoop drag force at the bottom is 5512 dynes.

The countercurrent flow in Figure 4.8 is dominated by the drag force exerted by the scoop located at x = 6. The 3-D distribution of the Cr-50 isotope is presented in Figure 4.9 and the radially averaged concentrations of all of the isotopes in Figure 4.10. It can be seen that the majority of the separation occurs at the top half of the centrifuge. This is a phenomenon resulting from the use of the small value of machine cut. Only 10% of the flow is extracted out from the product end and 90% exits out of the tails end. This results in minimal separation at the bottom half of the machine. The concentrations at the extraction points of the machine are compared against those measured by Szady in his experiments. Table 4.5 shows the concentrations and the percent differences between the two solutions. It is shown that the values obtained from the developed code agree well with the experimental data. The differences can be attributed to the unknown exact parameters of the machine used in the experiment as well as on the missing data quantifying the uncertainty associated with the experimental measurements. Additional detailed validation of the model through quantification of uncertainty and sensitivity analysis is presented in Chapter 5.

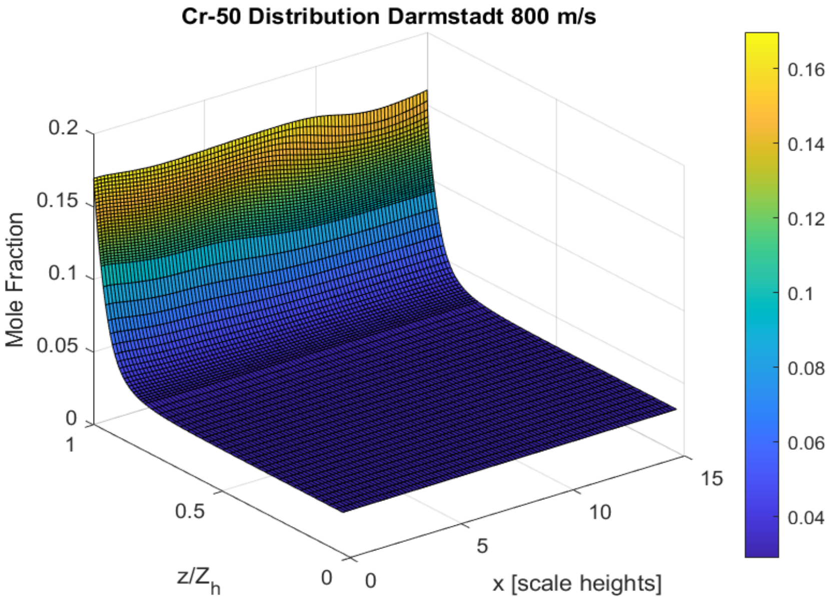

Figure 4.9: Cr-50 isotopic distribution inside the Darmstadt machine rotor

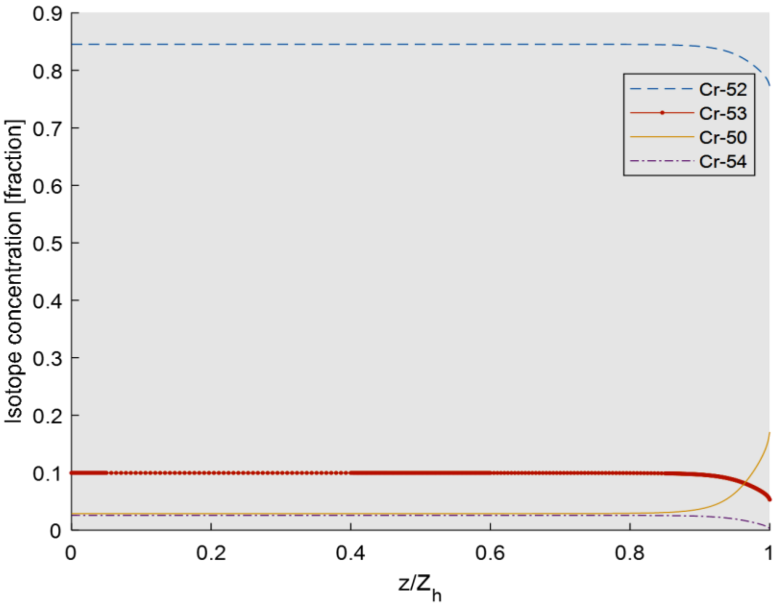

Figure 4.10: Radially averaged concentrations of the chromium isotopes. The plots resemble the 1-D solutions obtained in [47].

Table 4.5: Comparison of the end concentrations for chromium separation between experimental data and MultiPort code

Isotope	**Product-Szady [%]**	**Product-*MultiPort* [%]**	**% difference**	**Waste-Szady [%]**	**Waste-*MultiPort* [%]**	**% difference**
Cr-50	16.2	16.56	2.198	3.0	2.90	3.390
Cr-52	74.4	77.57	4.172	84.3	84.53	0.272
Cr-53	4.0	5.50	31.579	10.1	9.97	1.295
Cr-54	0.40	0.37	7.792	2.6	2.59	0.385

4.5 Summary and Conclusions

The 2-D diffusion equation has been solved using the newly developed finite element code to calculate the multi-isotopic gradients inside a single centrifuge machine. The finite element model utilized linear quadrilateral elements to approximate the mole fractions of an arbitrary number of isotopes present in the process gas. This work is beneficial in examining the two-dimensional variation of uranium isotopes that was not available in the past. The new code is designed to solve either the binary mixture or the multi-isotopic mixture according to user's preference. This feature allows the user to not only limit the calculations to uranium hexafluoride but also to non-radioactive and stable isotopic mixtures. The information obtained here can be used to determine the machine's separative capability as well as visualize and understand the distributions of individual isotopes inside the rotor volume. The new model not only provides the concentrations of uranium isotopes at the outlets of the machines but also information about how the isotopes are distributed in the interior regions. This type of knowledge is crucial for implementing nuclear safeguards. It can be significant in identifying how the machines were utilized and whether any misuse was conducted by the operators. Moreover, the separation parameters can be used to conduct additional calculations in the cascade models. The model has the potential to serve as a beneficial tool for facility level non-proliferation applications as discussed later in Chapter 6. The new software has been verified using available open source 1-D results, and it shows great agreements with the previously published data. As part of the future work, the mass flow and isotopic diffusion codes can be combined into a single stream with improved user interface.

Chapter 5

Uncertainty Quantification of the Finite Element Methods for Multi-Component Isotope Separation

5.1 Overview

As demonstrated in the previous chapters, the complex fluid dynamics and isotopic diffusion inside a gas centrifuge rotor require numerical modeling tools due to the lack and expensive nature of experimental work on the field. While the finite element code in Chapter 4 has been verified for numerical accuracies through spatial grid independence study and rigorous convergence criteria, it is lacking a proper validation study because of the unavailability of experimental data. In order to ensure that the prediction regarding the separation of isotopes produced by the code is as accurate as possible, it is important to consider the uncertainty in the input data and quantify its effect on the output. In this chapter, the propagation of uncertainty associated with the physical centrifuge parameters as well as gas properties of uranium hexafluoride (UF_6) is investigated. The quantities of interest (QoIs) include the separative work (ΔU) and the overall separation factor (γ). The statistics of the problem response functions are evaluated according to the “Surrogate-Based Uncertainty Quantification.” The general approach of the study includes:

(1) The generation of response surface using Design of Experiment (DoE) to approximate the multi-component separation from the FE model and reduce computational efforts.

(2) The application of the UQ technique based on the Latin Hypercube Scaling (LHS) to the meta-model.

3) The introduction of Probability Density Functions (PDFs) for the input parameters to quantify their effects on the output machine performance.

The simulation of the DoE sample is conducted on the FE code while the development of the surrogate model and UQ analysis is completed using Matlab based UQLab framework developed at ETH Zurich [65]. Another software that was also considered was the Dakota Framework developed by Sandia National Lab written in C++ [66]. While both are well recognized and utilized in the scientific community, UQLab was selected for this work because of its ease of adaptability with Matlab. The numerical codes developed as part of this research are all written in Matlab and therefore, it required significantly less labor to integrate them to UQLab than Dakota. The analysis conducted here is the first of its kind on the field of isotope separation and highlights the practical use of uncertainty quantification techniques to build confidence in the results obtained using the new finite element model.

5.2 Background on UQ Methods

Since the 1960s, mathematical computing has had an exponential degree of impact on various scientific fields including nuclear physics. Computational results can affect the designs of actual systems, public policy, and the well-being of entire industries. Therefore, an important aspect of numerical simulations used to predict complex physical processes is ensuring their accuracy. The credibility of these developed models depends on the quality of physics modeling, verification and validation (V&V) approaches, sensitivity analyses (SA), and uncertainty quantification (UQ). The computational analyst is responsible for developing the conceptual model for the problem, formulating the mathematical model, selecting the numerical solution algorithms, programming the software to compute the numerical solution, and analyzing the results obtained from the simulation of the model. All of such tasks have been completed to formulate the multi-component diffusion model for this research effort. The primary issue that remains is the assessment of each step to ensure minimization of errors regarding the fidelity of physical detail embodied in the mathematical model representing the relevant physics that takes place in the gas centrifuge rotor.

Confidence regarding the obtained results from the model can be increased through the application of V&V methods. Verification allows for the assessment of software and numerical accuracy of the solution to the mathematical model while validation assesses the physical accuracy based on comparisons between computational results and experimental data. V&V are the leading practices for accessing and quantifying the accuracy of computational results in scientific computing. For the model defined in Chapter 4, verification has been completed by comparing different numerical methods used to solve the equations and by determining the optimal spatial discretization for the finite element method. However, validation has not been possible due to the complexity and lack of experimental data available in the open literature on the field of isotopic separation inside a gas centrifuge. Because of this obstacle, it is important to determine alternate ways to ensure the credibility of our model. One such way is to identify, characterize, and quantify external factors that could affect the accuracy of the computational results. This process is known as uncertainty quantification. There are various sources of uncertainty including the assumptions made in the mathematical model, the initial or the boundary conditions for the partial differential equations (PDEs), the input parameters required to solve those equations, and the numerical errors intrinsic to any such computational approach. The sources of uncertainty are propagated to uncertainties in the simulation results, in our case the separative capability of the gas centrifuge. Sensitivity analysis is the process of determining how the outputs depend on all of the factors that make up the model. UQ and SA play a significant role in establishing credibility by illuminating the analyst on how uncertain the obtained results are and what factors contribute the most to those results [67].

5.3 Motivation

The primary objective of the work in this chapter is to provide confidence in the modeling approach by utilizing UQ and SA methods, i.e., observing whether a small variation in input parameters will significantly affect the solution. The goal is to be able to use UQ methods to quantify the above effect and understand the role of individual parameters in the overall machine separative performance. Even though numerous authors in the past have studied isotopic diffusion inside a gas centrifuge and developed simplified models in the past as detailed in previous chapters, there are not any studies that have quantified the impact of uncertainties associated with machine as well as gas properties on the concentration distribution [48] [49] [52] [53] [54] [47] [68]. Understanding the effect of varying such input parameters on the model output will provide additional assurances on the validity of the new code. Furthermore, because of the sensitive nature of this area of nuclear research and lack of transparency especially in machine parameters, this work will allow to analyze centrifuge performance with certain confidence even when all of the input data may not be available. This is an additional positive contribution of the research to the field of nuclear non-proliferation and safeguards.

As discussed in Chapters 3 and 4, the performance of countercurrent gas centrifuges is evaluated by analyzing the equations of fluid dynamics and isotopic diffusion. The diffusion equation is decoupled from the fluid dynamic equations and reduced to a standard partial differential equation given by Equation(4.1). The multi-component isotopic gradients are determined as highlighted in Chapter 4, and the machine's separative capability is quantified by the overall separation factor. It is important to note that the overall separation factor utilizes the concentrations of the isotope of interest at the exit ports of the machine. While the calculations regarding the centrifuge's capacity to separate isotopes do not necessarily account for the concentrations in different parts of the rotor, they are the standard parameters used to calculate the isotopic gradients between the ends of the centrifuge. In practice, the product and waste are collected at the ends of the machine via extraction piping and the ^{235}U isotope concentrations at those end pipes indicate the level of separation achieved. For the same reasons, the overall separation factor is evaluated at the extraction points and serve as outputs in our diffusion model. Nevertheless, the developed model also has the unique feature of providing the map of isotopic spread in the entire separation region of the centrifuge rotor.

5.4 Independent Input Parameters

The solution of Equation (4.1) was derived in the previous chapter using FEM. Here, the goal is to verify the reliability of the numerical method used and conduct a parametric study to understand how each of the several key input parameters plays a role in the separative characteristics of the gas centrifuge and determine how sensitive the output is to minor variations in the input values. The independent parameters from which the uncertainty arises in the model for a fictitious Iguaçu centrifuge are identified below. The results obtained using the Rome machine are included in Appendix III. The mass flow of the feed gas as well as the diffusion of isotopes in the centrifuge volume are functions of each of these parameters. In the first iteration of the list of parameters, the gas viscosity and pressure at the wall were also considered. However, a $\pm$ 20% off of the nominal values for these parameters results in non-gaseous phase of UF_6. To mitigate such anomaly, gas viscosity and pressure are evaluated as functions of temperature rather than considered to be independent variables [69]. Therefore, any uncertainties in the machine performance can be largely attributed to the uncertainties associated with the terms in Table 5.1.

Table 5.1: Range of independent parameter values used for simulations of the Iguaçu centrifuge

Parameter	Description	Lower bound	Nominal	Upper bound
ω	Rotor speed (m/s)	480	600	720
T	Temperature at the wall (K)	270	300	350
θ	Machine cut-product flow rate/ feed flow rate (non-dim)	0.4	0.5	0.6
k	Thermal conductivity (W/(m*K))	5.435E-3	6.794E-3	8.135E-3
Sc	Schmidt number (non-dim)	0.64	0.8	0.96
F	Feed rate (mgU/s)	24	30	36
ΔT	Temperature gradient (K)	9.096	11.37	13.644
D_{scoop}	Drag force exerted by the scoop on rotating gas (Dynes)	560	700	840

The upper and lower bounds are determined by taking a ± 20% of the nominal value. The 20% range was chosen to confidently represent uncertainties in the measurements of UF_6 gas properties [15].The nominal data is taken from the original definitions determined when the fictitious Iguaçu centrifuge was created in 1996 [60]. As nuclear safeguards inspectors or analysts, the ideal values of these machine and gas properties used in particular facilities might not be available due to proprietary reasons. To account for such scenarios, a reasonable range of 20% deviation from anticipated values is considered to understand how the code deals with those variations in obtaining performance information.

From the data points in Table 5.1, the design of experiment was created by generating random samples from the design space. This was achieved using a Latin Hypercube Sampling (LHS) method on UQLab module in Matlab [65]. In LHS, the design space (with dimensions equal to the problem variables) is subdivided into an orthogonal grid with *N* elements per parameter. Within the grid, *N* sub-volumes are located so that along each row and column of the grid, only one sub-volume is chosen. Inside each sub-volume, a sample is chosen randomly. A total of 80 simulations, 10 times as many as the number of variables, were created using LHS to produce statistically significant data set. The simulations are shown in Table 5.2 below. Each case was simulated in the FE code to obtain the Iguaçu centrifuge uranium isotope separation data.

Table 5.2: Few of the 80 randomized simulations developed using LHS

Sim	$\boldsymbol{\omega}$	**T**	$\boldsymbol{\theta}$	**k**	**Sc**	**F**	**ΔT**	$\boldsymbol{D_{Scoop}}$
1	709.488	273.941	0.547	0.00791	0.949	32.458	11.904	795.271
2	675.252	272.000	0.594	0.00632	0.689	29.0404	10.274	589.409
3	608.173	326.489	0.445	0.00640	0.803	34.945	13.039	685.654
4	568.624	277.773	0.475	0.00729	0.841	25.197	10.415	750.555
5	629.709	285.260	0.434	0.00803	0.950	34.021	9.492	798.445
6	605.185	330.041	0.469	0.00803	0.654	34.239	13.596	590.008
7	645.266	291.822	0.469	0.00599	0.717	31.850	9.994	817.3001
8	634.376	342.664	0.529	0.00566	0.909	31.658	12.4902	613.983
9	483.428	334.437	0.434	0.00778	0.809	35.460	12.241	561.358
10	675.985	341.121	0.563	0.00615	0.719	27.323	10.285	750.866
:	:	:	:	:	:	:	:	:
80	486.353	339.377	0.595	0.00563	0.822	31.662	10.743	657.219

5.5 Metamodeling

Once the simulation results were obtained from the multi-isotope code, the output parameter, machine separation factor,γ is recorded for each case. Using this complete data set, a surrogate model of the multi-isotope code is developed in Matlab©.

Metamodeling (or surrogate modeling) decreases the total cost of stochastic modeling by making use of inexpensive surrogates in place of the costly computational models such as the finite element code. It approximates the capability of the code by fitting the data set to a high degree function. Polynomial Chaos Expansions (PCEs) provide a functional approximation of the computational model using spectral theorem on a robust basis of polynomial functions. To review, spectral theorem involves a diagonalization of a linear operator or matrix which can significantly simplify computations. An arbitrary square matrix A is diagonalizable if $P^{-1}AP = D$, where P is the matrix whose columns are the eigenvectors of A, and D is a diagonal matrix.

As a mathematical illustration, take a random vector with independent components $\boldsymbol{X} \in \mathbb{R}^M$ described by the joint probability density function (pdf) $f_{\boldsymbol{X}}$. Then, consider a finite variance computational model as a map $Y = M(\boldsymbol{X})$, with $Y \in \mathbb{R}$. The polynomial chaos expansion of $M(X)$ is defined as:

$$Y = M(\boldsymbol{X}) = \sum_{\alpha \in \mathbb{R}^M} y_\alpha \psi_\alpha(\boldsymbol{X}) \tag{5.1}$$

where $\psi_\alpha(X)$ are multivariate polynomials orthonormal with respect to f_X, $\alpha \in \mathbb{N}^M$ is a multi-index that identifies the components of the multivariate polynomials ψ_α and $y_\alpha \in \mathbb{R}$ are the corresponding coefficients. The detailed definitions and the methodology utilized to construct the polynomial basis are obtained from the UQLab User Manual on PCEs [70].

5.6 Sensitivity Analysis

The variability of each input variable or their combinations given by $\boldsymbol{X}$ and its effect on the variability of the response, $y = M(X)$ of the mathematical model defined above in Equation (5.1) can be described using sensitivity analysis. SA is also useful in identifying unimportant input variables and consequently reducing the dimension of the problem. This analysis is performed solely based on the model response evaluations for a sample of inputs, obtained in ways to maximize the output information about the model structure. There are various means available to conduct SA. Some examples include correlation-based methods that analyze the correlation of samples of the inputs with samples of the output, linearization methods at given point, or derivative-based methods that look at the values of partial derivatives of the model. For this study, global sensitivity analysis based on variance decomposition techniques is considered. This approach considers the entirety of the input domain rather than a subset or smaller sample of the inputs.

Sobol' sensitivity indices are calculated to understand the relative effect of each of the input variables and the interaction between them on the predicted separation capability of the gas centrifuge, the model output. Sobol' indices describe the total variance of the model in terms of the sum of the variances of the summands [71]. This method is also referred to as Analysis of Variance (ANOVA). The first and higher-order indices are defined as:

$$S_{i_1 \dots i_s} = \frac{D_{i_1 \dots i_s}}{D}, \tag{5.2}$$

Which represent the relative contribution of each group of variables $\{X_{i_1} \dots . X_{i_s}\}$ to the total variance. $D_{i_1 \dots i_s}$ are the partial variances and D is the total variance of the decomposition given by $f(\boldsymbol{X})$. The details of Sobol' decomposition and the derivations of equations for indices are provided in the UQLab user manual for sensitivity analysis [72]. X_i is a single input variable and the index representing this term is known as the first-order Sobol' index. The interaction indices that consider the effects of the interactions of the variables X_i and X_j are referred to as higher-order Sobol' indices denoted by $S_{i,j}, i \neq j$. The total Sobol' index of input variable X_i, denoted by S_i^T, is the sum of all of the Sobol' indices involving the variable:

$$S_i^T = \sum_{\{i_1 \dots i_s\} \cup i} S_{i_1 \dots . i_s} \tag{5.3}$$

The definition given by Equation (5.3) requires computing each index separately and is computationally inefficient. Instead, the sensitivity measure of all the variables excluding X_i can be prescribed by $S_{\sim i} = S_v$, where $v = \{1, \dots i-1, i+1, \dots M\}$. Then the total index is:

$$S_i^T = 1 - S_{\sim i} \tag{5.4}$$

Sobol' indices are normally calculated by Monte Carlo (MC) simulation making them inefficient to use with computationally demanding models like the one in discussion, which currently takes on the order of 20-30 minutes per simulation case. To address this issue, Sudret (2008) developed a post-processing of polynomial chaos expansions (PCE) for sensitivity analysis [73]. In addition, the Sobol' indices can also be computed by post-processing the coefficients of a canonical low-rank approximation (LRA) metamodel [74]. All three methods are implemented in the Matlab program to cross-reference the output of the surrogate model and compare and contrast the solutions as a verification technique.

Figure 5.1 presents the sensitivity indices calculated using Equation (5.4) for each of the independent input parameters from Table 5.1. Three different calculation techniques are used including the MC, PCE, and LRA that agree within 5% of each other. Parameter 1, the rotor speed, and parameter 3, the cut of the machine are the most influential variables followed by parameter 5, Schmidt number and parameter 6, feed rate. Parameters 4, thermal conductivity has the least effect on the output while parameter 2, the gas temperature at the rotor wall, and the countercurrent flow parameters that drive the axial mass flux including end-to-end temperature gradient and scoop drag force given by parameters 7 and 8 respectively have roughly the same effect on the overall separation factor. The first order indices as well as the second order interaction terms used to calculate the total Sobol' index are presented below determined using just the PCE metamodel. Both total order indices in Figure 5.1 and first-order sensitivity indices in Figure 5.2 have similar values, which indicate no significant second-order interaction between the parameters. We can see that the cut of the machine is the most important term contributing to approximately 36% of the model output variability. The cut also interacts with five other parameters as shown by the second order plot below; however, such interaction has minimal influence on the changes in the output as indicated by significantly smaller values of the second-order indices. Physically, the interaction can be anticipated. To recap, cut describes the percentage of feed flow that exits out of the product end. Thus, increasing or decreasing the cut can affect how the gas is distributed inside the centrifuge rotor, which in turn can determine the counter-current flow and the overall separation capability of the machine.

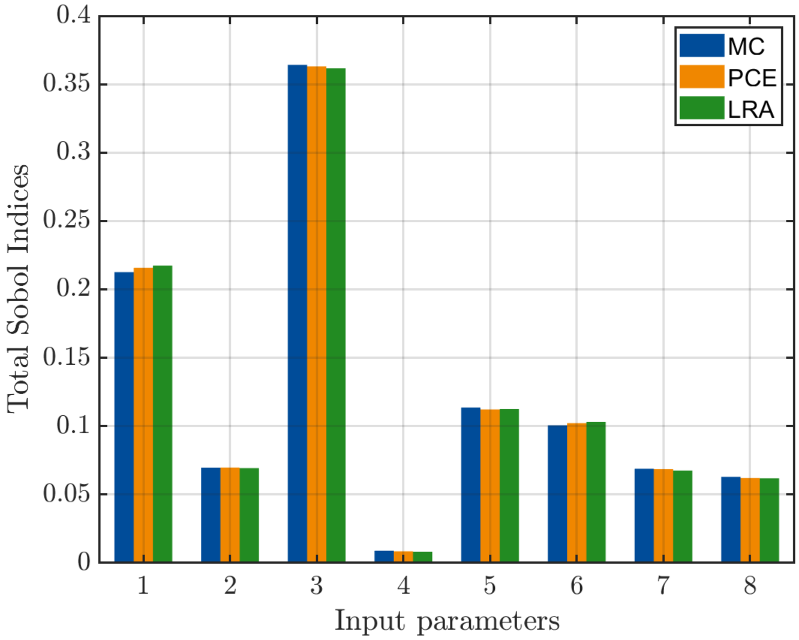

Figure 5.1 Total Sobol' sensitivity indices for the eight different input parameters. The parameters are listed numerically in the order they appear in Table 5.1.

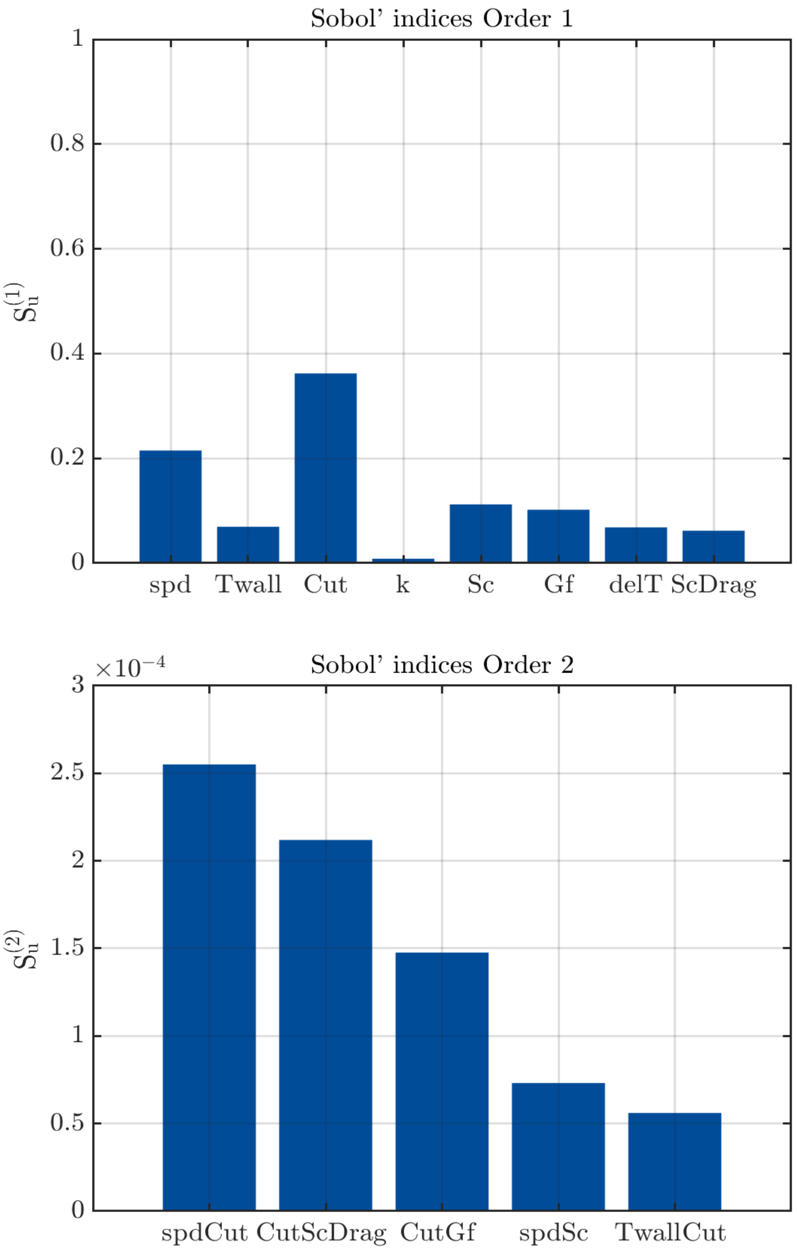

Figure 5.2: First order indices (top) and the second order indices (bottom) for the different input parameters that make up the total indices in Figure 5.1

5.7 Uncertainty Quantification

The UQ analysis was carried out for the eight variable parameters listed on Table 5.1. The Quantity of Interest (QoI) was the overall separation factor,γ defined in Equation(4.2). The separation factor was selected for this analysis rather than the separative work since the separation factor only depends on the concentrations of the key isotope while the separative work is a function of the flow rates in addition to the concentrations. The flow rates are treated as independent parameters using feed rate and cut parameters defined above. The DoE for the QoI based on LHS method was performed in the UQLab Matlab script for the variable ranges also defined on Table 5.1. The meta-model developed using PCE is then used to simulate 500 samples generated using LHS method. The meta-model reliability is ensured through a cross-validation analysis that is automatically performed by UQLab using the leave-one-out cross-validation error (ϵ_{LOO}) [70]. A uniform distribution of the input variables for the defined ranges were considered as the input probability density function (pdf). In this case, any parameter value within the established range has the same probability of appearing in the DoE. The prior distribution of the sample is presented below.

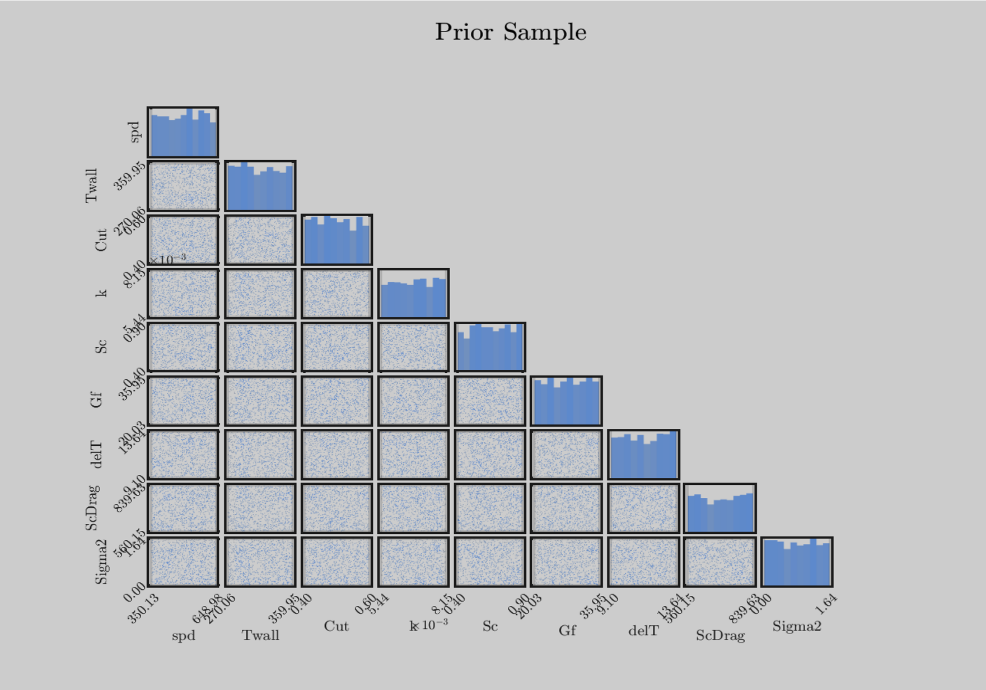

Figure 5.3: Initial uniform distribution of the input parameters along with the overall variance and the range of values for each.

Result of the uncertainty propagation through the surrogate model is the discretized pdf for the output function,γ shown in Figure 5.4.

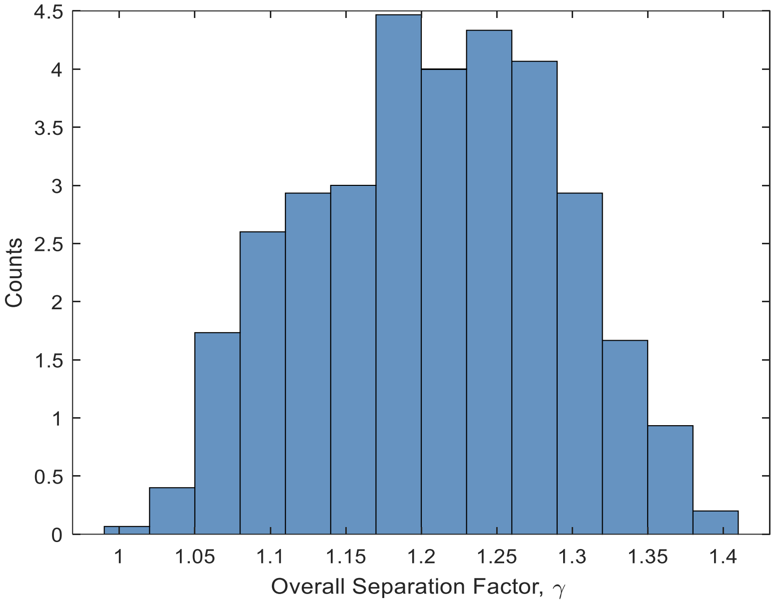

Figure 5.4: Histogram of the pdf for the output function γ

Table 5.3: Statistical moments for the response function distributions

Statistical Moments	**Values**
Mean	1.2079
Standard deviation	0.08101
Kurtosis	2.2689
Skewness	-0.06258

The pdf of the QoI does not quite represent the uniform distribution of the input variables. This suggests that the isotopic separation obtained by a particular centrifuge is constricted around a particular value even for a large variation of the input variables. In our case, the $\pm$ 20% variations in the eight input parameters caused a roughly $\pm$ 15% variation in the overall separation factor from a mean value of 1.208. The distribution in Figure 5.4 for γ is sharper (positive kurtosis) and slightly shifted to the right (negative skewness) with respect to a Gaussian pdf. To ensure that the number of samples tested is not affecting the distribution of the output, an additional case with 5000 samples, an order of magnitude greater than the previous case is also analyzed. The histograms obtained for the QoI using these two sample sets are presented in Figure 5.5 along with the statistical data in Table 5.3. The differences between the two distributions are minimal and 500 samples can be deemed sufficient.

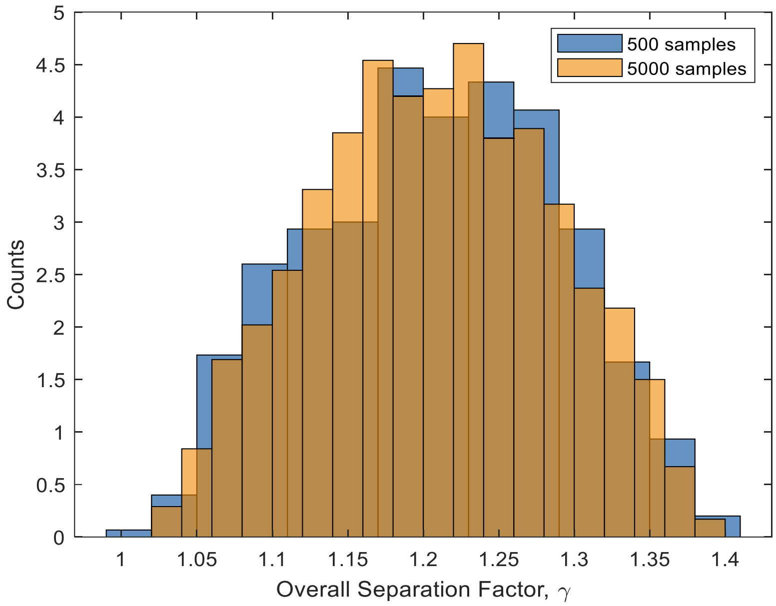

Figure 5.5: Comparison between 500 and 5000 samples for the LHS based UQ analysis for the overall separation factor

Table 5.4: Statistical moments for the case with 5000 samples. The minimal differences between this set and the one on Table 5.3 *suggests that 500 samples are sufficient for UQ calculations.*

Statistical Moments	**Values**
Mean	1.2079
Standard deviation	0.07884
Kurtosis	2.2809
Skewness	-0.008777

An additional case was analyzed by assigning a normal distribution of the input pdf with the mean of the parameters set at the nominal value defined on Table 5.1. The standard deviation, σ was calculated to have a small perturbation of the input parameters at 1% of the mean value. This small value of the standard deviation translates to approximately ±3% uniform range off of the mean value for the key parameters identified by the sensitivity analysis. The 1% was therefore deemed to be a reasonable anticipation of the minor fluctuations in the input parameters. The resulting pdfs of all of the input variables are shown below in Figure 5.6 with the range of values included in the design space. A more detailed view of the distributions for the most significant parameters, the machine cut and the rotor speed, are given in Figure 5.7.

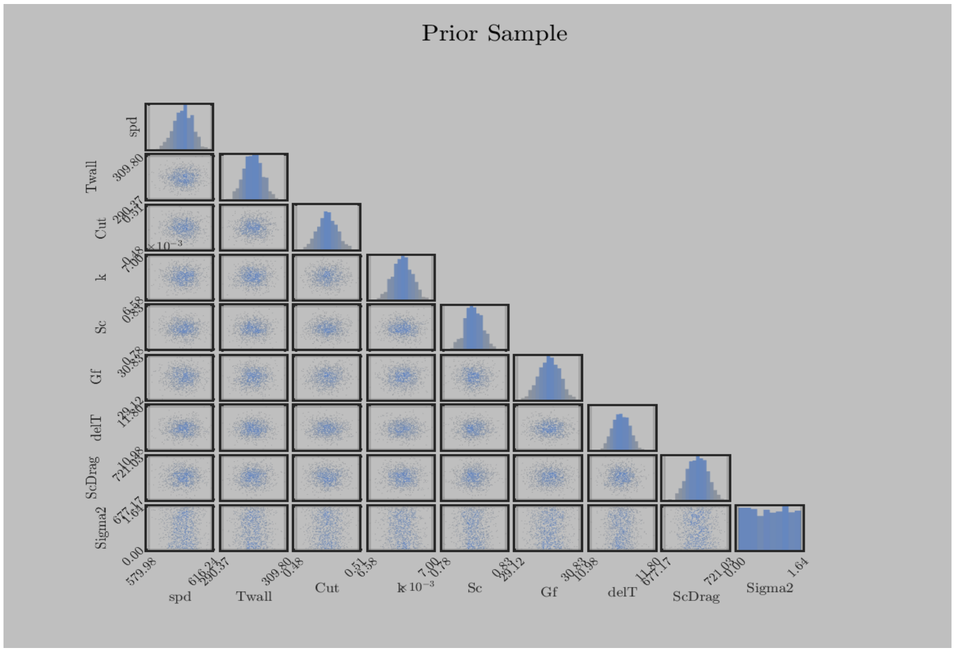

Figure 5.6: Normal input distributions with standard deviation calculated as 1% of the mean value

(a)

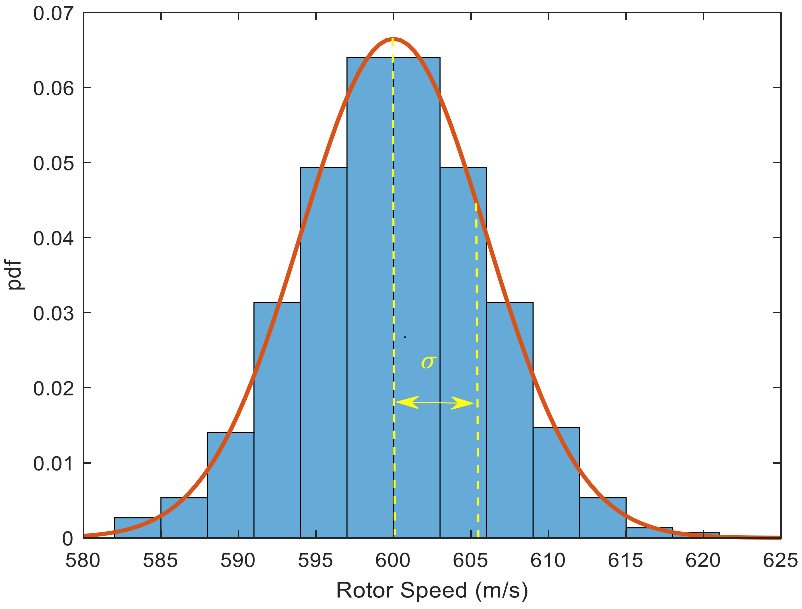

(b)

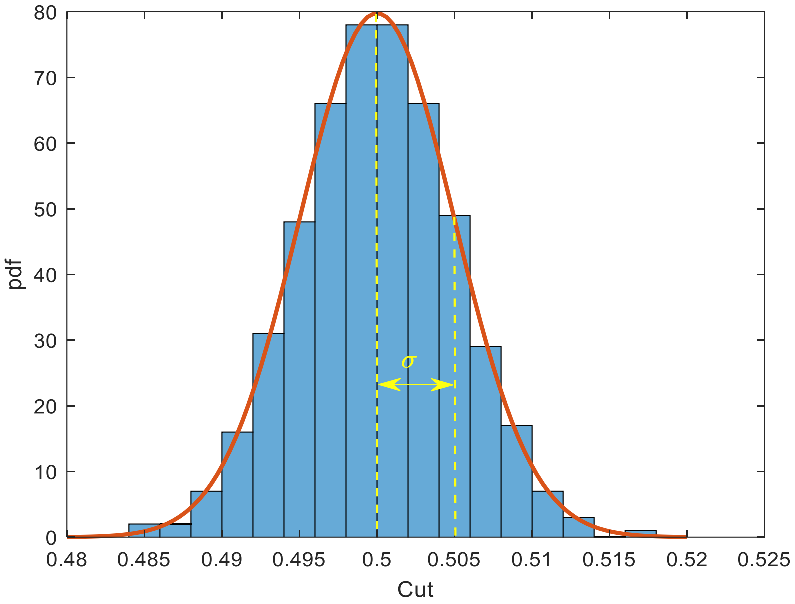

Figure 5.7: Normal distribution of two of the most significant input parameters, rotor speed (a) and cut (b), with standard deviation at 1% of the mean

The uncertainty propagation is performed again using the LHS method for 500 samples and the distribution for the overall separation factor is reported in Figure 5.8. It is evident that the output pdf is similar to the input normal distribution. Table 5.5 summarizes the statistical moments calculated for this case. The red curve in Figure 5.8 represents the continuous Gaussian distribution associated with the mean and standard deviation from Table 5.5 fitted to compare with the discretized histogram. Compared to the normal pdf in red, the overall separation factor distribution is sharper (positive kurtosis) and slightly shifted to the right (negative skewness). The results once again suggest that the values of the separation factor are constrained to a narrow range. A small variation in the input parameters does not have a significant effect on the output. It can be seen that 99% of the 500 samples (or 3 standard deviations) that were simulated by the surrogate model, produced values within 1% of the mean for the separation factor. This consequently indicates that the machine performance determined by the models is not sensitive to minor fluctuations in the input data adding additional layer of confidence in the code.

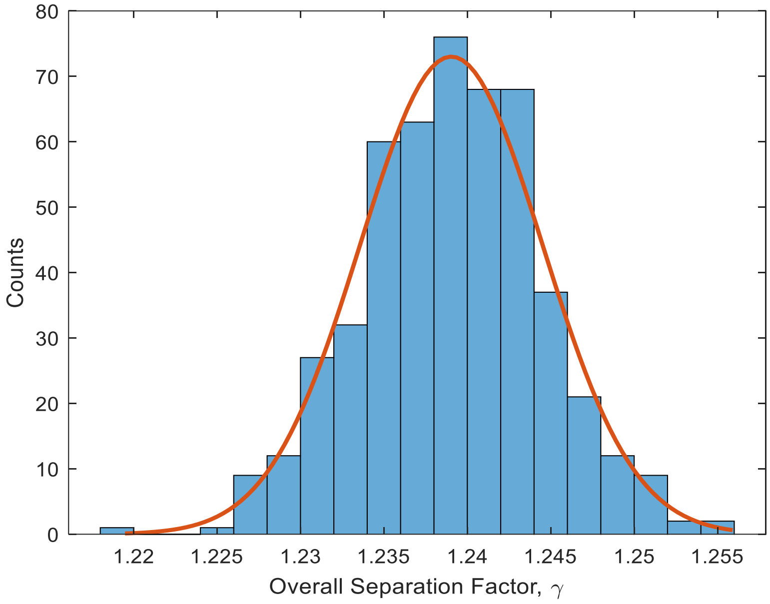

Figure 5.8: Probability distribution of the overall separation factor

Table 5.5: Statistical moments for the output function distribution

Statistical Moments	**Values**
Mean	1.2391
Standard deviation	0.005464
Kurtosis	3.0922
Skewness	-0.02074

5.8 Summary and Conclusions

The quantitative analysis of the variation of the eight different input parameters on the gas centrifuge model performance is evaluated. The randomized sample set of the inputs are obtained using LHS method on Matlab's UQLab module. This sample set was simulated in the finite element model to obtain the output data on the Iguaçu gas centrifuge performance. Subsequently, the simulation results were used to develop a surrogate model of the FEM diffusion code and further variations of input parameters were conducted to study the propagation of such variations on the output. From the sensitivity analysis, it can be seen that out of the eight parameters, the most significant ones include the speed of centrifuge rotation and the cut of the machine. This is consistent with what is expected from the theoretical perspective of the physics inside the centrifuge rotor. As expected, increasing, or decreasing the rotor speed in turn can increase or decrease the separation ability of the centrifuge. The cut needs to be optimized to obtain ideal separation. Thus, a great variation of the cut values from such optimal point can severely impact the desired output.

From the UQ analysis, it is evident that the 20% variations on all of the input parameters only causes the separation factor to deviate by about 15% from a mean value. The ability to quantify the fluctuations on the separative performance of the centrifuge provides greater confidence on the accuracy of the results obtained from the new code. Since the uncertainty in the input samples propagates roughly linearly on to the output, the robustness of the developed model can be inferred. In addition to the high fidelity of the new model, this work can also be applied to the application of non-proliferation. For example, in a potential proliferation scenario, if the nuclear inspectors are unable to obtain exact parameters of the centrifuges used by a rogue party, using variations in the anticipated values, we can determine such party’s capability with a quantifiable uncertainty. Such information can be crucial in understanding the severity of problems that the inspectors and the IAEA may be dealing with in general. Thus, by developing the methodology to ascertain the output of the multi-isotope model through uncertainty analysis, an additional layer of validity in the new code has been added that can be applied directly to nuclear non-proliferation.

Chapter 6

Applications of the Numerical Models on Safeguarding GCEPs

6.1 Overview

In this chapter, the models discussed in Chapters 3 and 4 are used to perform an enrichment cascade analysis with the goal of supporting the International Atomic Energy Agency's (IAEA) nuclear safeguards obligations. The IAEA inspectors routinely carry out environmental sampling (ES) as a verification method. Collection of environmental swipe samples at various locations in Gas Centrifuge Enrichment Plants (GCEPs) is an important process in detecting misuse of a declared facility and possibly the existence of undeclared nuclear material. These samples are measured for isotopic composition in uranium containing particles by Thermal Ionization Mass Spectrometry (TIMS) or Inductively Coupled Plasma Mass Spectrometry (ICP-MS). Even though ES is highly effective in detecting the absolute value of enrichments and their deviations from the declared values, it cannot explain the cause of those changes. Several potential explanations can serve as possibilities for particles detected above or other than the declared enrichment. These include normal and non-malicious events such as the design of the enrichment cascades, unintentional failures of the machines, or deliberate misuse by the facility operators such as addition of undeclared feed. The primary objective in this chapter is to understand how these factors affect the enrichments produced by a cascade and quantify anticipated multi-isotopic concentrations for each case. The following methodology is employed to determine signatures at a particular facility.

1) Utilize a new two-dimensional multi-component diffusion code to obtain centrifuge performance data and use that information to design and perform cascade analysis. Compare and contrast the results with previous 1-D radially averaged solutions from the *Pancake* code.
2) Design a high-assay low-enriched uranium (HALEU) fuel cascade with the production goal of 19.75% ^{235}U for each set of machine data above. Investigate two cascade scenarios that include enrichment of natural uranium (NU) feed to 19.75% ^{235}U in a single cascade compared to a two-step process of NU to 5% and then 5% to 19.75%.
3) Simulate the intentional vs. unintentional off-normal scenarios in the cascades to assess the differences in isotopic concentrations.

A non-ideal squared-off cascade model previously developed at the University of Virginia is used to calculate flow rates and isotopic concentrations of the process gas. The analysis is performed using the fictitious Rome and Iguaçu machines operated at 600 m/s rotor speed. The upper and lower bounds of normal and abnormal enrichments in a typical facility are used in conjunction with ES results to understand the root causes of such observations.

6.2 Safeguards and Environmental Sampling

According to the IAEA, a total of 175 States have concluded the Comprehensive Safeguards Agreement (CSA) as of June 2020. The CSA is required for all non-nuclear weapons states signatories to the Treaty on the Non-Proliferation of Nuclear Weapons (NPT) and is voluntary for non-NPT members. The agreement requires that the state declare the type and quantity of nuclear material subject to safeguards. The IAEA then independently verifies that a state's declaration is accurate and complete and that the materials and facilities are used exclusively for peaceful purposes. The international agency utilizes several techniques and measures to fulfill its verification duties such as [75]:

1) On-site inspections by IAEA inspectors including random and unannounced visits
2) Accountancy of nuclear material through review of facilities' records and documentation
3) Surveillance, containment, and monitoring using cameras, seals, flow meters, and radiation detectors
4) Verification by Destructive Analysis (DA) and Non Destructive Analysis (NDA) of nuclear material inventories and flows
5) Collection and analysis of environmental and nuclear material samples

Environmental sampling is an important safeguards tool that makes use of small particles containing nuclear material released during operation. The IAEA has adapted the environmental sampling measures since 1996 as an additional measure of detecting undeclared nuclear materials or enrichment activities in States under safeguards agreements [76]. At GCEPs, ES is used to ensure that no uranium is enriched above the declared levels. Samples are collected by the IAEA inspectors on site by running cotton cloth swipes on various surfaces collecting the particles. The swipe samples are taken in locations where access is guaranteed by the facilities' safeguards agreements with IAEA. Some of the potential areas that can contain higher traces of activities include breakable cascade connections such as feed and withdrawal points, surfaces in the vicinity of sampling locations, and surfaces of tools and equipment used to transport material in and out of the facility [77]. The collected samples are then sent to the Safeguards Analytical Laboratory (SAL) or one of the Network Analytical Laboratories (NWAL) for content analysis using TIMS or ICP-MS [78]. The analytical procedure involves either the particle analysis and/ or bulk analysis. The former, which is performed regularly, can detect individual particles of uranium and plutonium, and examine their isotopic signatures and elemental composition. The information on the ratios of isotopic abundances in the particles, including those of minor uranium isotopes, can indicate the type of enrichment process carried out at the facility under inspection. In some instances, individual facilities can be identified based on particle signatures. Bulk analysis produces an extensive overview of the swipe content and extraction of information about the sample as a whole. According to the IAEA, roughly 400 environmental samples are analyzed every year and thus it is a vital tool used to fulfill its verification duties [79].

While the swipe samples can assist in the detection of anomalous enrichments, they cannot precisely indicate the type of activity that might have occurred [80]. It is important to distinguish if the abnormality detected is due to intentional misuse by the facility operators or due to unexpected issues such as piping or machine failures. In addition to environmental sampling, the IAEA makes use of other safeguard measures listed above that are agreed upon with the State or specifically with the facility. However, a proliferator can still bypass such measures and pursue illicit activities. Therefore, if the environmental samples indicate anomalies, there needs measures in place to understand how they originated and whether to pursue further investigations. One such way is through numerical modeling of typical enrichment facilities and recognizing the trends in isotopic signatures for various potential proliferation scenarios. This knowledge can help interpret the swipe data and allow the IAEA to take the required actions in a timely manner.

There are studies in literature that have looked at the modeling for enrichment cascades to quantify isotopic ratios. Fischer et. al investigated the variations in the minor uranium isotopic concentrations, (isotopes other than ^{235}U and ^{238}U), for two different cascade arrangements [81]. The motivation behind such study was that the IAEA's environmental samples showed that highly enriched uranium (HEU) produced by different countries and facilities can have different minor isotope concentrations. The study used an ideal cascade model, the *MSTAR* code, to perform the analysis [82]. *MSTAR* is widely used in safeguards applications because it does not include sensitive parameters about the centrifuge or the cascade designs. However, this implies that several simplifying assumptions of the facility were made in the study and the uncertainty associated with such assumptions need to be quantified. Migliorini et al. developed non-ideal cascade models to perform potential proliferation scenarios for fictitious centrifuges [83] [84] . Their study, however, involves the use of simplified 1-D model to obtain centrifuge performance and the cascade designs are limited to the enrichment of natural uranium to 5 % ^{235}U.

In the past few years, there has been a growing interest, especially in the US, in the production of high-assay low-enriched uranium (HALEU). Such fuel is enriched to between 5% and 20% ^{235}U and will be required to operate many advanced reactor designs that are currently under development. U.S. based Centrus Energy Corp is leading the enrichment efforts at its facility in Piketon, Ohio after the Nuclear Regulatory Commission (NRC) approved its operational license in June 2021 [85]. Even though this type of enrichment activity can pose a proliferation danger, since enriching ^{235}U from 5% to 20% and higher takes less effort compared to enriching natural uranium to 5% ^{235}U, there is not any open-source literature studying the safeguards implications of consistently producing such higher enrichment. The effort required to separate the heavier and lighter uranium isotopes is defined by a unit known as the separative work unit (SWU). SWU is measured in units of kilograms. The fact that higher SWU is required to enrich NU to 5% can be explained using second law of thermodynamics that states that an isolated system produces an increase in entropy. However, separation of isotopes represents greater order or lower entropy than a mixture of isotopes, requiring increasing effort to counter entropy. Another terminology often utilized to comprehend separative work is the value of an enriched gas, which closely follows the concept of entropy [86]. The performance of an enrichment technology is evaluated by calculating the net value added to a certain amount of material passing through the machine. The value function given by Equation (6.5) is highest for a value of 0 and 1. In other words, a mixture with one dominant isotope has the highest value. It decreases with increasing concentration up to 50% ^{235}U because the isotopic mixture is getting farther away from being dominated by a single component. At 50%, the value is zero since the mixture is farthest away from an isotopically pure entity. Therefore, the value is greatest at lower enrichments between NU and 5% compared to 5% and 20%, illustrating lower SWUs for the latter. The study here is performed for the upper enrichment limit of 19.75% in order to ensure that it still falls under the low enriched uranium designation with expected manufacturing deviations. The US designates the 20% ^{235}U and higher as HEU and a great proliferation concern.

The primary objective of this work, therefore, is to analyze a cascade arranged to produce product streams of up to 20% for potential normal and off-normal operations. The analysis differs from previous studies since the newly developed 2-D multicomponent isotopic diffusion model, *MultiPort*, is used to first evaluate centrifuge performance data rather than the 1-D *Pancake* model. The higher fidelity code is compared against the latter to highlight any uncertainty associated in the calculations. Then such a cascade is designed using fictitious Rome centrifuge to study two different enrichment scenarios. In the first case, commercial natural uranium is enriched from 0.72% ^{235}U directly to 19.75 % ^{235}U while in the second scenario, it is achieved in two steps: 0.72% to 5% and 5% to 19.75%. The minor isotopic distributions for the two scenarios will be analyzed to quantify any differences. Finally, two off-normal operational scenarios are presented for the second cascade structure. These include unintentional centrifuge failure in the feed stage and intentional addition of undeclared feed to the up-flow of the top stripping stage. Thus, the isotopic ratios for the premeditated misuse are measured against accidental mishap for both the 5% ^{235}U product concentration and the 19.75% fuel.

6.3 Machine Performance

A detailed cascade analysis requires information regarding the performance of individual machines in operation. Centrifuge performance maps provide its separative capability at different gas feed rates and cuts. The cut (θ) is the ratio of the centrifuge product rate to the feed rate. The ability of gas centrifuges to separate the isotopes of uranium are characterized by two parameters, the separation factor and the separative power. The overall separation factor measures the relative enrichment of individual isotopes across the centrifuge and is defined as

$$\gamma_i = \gamma_0^{238-M_i} \tag{6.1}$$

where M_i is the mass number of isotope i and γ_0 is the unity overall separation factor that is determined from the binary overall separation factor, γ, between ^{235}U and ^{238}U.

$$\gamma_0 = \gamma^{(238-235)^{-1}} = \gamma^{\frac{1}{3}} \tag{6.2}$$

$$\gamma = \frac{N_{235}^{P}}{N_{238}^{P}} / \left(\frac{N_{235}^{W}}{N_{238}^{W}}\right) \tag{6.3}$$

Equation (6.1) is used in the separative performance maps where N^P and N^W are the concentrations at the product and waste streams respectively. The separative power, ΔU is the amount of useful work done by the centrifuge per unit time and defined as

$$\Delta U = PV(N_P) + WV(N_W) - FV(N_F) \tag{6.4}$$

Where $P, W,$ and F are the flow rates at the product, tails, and feed ports respectively and V is the value function given as

$$V(N) = (2 * N - 1) * ln(N/1 - N) \tag{6.5}$$

The value function evaluates the value of a given concentration and the separative power provides the amount of separation achieved per time usually given in kgU/yr, also known as SWU. The concentrations in Equation (6.4) are for the ^{235}U isotope for this work.

The study was conducted first using the fictitious Rome centrifuge followed by Iguacu. The geometric and operating details of the centrifuges are the same as given in Table 3.1. Two different performance maps are developed first using *Pancake* code [47] and again using the new *MultiPort* diffusion code [61]. The *Pancake* solution solves the concentration gradient equations using the radially averaged technique where the radial variation of the isotopes is averaged at each axial point along the length of the centrifuge. *MultiPort*, on the other hand, calculates both the axial and radial distributions. The concentrations in Equations (6.3) and (6.4) are obtained at the location of the extraction ports rather than averaged across the top and the bottom surface. The general procedure for obtaining performance maps involves first determining the optimized operating point by varying the countercurrent flow drives including the feed rate, cut, wall temperature gradient, and scoop drag force until the separative power is maximized. Next, the temperature gradient, scoop drag, and machine cut are fixed and the separative parameters are calculated over a range of centrifuge feed rates.

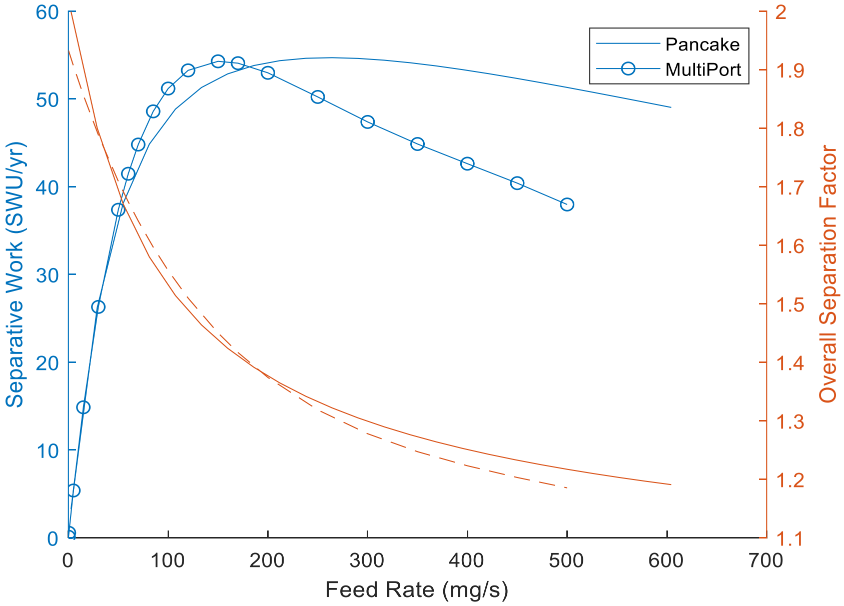

Figure 6.1: 1D performance maps for the Rome centrifuge. The separation parameters are plotted over a range of feed rates. The optimal feed rate is the value associated with maximum separative power.

The performance maps for the Rome machine are presented in Figure 6.1. The x-axis shows the range of centrifuge feed rates given in mgUF$_6$/s. The left y-axis shows separative work per year while the right y-axis shows the overall separation factor given by Equation (6.3). The results from both *Pancake* and *MultiPort* are presented in the same plot for comparison. The solid lines represent the results from the *Pancake* code. As seen in Figure 6.1, the performance obtained from both codes follow the same general trend. The separation factor maximizes as the centrifuge feed rate goes to zero and diminishes as the feed rate increases. The separative power is at zero for feed rate of zero but rises rapidly to a maximum value as more feed is added and begins to decrease for higher feed rate values. The feed rate corresponding to the maximum value of separative power is the optimal operating point. From the *Pancake* plot, this point is at the feed rate value of 207 mgUF$_6$/s while for *MultiPort*, the optimal feed rate is 150 mgUF$_6$/s, which amounts to 31.93% difference between the two solutions. However, the maximum separative power values are 55.133 SWU/yr and 54.271 SWU/yr for *Pancake* and *MultiPort* respectively, a 1.58% difference. Likewise, the optimal values of the overall separation factor are 1.373 for *Pancake* and 1.450 for *MultiPort,* which corresponds to 5.48% difference. The separation factor plots from both solutions are within approximately 5% of each other for the entire range considered. Both solutions show excellent agreement at smaller feed rate values up to the optimal point. At higher feed rates, the quantity of gas in the centrifuge is increasing faster than its capability to separate the isotopes. This inefficiency can lead to greater radial fluctuations of concentrations and thus would explain the greater differences between the radially averaged and two-dimensional diffusion equations.

6.4 Cascade Designs

The ideal operating parameters from Figure 6.1 are used to design enrichment cascades and create facility level simulations. Previously developed squared-off cascade model is used to design the cascade. The general cascade theory has been analyzed extensively in literature including by Cohen [87], Hoglund et. al [88], Brigoli [89] , and Von Halle [90] [56]. The most recent work by Migliorini serves as a reference to the cascade code *DesignCascMult* that is used here to design squared-off cascade based on target enrichment parameters [57]. *DesignCascMult* takes in the performance data of the centrifuge as defined above, cascade feed enrichments for the isotopic mixtures in molecular fractions, cascade feed rate, and target product and tails concentrations for the ^{235}U isotope. Based on those inputs, the ideal cascade equations are solved to determine the number of stages, machines, and flow rates. In an ideal cascade, the heads separation factor and the tails separation factor for a given stage *n* are assumed to be equal.

Additionally, the upflow and downflow concentrations at a particular stage are assumed to be the same as the feed concentrations of the stage above and below it i.e., no mixing effects.

$$\alpha_n = \beta_n = \sqrt{\gamma_n} = \alpha_0 = \beta_0 = \sqrt{\gamma_0} \tag{6.6}$$

$$N_n = N'_{n-1} = N''_{n+1} \tag{6.7}$$

Applying the above assumptions, the number of stages in the enriching and stripping sections of the cascades can be evaluated for the target enrichments as follows

$$n_E = \ln\left(\frac{R(N_P)}{R(N_F)}\right) * \left(\frac{1}{\ln(\alpha_0)}\right) + 1 \tag{6.8}$$

$$n_s = \ln\left(\frac{R(N_F)}{R(N_W)}\right) * \left(\frac{1}{\ln(\alpha_0)}\right), \tag{6.9}$$

where R is the abundance ratio given by $R(N) = \frac{N_{235}}{N_{238}}$. The feed concentration gradient in the n^{th} stage of the enriching and stripping sections of the cascade is found by

$$C_{E,n} = \frac{R(N_F)\alpha_0^{n-1}}{1 + R(N_F)\alpha_0^{n-1}} \tag{6.10}$$

$$C_{S,n} = \frac{R(N_F)\alpha_0^{n-n_s-1}}{1 + R(N_F)\alpha_0^{n-n_s-1}} \tag{6.11}$$

The cut value of the entire cascade can be obtained as

$$\theta = \frac{N_F - N_W}{N_P - N_W}, \tag{6.12}$$

where $N_F, N_W, and\ N_P$ are cascade feed and target tails and product concentrations of the ^{235}U isotope respectively. Using the cut and defined feed rate, the cascade product flow rate can be calculated. Thus, the stage feed rates for the enriching and stripping sections are evaluated as

$$G_{E,n} = P * \frac{\alpha_0 + 1}{\alpha_0 - 1} * \frac{N_P - N_{E,n}}{N_{E,n} * \left(1 - N_{E,n}\right)} \tag{6.13}$$

$$G_{S,n} = W * \frac{\alpha_0 + 1}{\alpha_0 - 1} * \frac{N_{S,n} - N_W}{N_{S,n} * \left(1 - N_{S,n}\right)} \tag{6.14}$$

The tails rate, W comes from the overall cascade flow balance given by $F = P + W$.

Finally, the number of centrifuges in each stage can be found by

$$M_n = \frac{G_n}{G_0} \tag{6.15}$$

In Equation(6.15), G_n is the feed rate going into stage *n* and G_0 is the optimal centrifuge feed rate determined from the performance map. The stage numbers given by Equations (6.8) and (6.9) and the total machines in each stage given by Equation (6.15) are the most optimal non-integer values. Since there cannot be fractional stages or machines, those values are "squared-off" by rounding to the nearest integers. This changes the stage flow rates and consequently the concentrations deviating the cascade behavior from ideal to non-ideal but practical operation. The gradient equations in the cascade are solved using *PCFX4* code written originally by Von Halle [91] and modified and transported to Matlab© by Migliorini [92].

6.5 Transient Cascade Study

The uranium fuel with ^{235}U enriched between 5 to 20% is considered advantageous for both existing and next generation advanced reactors. With the rising interests in enriching uranium past its common 5% fuel, it is important to discern the potential proliferation concerns it possesses. Thus, a few different case studies are explored to obtain uranium isotopic gradients in a normally operating HALEU cascade as well as one with intentional and unintentional misuse. These cases are defined below.

1) The cascade is designed in two scenarios that involve enriching natural uranium (NU) to 19.75% ^{235}U at the product end.
    a. A single cascade that enriches NU to 19.75%
    b. Two separate cascades, one enriching NU to 5% and second enriching the 5% to 19.75%
2) Transient cascade code is utilized to study off-normal operations
    a. Unintentional centrifuge failure in the feed stage of the cascade
    b. Intentional addition of material in the top stripping stage up-flow

Case 1 mirrors the study by Fischer et al [93] where they used an ideal *MSTAR* cascade model to show that environmental signatures of HEU produced from a single cascade can be differentiated from uranium produced from series of four cascade. Here, the goal is to modify that study to highlight differences in such signatures obtained for HALEU using non-ideal *DesignCascMult* model described above in a single vs. two cascades. The findings can quantify the differences in isotopics between the two scenarios, which can then be used to insinuate the type of facility setup and verify whether that aligns with the facility declarations.

The transient study in case 2 is performed based on the methodology developed by Migliorini et. al [57]. An enrichment facility is designed to operate for 50 hours. After the first hour of operation, either an intentional or accidental off normal behavior occurs over a fifteen-minute period. This behavior lasts for 26 hours, after which it is brought back to normal operation over another fifteen-minute period. The *TransCasc* code developed by Migliorini solves the transient cascade multi-isotope separation equations for time-varying flow rates, number of centrifuges, and side streams. The physical centrifuge parameters, isotopic composition of the feed gas, and the cascade details obtained from *DesignCascMult* including the number of stages, centrifuges per stage, and the stage up-flow rates are the required inputs to the code.

The normal operation of the cascade is managed by designating either the stage cuts or stage up-flow rates in addition to the cascade feed and product rates. Migliorini defines several flow control parameters that can be manipulated to simulate potential off-normal scenarios. A centrifuge scale factor defines the increase of the number of machines in a particular stage and is defined as

$$\zeta_{M,n} = \frac{M_{off-normal,n}}{M_{normal,n}} \tag{6.16}$$

The addition or removal of the machines is assumed to occur instantaneously and defined by a step function as:

$$M_n = \begin{cases} M_{spec,n}, & t = 0 \ldots t_1 \\ M_{spec,n} + \zeta_{M,n}, & t = t_1 \ldots t_2 \\ M_{spec,n}, & t = t_2 \ldots t_{end} \end{cases} \tag{6.17}$$

$M_{spec,n}$ is the specified normal number of centrifuges in each stage obtained from the design of the cascade, t_1 is the designated time for the off-normal operation to begin and t_2 the time in hours when normal operation begins once more. For the simulation performed here, 20% of the centrifuges in the feed stage are assumed to fail during normal operation. This is specified as follows

$$\zeta_{M,nF} = -ceil(0.20 * M_{nF}) \tag{6.18}$$

The negative sign indicates removal of the failed machines and $ceil$ is used to round the number of machines to the nearest integer towards infinity. To simulate the addition of undeclared material into the top stripping stage up-flow, an up-flow withdrawal factor that controls the stage product withdrawal rate is defined similarly to Equation (6.16) as

$$\zeta_{P,n} = \frac{P_{off-normal,n}}{P_{normal,n}} \tag{6.19}$$

The negative value of Equation (6.19) indicates the addition of material. The change from normal to off-normal behavior of the stage product flow rate, P_n, is given by

$$P_n = \begin{cases} 0 & t = 0 \dots t_1 \\ \zeta_{P,n} * \dfrac{t - t_1}{t_2 - t_1} & t = t_1 \dots t_2 \\ \zeta_{P,n} & t = t_2 \dots t_3 \\ \zeta_{P,n} - \zeta_{P,n} * \dfrac{t - t_3}{t_4 - t_3} & t = t_3 \dots t_4 \\ 0 & t = t_4 \dots t_{end} \end{cases} \tag{6.20}$$

In Equation (6.20), t_1 is the initial time the off-normal activity begins, $t_2 - t_1$ is the time period of the ramp function that indicates change to off-normal operation, t_3 is the specified time to return to normal operation and $t_4 - t_3$ is the time period of the ramp function to return back to normal operation. For the simulations conducted here, the ramp function is applied for a period of 15 minutes. The top stripping stage up-flow going into the feed stage is increased by 1% and is given as

$$\zeta_{P,nF-1} = -0.01 * L_{nF-1}, \tag{6.21}$$

where L_{nF-1} is the stage up-flow rate for the stage directly below the feed stage. The isotopic composition of this undeclared material can assumed to be the same as that of the feed material to avoid mixing losses. Based on these specifications, *TransCasc* solves the transient flow as well as gradient equations providing the changes in isotopic concentrations and ratios for the two off-normal scenarios. The differences in such ratios for the intentional and unintentional activities for both the common cascade enriching up to 5% ^{235}U and the HALEU cascade enriching up to 19.75% ^{235}U are highlighted in the next section.

6.6 Results

The two enrichment scenarios for case 1 are investigated first. The isotopic composition of the feed into the single cascade as well as cascade 1 of the two-step design is natural commercial uranium consisting small quantities of ^{232}U and ^{236}U as defined in ATSM C787-06 [94]. This particular type of uranium was selected here to be able to study the minor isotopic ratios in the simulated facility. Table 6.1 describes the input feed concentrations for the isotopes considered.

Table 6.1: Isotopic composition of the commercial NU with trace amounts of ^{232}U and ^{236}U present

Isotope	Feed concentrations [atm %]
^{232}U	1e-09
^{234}U	0.0054
^{235}U	0.72
^{236}U	0.0020
^{238}U	99.27

The cascades were designed to achieve target ^{235}U product concentrations of 19.75% in a single step vs. two steps in which the product of the first cascade is used as feed on to the second. The details of the designed cascades using machine performance from the *Pancake* code are presented in Table 6.2. It can be seen that the number of enriching stages is lower for cascade 2 enriching 5% to 19.75% compared to cascade 1 enriching NU to 5%. This indicates that less effort is needed to produce the higher enrichment. The difference in the total number of machines needed for single cascade and cascade 2 is due to a large stripping section of cascade 2. The target tails 235U concentration for the single cascade is set at 0.3% and the target for cascade 2 is set at 0.72%. However, it takes substantial number of stages to deplete 5% feed to 0.72% than it does 0.72% to 0.3%. Thus, for the purpose of this study, greater focus is placed on the enriching stages and the effort is measured to produce product concentrations rather than the tails.

Table 6.2: Two different cascade types designed to produce HALEU fuel

	Cascade type	Number of enriching stages, NE	Number of stripping stages, NS	Total number of centrifuges, M	Optimal centrifuge separation factor, γ_0	Target ^{235}U product concentration [atm %]
Scenario: 1	Single	25	5	650	1.3238	19.75
Scenario: 2	1	14	5	508	1.3238	5.0
	2	11	13	1072	1.3238	19.75

Table 6.3: The concentrations of the four isotopes in the feed, tails, and product streams for the two enrichment scenarios

	Casc.	**Feed (atm%)**				**Tails (atm %)**				**Product (atm %)**			
		^{232}U	^{234}U	^{235}U	^{236}U	^{232}U	^{234}U	^{235}U	^{236}U	^{232}U	^{234}U	^{235}U	^{236}U
Scen. 1	Single	1.00E-09	0.0054	0.72	0.002	7.86E-11	0.00131	0.303	0.00137	4.31E-08	*0.192*	*19.75*	*0.0310*
Scen. 2	1	1.00E-09	0.0054	0.72	0.002	8.39E-11	0.00137	0.305	0.00129	1.04E-08	0.0469	5.00	0.00927
	2	1.04E-08	0.0469	5.00	0.00927	*3.38E-11*	*0.002004*	*0.705*	*0.00355*	4.62E-08	0.201	19.75	0.0289

Table 6.3 presents the ^{232}U, ^{234}U, ^{235}U, and ^{236}U for the feed, tails, and product of each enrichment scenario as calculated by the squared-off *DesignCascMult* cascade code. While the ^{235}U concentration particles that could be detected range from 0.3%-19.75% for both scenarios, there are slight differences in the minor isotopes and their distributions. These values indicate the isotopic signatures for the feed, tails, and product that could be detected on environmental swipe samples at a particular facility. The differences in the minor isotopics and their ratios with ^{235}U between the two scenarios can be used to predict and/or verify the setup at the location under IAEA investigation. From Table 6.3, the product acquired from the single cascade has a 7% lower ^{232}U, a 5% lower ^{234}U and a 7% higher ^{236}U concentrations than the product from scenario 2. These differences can be explained by the fact that the coupled cascades in scenario 2 are not simulated to recycle their tails concentrations. Since the lighter isotopes get enriched at a faster rate than the heavier ones, the feed concentrations of cascade 2 from scenario 2 have slightly higher amount of lighter ^{232}U and ^{234}U and lower amount of heavier ^{236}U compared to the inner stage in the single cascade from scenario 1 that produces approximately 5% ^{235}U in its product stream. The effect of not mixing the material can further be seen from the tails concentrations of cascade 2 that has lower values of the lighter isotopes and higher values of the heavier one compared to the NU feed for cascade 1. Therefore, the type of enrichment set-up in a particular facility, one continuous cascade vs series of cascades, can affect the concentrations of minor isotopes and nuclear signatures detected by environmental samples. However, such differences are minor for the cascade enriching up to 19.75% compared to HEU fuel studied by Fischer [93].

To further analyze the differences in concentrations throughout the entire cascade rather than simply at the entry and exit ports, the plots of the isotopic signatures are presented in Figure 6.3. The stage product concentrations of the three minor isotopes are plotted against ^{235}U for the three types of cascades described above. Both the enriching and stripping stages are included in the plots. The lighter isotopes increase in concentrations while the heavier one decreases with the increase in ^{235}U concentrations. The differences between the cascade designs are minimal, roughly between 5-7%, for the upper enrichment range; however, it can be noticed that the difference is increasing with increasing concentrations. The ^{236}U concentration varies the most between the different cascades and thus ^{235}U/^{236}U ratio can be a better indication of the enrichment cascade set-up at a particular facility.

As mentioned previously, the cascades designed above use the machine performance maps from the 1-D *Pancake* code. The study was also conducted using the performance data from the 2-D *MultiPort* code, which showed less than 1% difference in the isotopic concentrations throughout the cascades. As seen in Figure 6.3, the ratios of ^{235}U, ^{234}U, and ^{236}U from the two codes are nearly identical. This is expected since the cascades for both solutions are designed with the same feed rate and to achieve the same target enrichments. The isotopic ratios alone, therefore, cannot provide the full picture of the capabilities of individual centrifuges in the facility. It is necessary to also measure the flow rates to corroborate the signatures in an environmental sample and verify declarations.

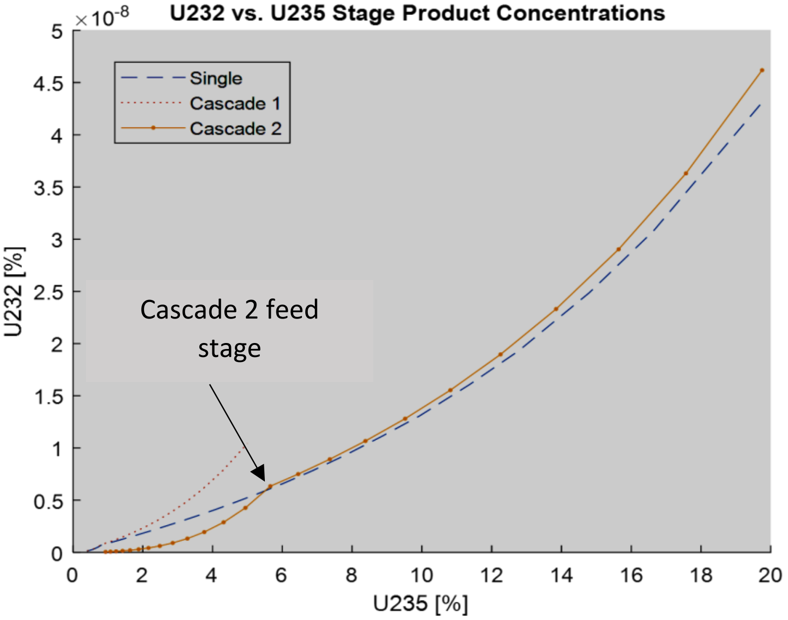

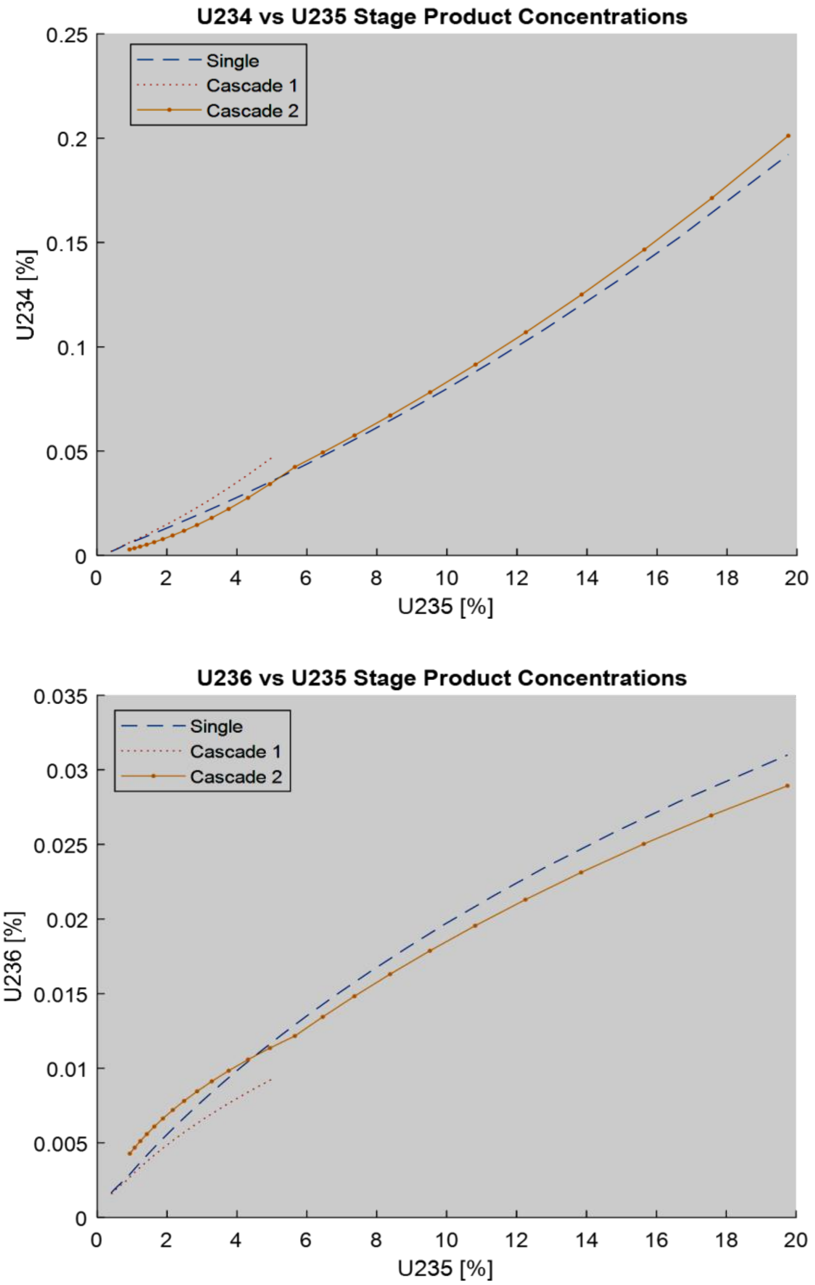

Figure 6.2: The stage product concentrations of the minor isotopes plotted against ^{235}*U for all three cascades from Table 6.2. The plots show the product concentrations for all of the stages in the cascade including those in the stripping section below the feed point.*

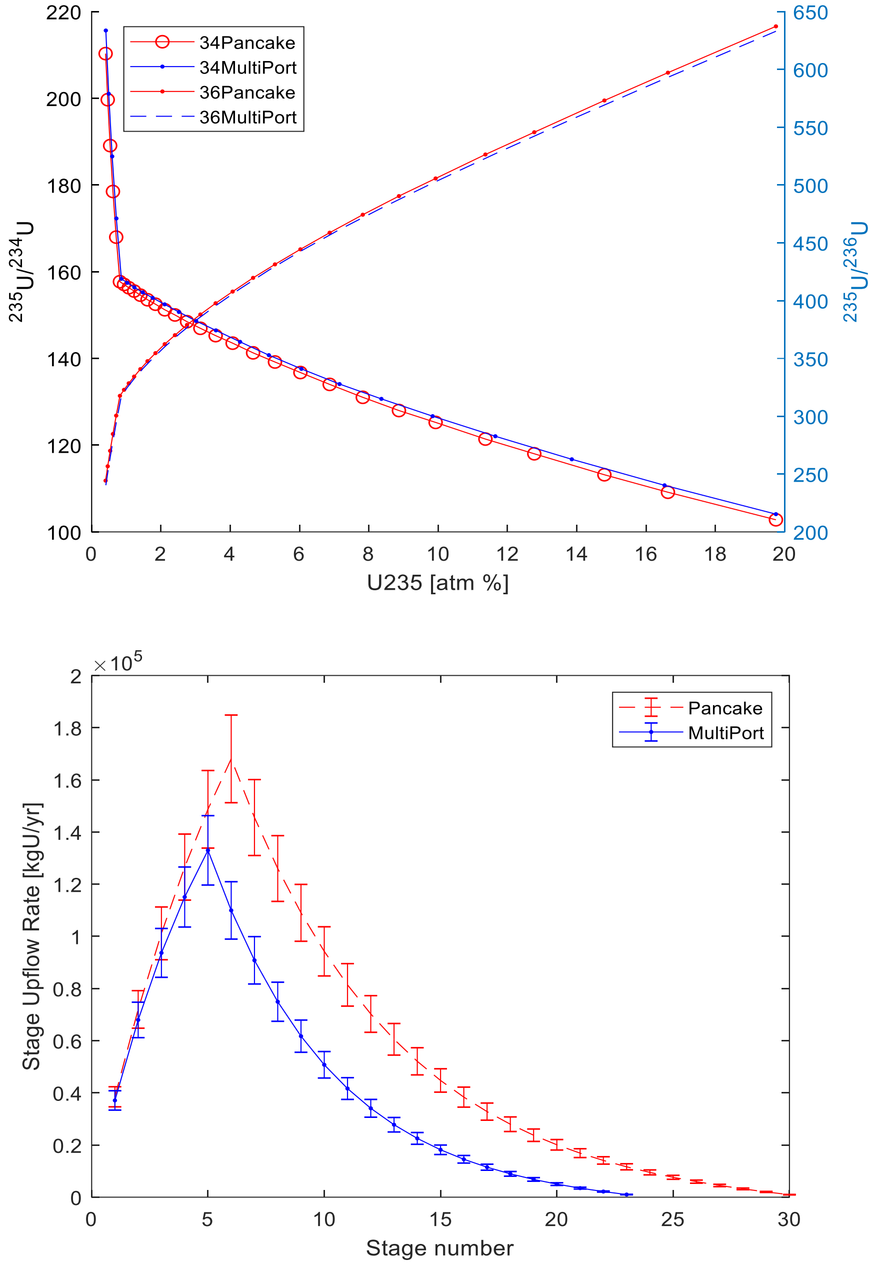

Figure 6.3: Differences between Pancake and MultiPort in terms of the isotopic concentration ratios vs. ^{235}U (top) and stage up-flow rates (bottom). Negligible differences seen for the isotopic ratios. The deviations in the two codes occur in the stage up-flow rates specifically for the enriching sections of the cascades. The error bars show 10% variation in flow rates at each stage.

The next case for this paper involves the simulation of off-normal operations in the HALEU cascade to highlight the distinctions in environmental sampling signatures for intentional and unintentional enrichment activities. The transient study first looks at accidental machine failures followed by purposeful manipulation of the flow rates. Since the isotopic ratios produced by the two sets of performance maps are identical, the results presented here used the cascade designed using the

Pancake solution. The two cascades from scenario 2 described above in in Table 6.2. It can be seen that the number of enriching stages is lower for cascade 2 enriching 5% to 19.75% compared to cascade 1 enriching NU to 5%. This indicates that less effort is needed to produce the higher enrichment. The difference in the total number of machines needed for single cascade and cascade 2 is due to a large stripping section of cascade 2. The target tails 235U concentration for the single cascade is set at 0.3% and the target for cascade 2 is set at 0.72%. However, it takes substantial number of stages to deplete 5% feed to 0.72% than it does 0.72% to 0.3%. Thus, for the purpose of this study, greater focus is placed on the enriching stages and the effort is measured to produce product concentrations rather than the tails.

Table 6.2 are simulated to apprehend how the isotopic signatures can vary between the common cascade enriching up to 5% ^{235}U and the HALEU cascade enriching up to 19.75% ^{235}U. For the HALEU cascade in Figure 6.4, the case of centrifuge failure reveals an initial decrease in the ^{232}U/^{235}U and ^{234}U/^{235}U ratios followed by a gradual increase greater than the normal operational level. For the case of the misuse, there is an initial increase in the ratio and a gradual decrease that remains less than the normal ratio. The ^{236}U behavior is different, which indicates that the ratio of the light minor isotopes to ^{235}U can indicate misuse in a cascade. The variations in the ratios are small and can fall within the target uncertainties of the on-line enrichment monitors that can detect changes near or above 0.2%.

(a)

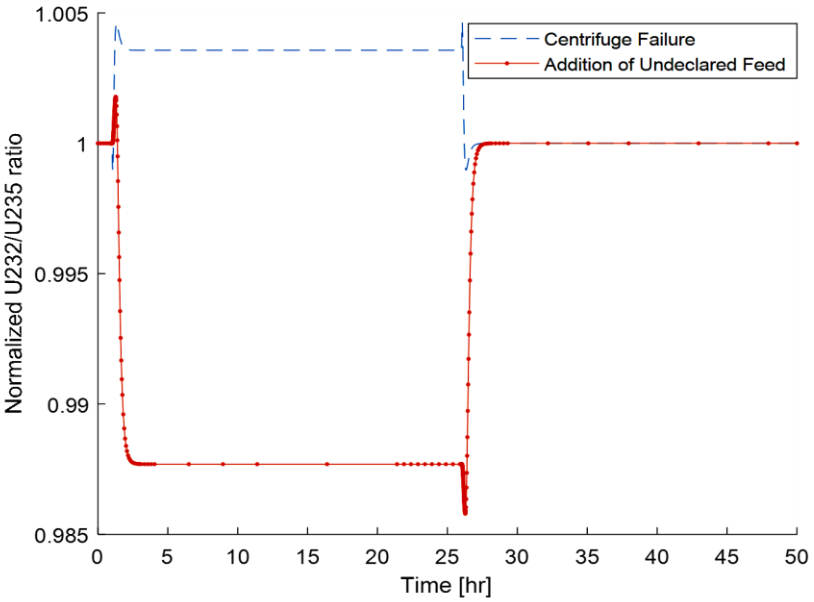

(b)

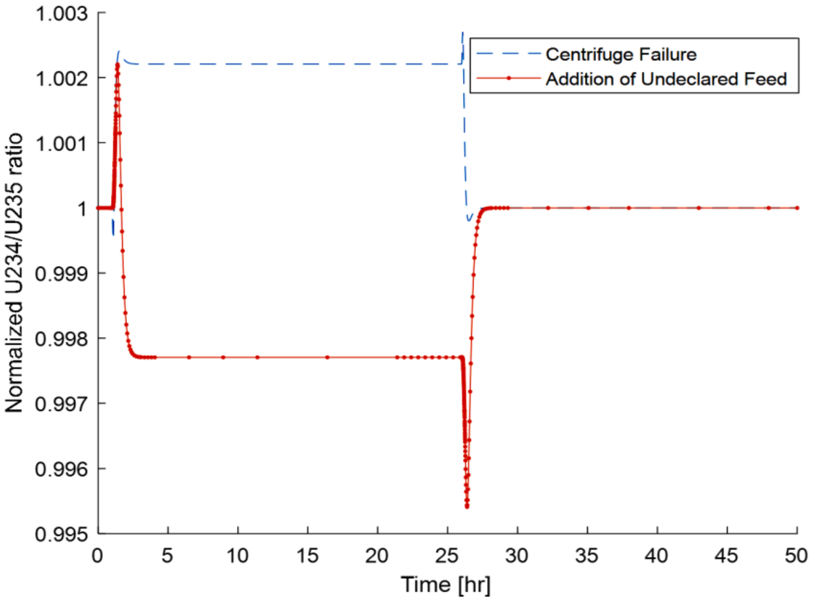

(c)

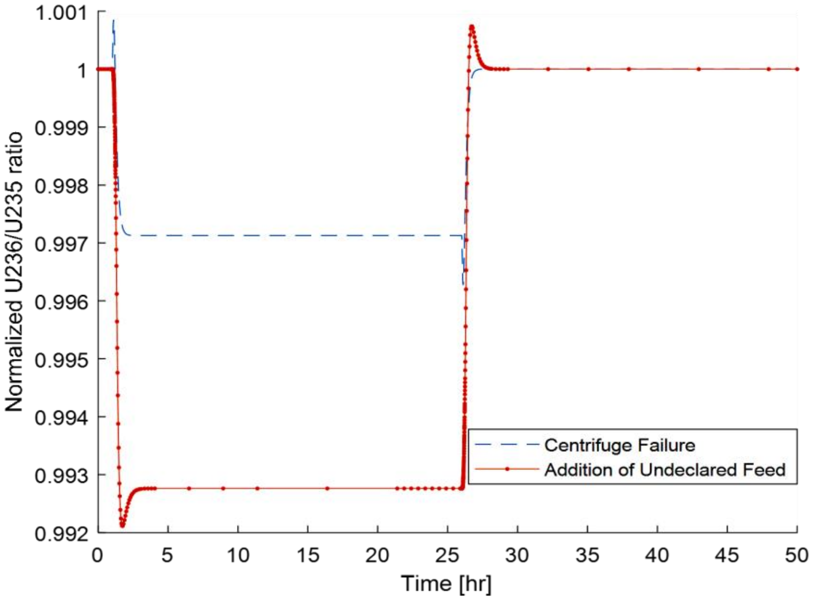

Figure 6.4: The ratios of minor isotopes (a) ^{232}U, (b) ^{234}U, and (c) ^{236}U to ^{235}U normalized by the values of normal operations plotted over the simulation time given in hours for a Rome cascade. The facility was in operation for 50 hours. At hour 1, the intentional off-normal scenario occurs over a 15-minute period. At hour 26, the normal operation is resumed during another 15-minute interval. The behavior of lighter minor isotopes clearly shows the difference between intentional and unintentional occurrences.

Figure 6.5 provides a magnified view of the isotopic ratio plots for the two off-normal scenarios simulated. Once again, the behavior of the minor isotopes between the two cases is evidently inconsistent. The transition time, defined as the time it takes for the ratios to reach a new steady value, differs between the two scenarios. For the unintentional centrifuge failure, the transition time from normal to off-normal signatures is on the order of approximately 1.5 hours as seen in Figure 6.5a) while for the intentional addition of material, the time is longer on the order of 2.5 hours. This is promising from the safeguards point of view since the detectable phenomena for an intentional misuse can remain in the cascade for a longer period of time. It is also beneficial to know if the transition time for an abnormal event falls within the notification timeframe during a short notice random inspections conducted by the IAEA inspectors.

(a)

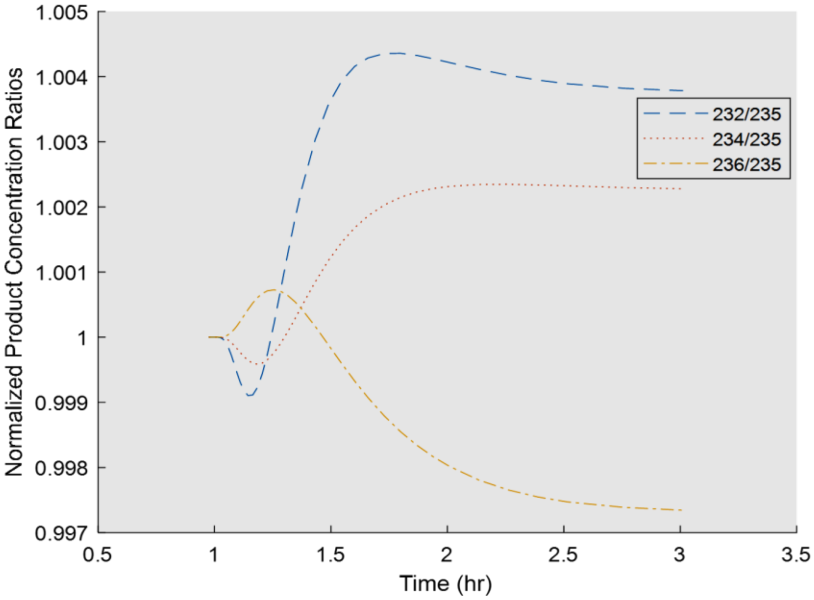

(b)

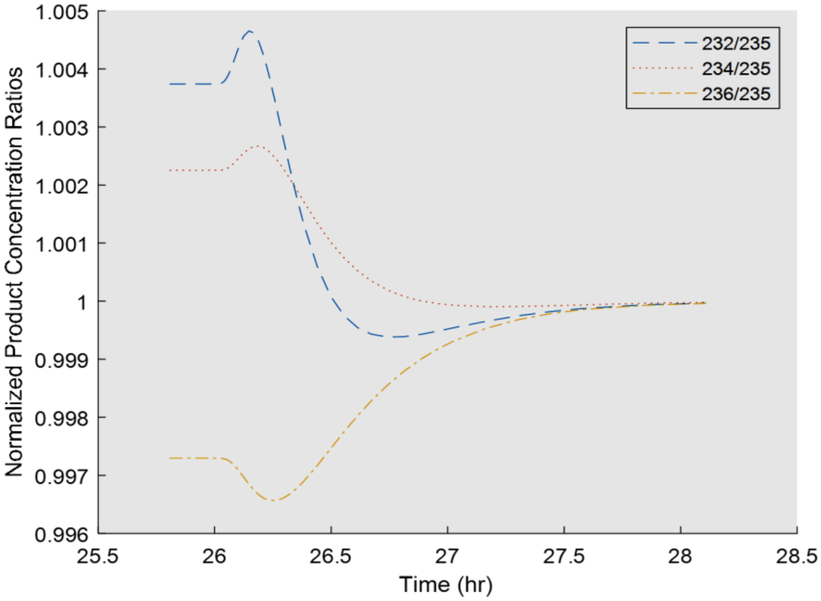

1.005
1.004
1.003
1.002
1.001
1
0.999
0.998
0.997
0.996
25.5
26
26.5
27
27.5
28
28.5
Time (hr)
Normalized Product Concentration Ratios
232/235
234/235
236/235

(c)

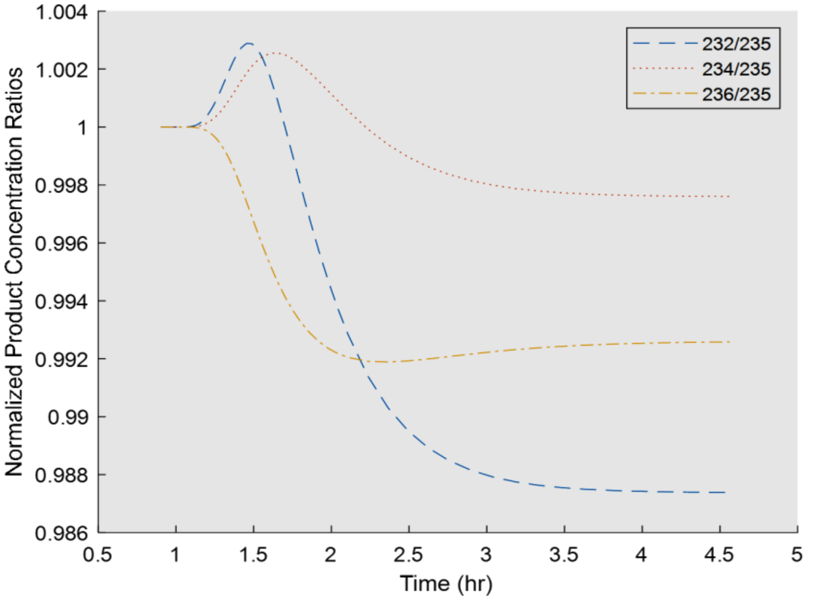

1.004
1.002
1
0.998
0.996
0.994
0.992
0.99
0.988
0.986
0.5
1
1.5
2
2.5
3
3.5
4
4.5
5
Time (hr)
Normalized Product Concentration Ratios
232/235
234/235
236/235

(d)

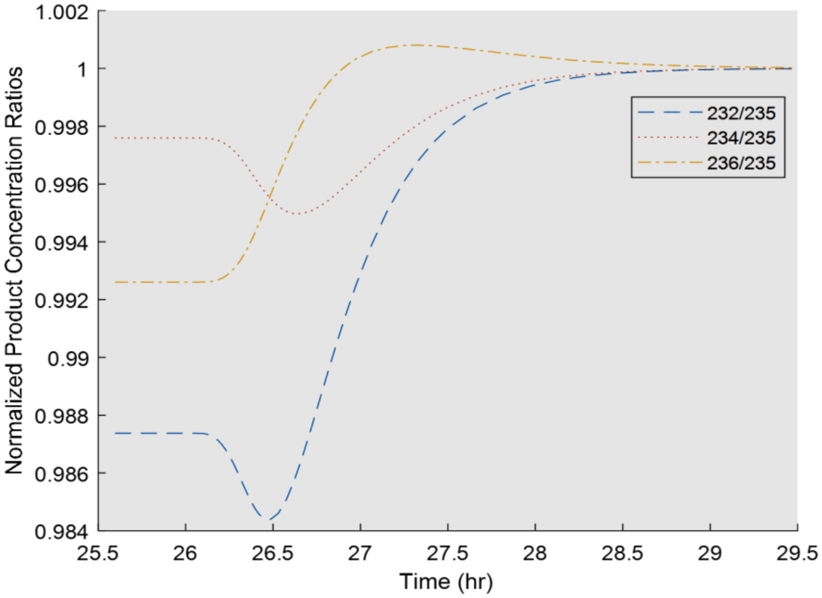

Figure 6.5: The normalized product concentration ratios of the minor isotopes during the transition time between normal and off-normal operations for a), b) centrifuge failures and c), d) addition of undeclared feed

The isotopic ratios for the HALEU cascades above differ from those of a cascade enriching only up to 5% ^{235}U. Figure 6.6 shows that the ratios are smaller for the LEU cascades. Furthermore, the intentional misuse curves for the lighter isotope ratios remain fairly close to normal operation levels except for the sharp changes during transition time. This makes it difficult to detect anomalies with the swipe samples since the particles remain in the environment for a shorter period of time. The ^{236}U ratio can be a good indicator of intentional misuse in an LEU cascade since the centrifuge failure only causes about 0.089% diversion from normal while the addition of undeclared material differs from normal by roughly 0.25% as indicated in the figure. Overall, the isotopic ratios for HALEU cascade vary by about 1% more from normal operation compared to LEU for both intentional and unintentional changes. Therefore, the environmental samples at the HALEU facility would be slightly more capable of detecting particles compared to LEU, which is expected because of the higher enrichments.

(a)

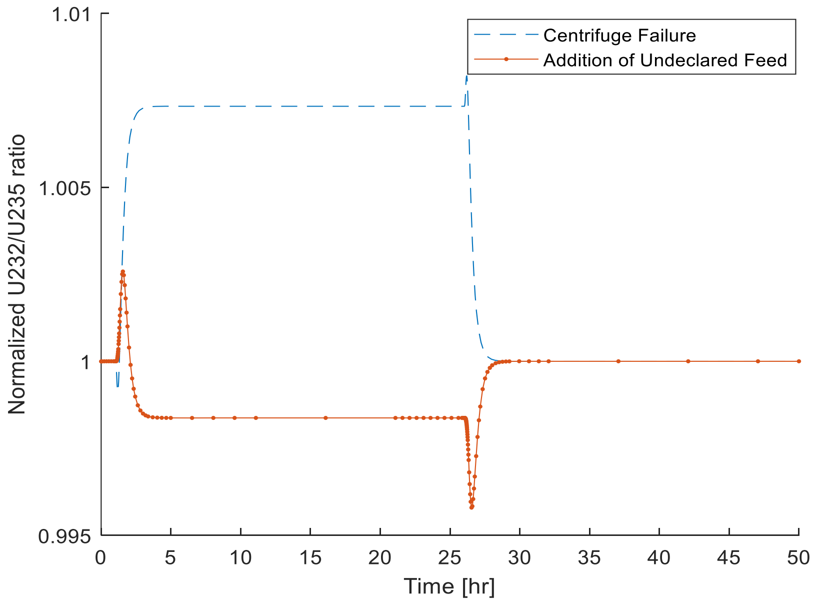
1.01
1.005
1
0.995
Normalized U232/U235 ratio
0
5
10
15
20
25
30
35
40
45
50
Time [hr]
Centrifuge Failure
Addition of Undeclared Feed

b)

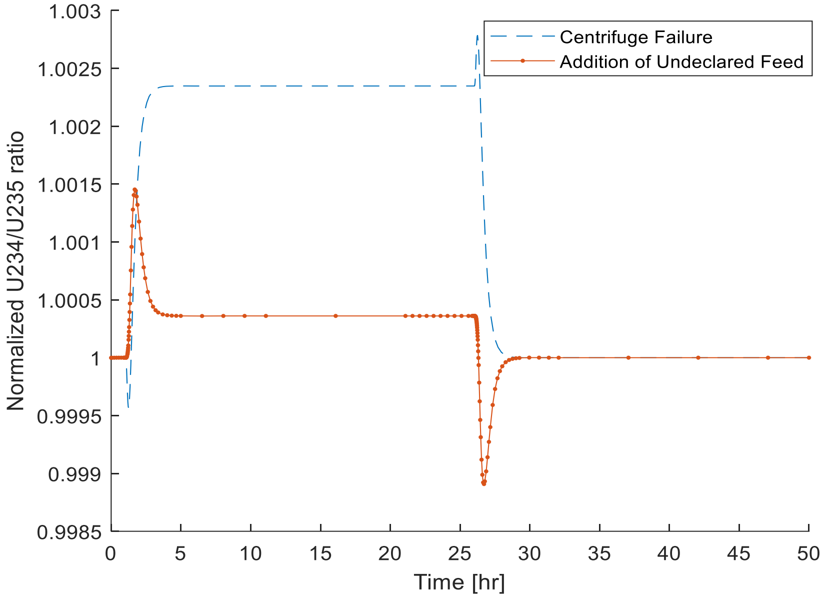
1.003
1.0025
1.002
1.0015
1.001
1.0005
1
0.9995
0.999
0.9985
Normalized U234/U235 ratio
0
5
10
15
20
25
30
35
40
45
50
Time [hr]
Centrifuge Failure
Addition of Undeclared Feed

(c)

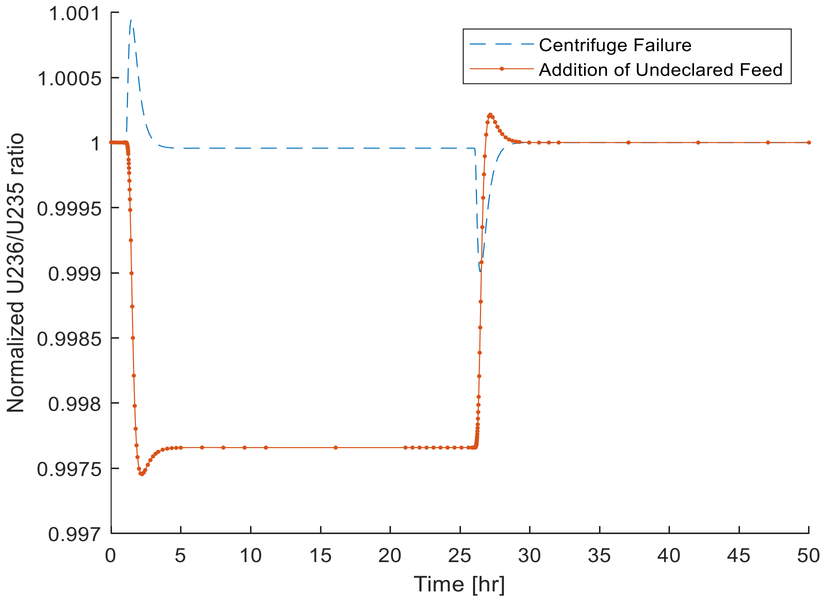

Figure 6.6: Normalized minor isotopic ratios in an LEU Rome cascade for off-normal scenarios. The behavior of the lighter isotopic ratios in an intentional misuse case is different from that of a HALEU cascade.

The off-normal scenarios presented so far are for Rome cascades. The study is expanded by designing cascades for Iguacu centrifuges to understand the isotopic variations in such facilities. Since the machine performance maps obtained from simplified 1-D versus the new 2-D model are similar as shown above, the data from the *Pancake* code presented in Figure 6.7 is used for this analysis. Two cascades are designed to enrich NU to 19.75% and the details are presented in Table 6.4 .

Table 6.4: Two enrichment scenarios to produce 19.75% ^{235}U product concentration using Iguaçu centrifuges

	Cascade type	**Number of enriching stages, NE**	**Number of stripping stages, NS**	**Total number of centrifuges, M**	**Optimal centrifuge separation factor, γ_0**	**Target ^{235}U product concentration [atm %]**
Scenario: 1	Single	28	6	8209	1.2817	19.75
Scenario: 2	1	16	6	6485	1.2817	5.0
	2	12	15	13175	1.2817	19.75

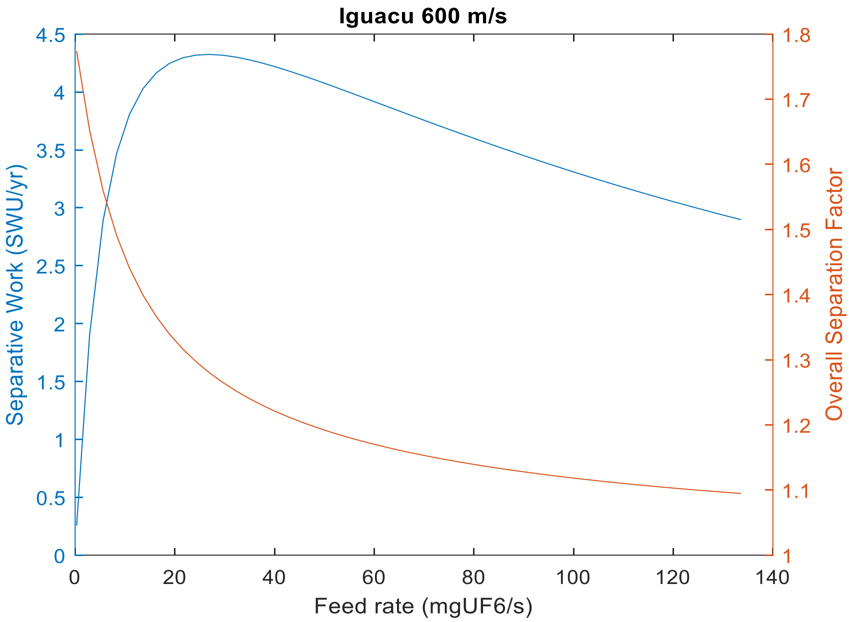

Figure 6.7: Performance map of the Iguaçu centrifuge showing the change in separation parameters over a range of feed rates. The optimal feed rate is 28 mgUF$_6$/s and the overall separation factor corresponding to that value is 1.2817.

Since the Iguacu cascades in Table 6.4 are designed to produce the same tails and product concentrations as the Rome cascades in Table 6.2, the isotopic concentrations in the feed, product, and tails streams will be the same as those reported for Rome in Table 6.3. The differences between the cascades will be in the behavior of minor isotopes during off-normal occurrences in the facility. The normalized isotopic ratios for the Iguacu cascades enriching NU to 5% target ^{235}U and 5% to 19.75% ^{235}U are presented below. It is important to note that the Iguacu cascades show significantly smaller transition time between normal and off-normal situations. This could result from the fact that Iguacu cascades require significantly greater number of machines to achieve the same enrichment as Rome. Therefore, small changes in the cascade such as 20% of the machines failing in the feed stage and 1% additional material added to the top stripping stage upflow can have less of an impact of the enrichment ratios compared to Rome cascades. This further indicates that the particles from off-normal activities remain in the environment for a shorter period of time thus making it more challenging to capture and detect through sampling. Therefore, additional safeguarding measures such as continuous online monitoring and more frequent unannounced inspections are necessary in facilities using machines with smaller aspect ratios in addition to environmental sampling to verify the operators' declarations.

(a)

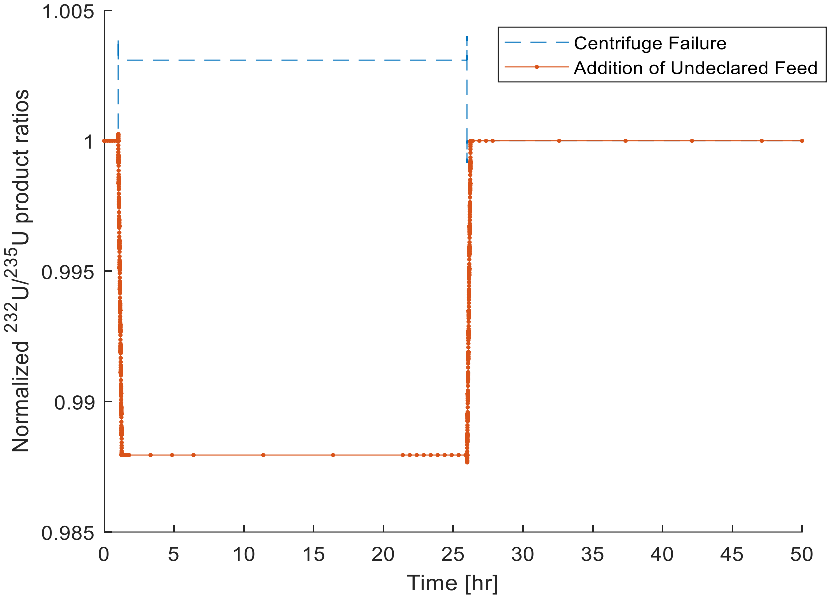
Centrifuge Failure
Addition of Undeclared Feed
Normalized $^{232}U/^{235}U$ product ratios
1.005
1
0.995
0.99
0.985
0
5
10
15
20
25
30
35
40
45
50
Time [hr]

(b)

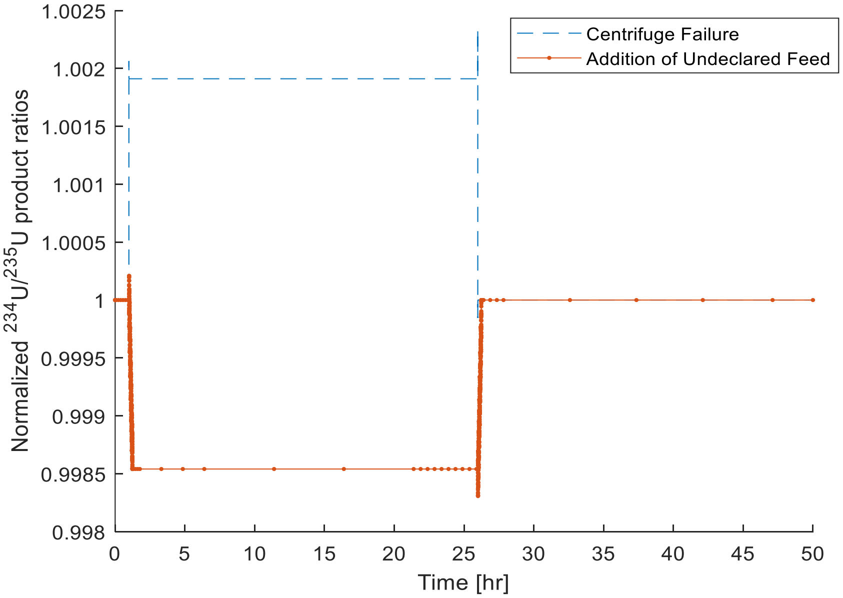
Centrifuge Failure
Addition of Undeclared Feed
Normalized $^{234}U/^{235}U$ product ratios
1.0025
1.002
1.0015
1.001
1.0005
1
0.9995
0.999
0.9985
0.998
0
5
10
15
20
25
30
35
40
45
50
Time [hr]

(c)

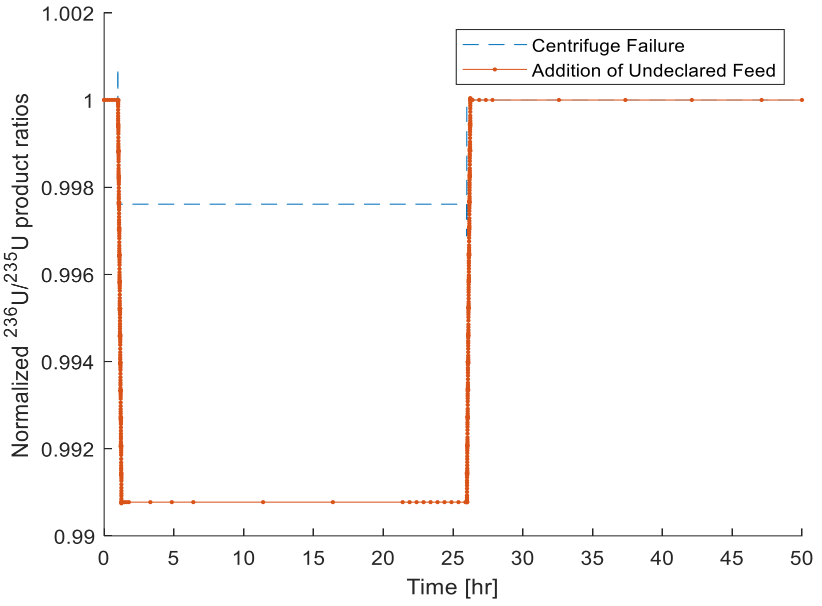

Figure 6.8: The ratios of minor isotopes (a) ^{232}U, (b) ^{234}U, and (c) ^{236}U to ^{235}U normalized by the values of normal operations plotted over the simulation time given in hours for a HALEU Iguaçu cascade.

(a)

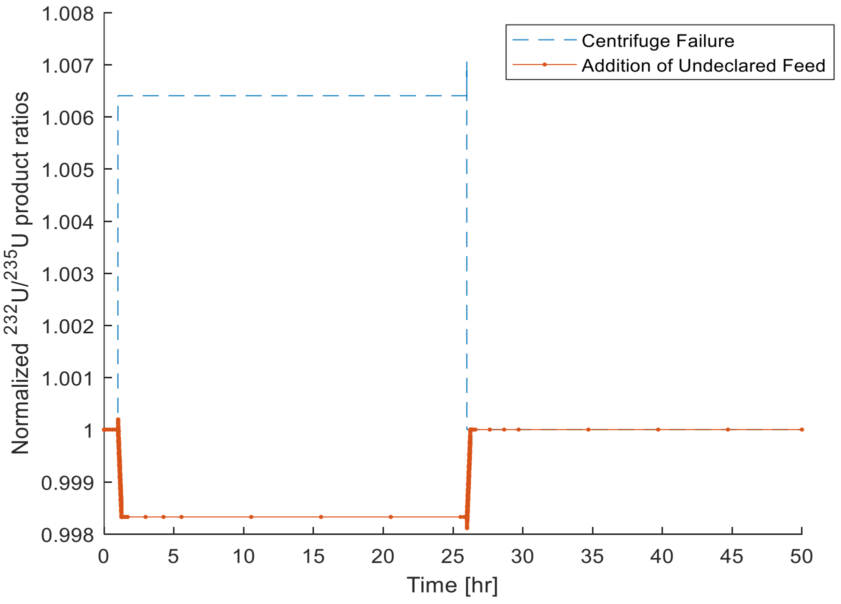

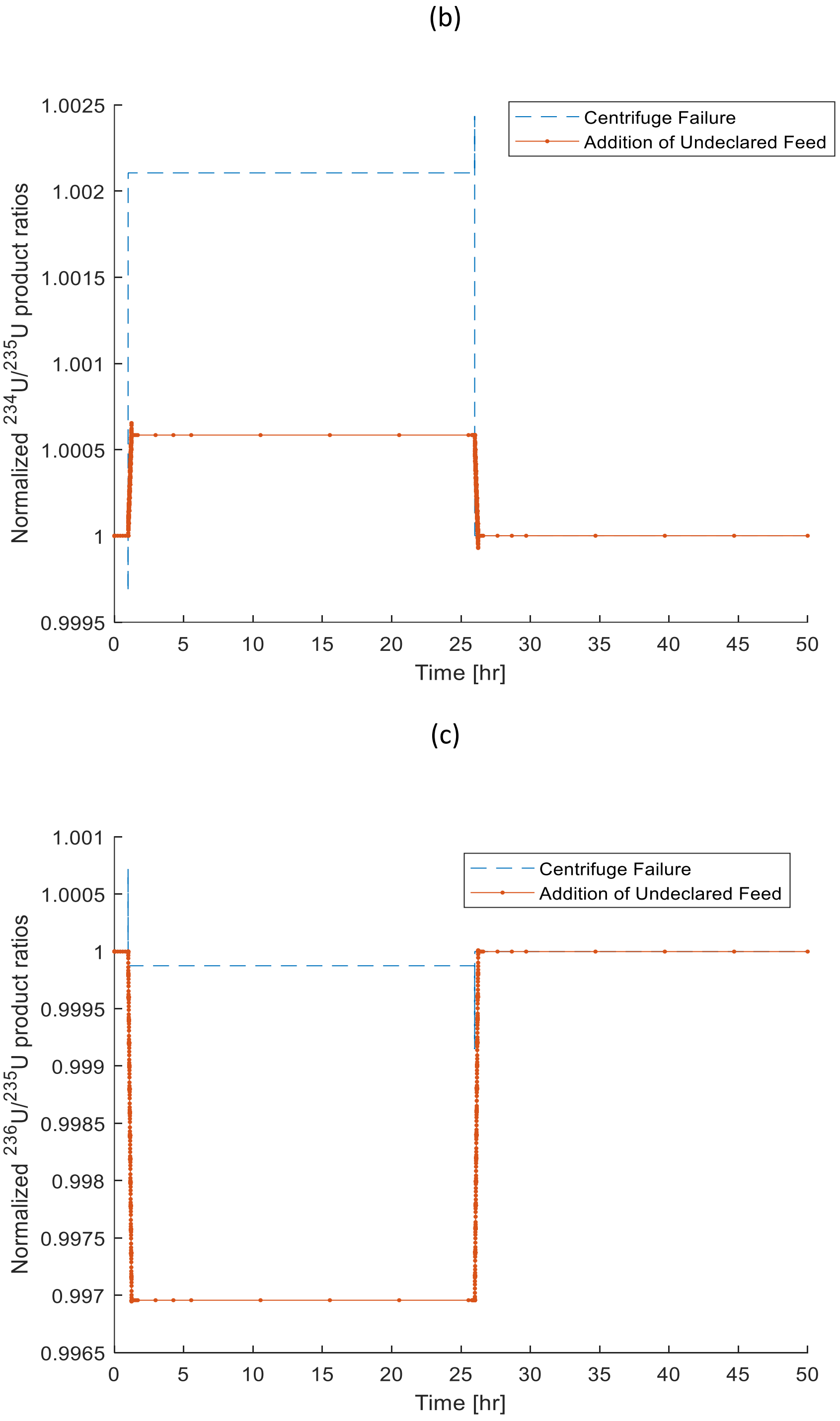

Figure 6.9: The ratios of minor isotopes (a) ^{232}U, (b) ^{234}U, and (c) ^{236}U to ^{235}U normalized by the values of normal operations plotted over the simulation time given in hours for an LEU Iguaçu cascade.

6.7 Summary and Conclusions

Two different centrifuge modeling software were used to obtain the performance map of a fictitious Rome machine. It was shown that the optimal operating point of the centrifuge can vary by approximately 30% between the 1-D and 2-D diffusion codes. However, associated difference in the overall separation factor was only about 5%. The performance maps were then used to design a HALEU cascade by adopting two approaches. The isotopic signatures of the minor isotopes varied by roughly 5% among the two enrichment scenarios. The solutions obtained from *Pancake* and *MultiPort* code showed no significant variations in the isotopic ratios. This shows that the individual centrifuge data from a simplified 1-D solution is sufficiently accurate to perform cascade analysis. The final section included the simulation of off-normal operations on the LEU vs. HALEU cascades. The concentration ratios of the lighter minor isotopes demonstrate distinct behavior for an accidental vs. intentional misuse in a facility. The variations in the ratios are quite small and most fall within the uncertainties of the on-line enrichment monitors. However, the ^{232}U to ^{235}U ratios have differences of around 1% for the HALEU cascade that can be detected by the enrichment monitors. It was also shown that the HALEU cascade diverted more from normal to off-normal operation for the misuse scenarios studied, which is a positive finding in terms of being able to detect undeclared activities at such facility. This is because greater diversions are better captured by IAEA measures and monitoring technologies. Additionally, it takes longer for the operation to return to normal in a HALEU cascade providing greater window of detection during random IAEA inspections. On the whole, a higher fidelity single machine model is not necessary to perform cascade level analysis of isotopic signatures. Such isotope ratios analyzed using swipe samples can vary depending on the structure of the enrichment facility as well as between illicit activities and unplanned accidents. And finally, the HALEU fuel development will not require modifications of the current safeguards measures since the isotopic signatures for potential misuse cases simulated here are more detectable than the LEU fuel. A future extension of this work can include simulations of multiple proliferation scenarios and further analysis of how the cascade flow rates vary between the 1-D and the 2-D solutions.

Chapter 7

Summary, Conclusions, and Future Work

7.1 Dissertation Summary and Anticipated Impact

The rising international tensions in the recent times, especially involving the nations with numerous nuclear weapons, have signified the necessity of pronounced efforts towards deterrence and non-proliferation. It is of utmost importance to the United States and the IAEA in general to have resources in place that can assist in eradicating and/or limiting the misuse of nuclear technology. Whether to calculate the capacities of adversaries or to promote transparency when it comes to a state's handling of nuclear material, it is imperative to analyze the nuclear fuel cycle, particularly the enrichment of uranium. However, this subject is sensitive and proprietary, which often makes it difficult for the IAEA to gather accurate information, despite several international treaties and safeguard measures in place. In order to bolster the agency's efforts, this dissertation looks to add to the current inventory of computer models that permit the prediction of capabilities of enrichment technology without the need of every detail from the facility or the State as a whole.

The work completed in this dissertation is part of the series of research efforts that involve the development and refinement of computational models to accurately understand the physics inside the gas centrifuge and apply that knowledge to enhance cascade analysis. Based on the numerical codes constructed over the past decade at the University of Virginia, this work advanced and augmented their features and in turn produced new program to present higher dimensional analysis. This research, therefore, contributes to the general theory of isotopic diffusion inside a single gas centrifuge, quantification of uncertainty associated with the developed models, cascade modeling, and non-proliferation and safeguards analyses.

The first aspect of the work involved the refinement of the previously developed finite element model simulating the hydrodynamics inside the gas centrifuge rotor. Four different ways of modeling the sources and sinks of mass, momentum, and energy were described and the impact of each on the produced mass flow and isotopic diffusion were highlighted. Previously implemented function proved to introduce anomalies for larger operational values in the two-dimensional analysis of isotopic diffusion that was not captured by the past studies or 1-D models. A mathematical function that best describes the physics as well as eliminates numerical error is identified and appended to the previous version of the mass flow model.

Next, making use of the upgrade to the fluid dynamic model, a new finite element code solving the isotopic diffusion inside the centrifuge rotor is written for a two-dimensional multi-component domain. This is the first of the models that adds such complexity in a single platform to obtain a comprehensive analysis of the dissemination of individual uranium isotopes inside the rotor volume. Having the capability to quantify isotopic concentrations at any desired radial and axial location is crucial during a destructive analysis of the machine samples. Furthermore, the knowledge regarding not only the major uranium isotopes, ^{235}U and ^{238}U, but also the minor ^{234}U and ^{236}U can furnish insights into the historical use of the machine being analyzed. The output of the new code is verified by comparing against previous 1-D models; however, a complete validation has proved difficult due to the lack of open-source literature on the experimental work involving gas centrifuges.

To tackle the problem with code verification, a sensitivity analysis and uncertainty quantification of the finite element diffusion model is performed. Several key input parameters are identified and randomized to set up statistically significant simulations. The output parameter, the machine's separation factor that is solely the function of isotopic concentrations at the exit ports, is obtained for each simulated case. It is shown that the most influential input parameters include the machine's rotation and the cut of the machine. For the uncertainty quantification analysis, each of the input parameters are varied by the 20% off of their nominal values. It is observed that the separation factor only varied by approximately 15% off the normal value, indicating the fact that uncertainty in inputs propagates essentially linearly to the output. This ensures that no additional numerical errors are introduced by the developed model providing a greater confidence in the results obtained. Additionally, the methodology explored here can be applied in the field to account for uncertainty when the IAEA inspectors may not have the exact facilities' operational data.

Finally, the single machine models are combined with the cascade analysis to study multi-isotopic gradients in an enrichment facility. The machine performance obtained from the 2D multicomponent diffusion code is compared against the results from the previous 1D solutions. Following centrifuge data, two sets of cascades are designed, one enriching NU to 5% and another 5% to 19.75%. Using previously developed transient cascade models, two off-normal simulations are conducted to highlight the differences in the uranium isotopic ratios. The concentration ratios for the lighter minor isotopes distinctly differ for an intentional misuse compared to accidental incidents in the facility. It is also shown that for the higher enrichment case, isotopic signatures differed greatly from normal to off-normal transitions compared to the lower, which indicates that it is easier to detect misuse for such enrichments. This is a positive outcome since uranium enrichment to 19.75% has been more common in the past few years for the application in the advanced nuclear reactors. The study ensured that safeguarding these higher enrichment activities will not require additional measures by the IAEA.

The above-mentioned studies for this dissertation have been published or in the process of being published in the open forum at the time of writing. Overall, throughout the entire research process over the past few years as well as in the near future, the contributions to the scientific literature include:

1) Four peer-reviewed journal articles directly correlating with Chapters 3-6, with one in publication, another one submitted, and the last two in final phase of preparation at the time of writing.
2) Four conference papers and posters in Institute of Nuclear Material and Management (INMM) and Separation Phenomena on Liquids and Gases (SPLG)
3) Two software (*MultiPort,* and modification to *CurvSOL*)

7.2 Future Work

The future direction of the current research efforts needs to be identified for continuous improvement and addition to this work. Some noticeable subject matter of interest include:

1. Exploration of more intricate physics inside the centrifuge rotor. The current version of the mass flow as well as multi-component diffusion code use a simplified representation of the rotor to produce respective solutions. Some of the missing aspects include studying the diffusion of isotopes at the very thin Ekman layers near the top and bottom boundaries of the machine. The radial velocity is dominant over the axial in these thin Ekman layers, and it would be beneficial to understand the degree of impact that has on the radial isotopic diffusion at the machine's end plates. Furthermore, the current models do not account for the baffle chamber of the centrifuge. The upper boundary is placed right before the baffle and the concentrations out of the machine are assumed to equal the concentrations at the boundary. However, the perforation of the baffle disk and the space in the chamber prior to the machine's extraction point can slow the flow of gas and perhaps impact diffusion. Creating a fluid dynamics model of this section of the rotor and adding its complexity to the multicomponent code can assist in quantifying potential inaccuracies in the current simplified model.

2. Comparison of the current results with experimental data to validate the codes. While a detailed discussion on the verification techniques and uncertainty quantification is provided, the dissertation is still missing a proper validation with experimental data. This is difficult to obtain for uranium separation in the open-source forum. However, the use of the developed models in practice is encouraged to be done after a proper comparison against available experimental data.
3. Study of additional off-normal scenarios in the cascade halls. The presented results in Chapter 6 are limited to two potential unexpected operations; however, in reality there could be dozens of ways that a proliferator can exploit peaceful or declared development of nuclear material. It will be beneficial to prepare a detailed report including the changes in isotopic signatures for all such cases.

References

[1] E. Tretkoff, "December 1938: Discovery of Nuclear Fission," *APS News,* vol. 16, no. 11, p. 2, December 2007.

[2] K. Davenport, "Nuclear Weapons:: Who Has What At A Glance," Arms Control Association, August 2020. [Online]. [Accessed February 2021].

[3] D. D. Eisenhower, *Atoms for Peace,* New York, NY: 470th Plenary Meeting of the United Nations General Assembly, December 8, 1953.

[4] International Atomic Energy Agency, "The Statute of the IAEA," [Online]. Available: iaea.org/about/statute. [Accessed February 2022].

[5] International Atomic Energy Agency, "IAEA and the Non-Proliferation Treaty," [Online]. Available: iaea.org/topics/non-proliferation-treaty. [Accessed February 2022].

[6] International Atomic Energy Agency, "Information Circular/ 140: Treaty on the Non-Proliferation of Nuclear Weapons," IAEA, Vienna, Austria, 1970.

[7] International Atomic Energy Agency, "Implementation of the Agreement between the Agency and the Democratic People's Republic of Korea for the Application of Safeguards in Connection with the Treaty on the Nonproliferation of Nuclear Weapons," IAEA, Vienna, Austria, 1993.

[8] M. Rosenthal and W. M. Stern, "Deterring Nuclear Proliferation: The Importance of IAEA Safeguards, 2nd ed.," Brookhaven Science Associates, LLC, Brookhaven, NY, April 2019.

[9] Nuclear Threat Initiative, "Iraq Nuclear Facilities," 7 December 2011. [Online]. Available: nti.org/analysis/articles/iraq-nuclear-facilities/. [Accessed February 2022].

[10] James Martin Center for Nonproliferation Studies at the Middlebury Institute of International Studies at Monterey, "Iran Nuclear Overview," 25 June 2020. [Online]. Available: nti.org/analysis/articles/iran-nuclear/. [Accessed February 2022].

[11] D. Kimball, "Arms Control Association: Comprehensive Test Ban Treaty at a Glance," July 2020. [Online]. Available: armscontrol.org/factsheets/test-ban-treaty-at-a-glance. [Accessed February 2022].

[12] International Atomic Energy Agency, "Additional Protocol," [Online]. Available: iaea.org/topics/additional-protocol. [Accessed February 2022].

[13] U.S. Energy Information Administration, "Nuclear Explained: Nuclear," 14 July 2021. [Online]. Available: eia.gov/energyexplained/nuclear/. [Accessed February 2022].

[14] World Nuclear Association, "Nuclear Power Reactors," World Nuclear Association, March 2022. [Online]. Available: https://world-nuclear.org/information-library/nuclear-fuel-cycle/nuclear-power-reactors/nuclear-power-reactors.aspx. [Accessed April 2022].

[15] R. DeWitt, "Uranium Hexafluoride: A Survey of the Physico-Chemical Properties," Goodyear Atomic Corporation, Portsmouth, Ohio, 1960.

[16] U.S. Energy Information Administration, "Nuclear Explained: The Nuclear Fuel Cycle," 21 June 2021. [Online]. Available: eia.gov/energyexplained/nuclear/the-nuclear-fuel-cycle.php. [Accessed 2022].

[17] H. D. Smyth, "Atomic Energy for Military Purposes," Princeton University Press, Princeton, NJ, 1945.

[18] M. Benedict and C. Williams, Engineering Dvelopments in the Gaseous Diffusion Process, New York: McGraw-Hill, 1949.

[19] U.S. Department of Energy- Office of History and Heritage Resources, "The Manhattan Project an Interactive history," U.S. Department of Energy, [Online]. Available: https://www.osti.gov/opennet/manhattan-project-history/Processes/UraniumSeparation/electromagnetic.html. [Accessed April 2022].

[20] S. Villani and E. W. Becker, "Separation Nozzle," in *Uranium Enrichment*, Heidelberg, Germany, Springer-Verlag, 1979, pp. 245-290.

[21] S. Villani, C. P. Robinson and R. J. Jensen, "Laser Methods of Uranium Isotope Separation," in *Uranium Enrichment*, Heidelberg, Germany, Springer-Verlag, 1979, pp. 269-290.

[22] F. A. Lindeman and F. W. Aston, "The Possibility of Separating Isotopes," *Philosophical Magazine and Journal of Science,* vol. 37, no. 221, pp. 523-534, 1919.

[23] J. W. Beams, A. C. Hagg and E. V. Murphree, "Developments in the Centrifuge Separation Project," United States Atomic Energy Commission: Office of Technical Information, Washington, D.C., 1951.

[24] G. Zippe, "The Development of Short Bowl Ultracentrifuges Report no. EP-4420-101-60U," University of Virginia, Charlottesville, VA, 1960.

[25] H. Wood, A. Glaser and S. Kemp, "The Gas Centrifuge and Nuclear Weapons Proliferation," *Physics Today,* pp. 40-45, September 2008.

[26] D. A. Waters, "The American Gas Centrifuge Past, Present, and Future," in *Workshop on Separation Phenomena in Liquids and Gases (SPLG)*, 2003.

[27] S. Whitley, "Review of the gas centrifuge until 1962. Part I: Principles of separation physics," *Reviews of Modern Physics,* vol. 56, no. 1, pp. 41-65, 1984.

[28] F. Doneddu, "Uranium Enrichment: Centrifuge Process," in *International Seminar on Nuclear Fuel Cycle*, 2004.

[29] D. R. Olander, "The Gas Centrifuge," *Scientific American,* vol. 239, no. 2, pp. 37-43, 1978.

[30] Soubbaramayer, Centrifugation: Uranium Enrichment, vol. 35, S. Villani, Ed., New York, NY: Springer-Verlag Berlin Heidelberg, 1979.

[31] L. Onsager, "Approximate Solutions of the Linearized Flow Equations," 1965.

[32] H. G. Wood and J. B. Morton, "Onsager's Pancake Approximation for the Fluid Dynamics of a Gas Centrifuge," *Journal of Fluid Mechanics,* vol. 101, no. 1, pp. 1-31, 1980.

[33] K. Stewartson, "On Almost Rigid Rotations," *Journal of Fluid Mechanics,* vol. 3, pp. 17-26, 1959.

[34] V. W. Ekman, "On the Influence of the Earth's Rotation on Ocean Currents," *Arkin. Mat. Astron. och Fysik,* vol. 2, no. 11, 1905.

[35] R. Babarsky and H. G. Wood, "An Analysis from First Principles of the Source/Sink Terms in the Pancake Equation," University of Virginia, Charlottesville, VA, 982.

[36] H. G. Wood and G. Sanders, "Rotating Compressible Flows with Internal Sources and Sinks," *Journal of Fluid Mechanics,* vol. 127, pp. 299-313, 1983.

[37] H. G. Wood,, J. A. Jordan and M. D. Gunzburger, "The Effects of Curvature on the Flow Field in Rapidly Rotating Gas Centrifuges," *J. Fluid Mech,* vol. 140, pp. 373-395, 1984.

[38] J. A. Viecelli, "Exponential Difference Operator Approximation for the Sixth Order Onsager Equation," *J. Comp. Phys.,* vol. 50, pp. 162-170, 1983.

[39] M. D. Gunzburger and H. G. Wood, "A Finite Element Method for the Onsager Pancake Equation," *Computer Methods in Applied Mechanics and Engineering,* vol. 31, no. 1, pp. 43-59, July 1982.

[40] M. D. Gunzburger, H. G. Wood and J. A. Jordan, "A Finite Element Method for Gas Centrifuge Flow Problems," *SIAM J. Sci. Stat. Comput.,* vol. 5, no. 1, pp. 78-94, March 1984.

[41] R. Bourn,, T. E. Peterson and H. G. Wood, "Solution of the Pancake Model for Flow in a Gas Centrifuge by Means of a Temperature Potential," *Comput. Methods Appl. Mech. Engrg.,* vol. 178, pp. 183-97, 1999.

[42] W. C. Witt, "The Onsager Equation with Curvature and Source Terms: A Finite Element Solution," University of Virginia, Charlottesville, VA, 2013.

[43] B. R. Thomas, W. C. Witt, W. Paudel and H. G. Wood, "A Finite Element Solution to the Generalized Onsager Model of Fluid Flow in a Countercurrent Gas Centrifuge," *Journal of Separation Science and Technology,* 2019.

[44] S. H. Maslen, "The Basic Steady State Flow Models for Computing Countercurrent Motions, UVA-ER-540-80U," University of Virginia, Charlottesville, VA, 1979.

[45] S. H. Maslen, "On the Differential Equations for the Gas Centrifuge, UVA-ER-766-82U," University of Virginia, Charlottesville, VA, 1982.

[46] H. G. Wood, "Analysis of Feed Effects on a Single-Stage Gas Centrifuge Cascade," *Separation Science and Technology,* vol. 30, no. 13, pp. 2631-2657, 1995.

[47] H. G. Wood, T. C. Mason and Soubbaramayer, "Multi-isotope Separation in a Gas Centrifuge Using Onsager's Pancake Model," *Separation Science and Technology,* vol. 31, no. 9, pp. 1185-1213, 1996.

[48] T. Kai, "Basic Characteristics of Centrifuges (IV) - Analysis of Separation Performance," *J. Nucl. Sci. Technol.,* vol. 14, p. 506, 1977.

[49] H. Makihara and T. Ito, "Separation Characteristics of Gas Centrifuges," *Journal of Nuclear Science and Technology,* vol. 25, no. 8, pp. 649-660, August, 1988.

[50] W. L. Roberts, "Gas Centrifugation of Research Isotopes," *Nucl. Instrum. Methods Phys. Res.,* vol. A282, pp. 271-276, 1989.

[51] A. J. Szady, "Enrichment of Chromium Isotopes by Gas Centrifugation," *Ibid,* vol. A282, pp. 277-280, 1989.

[52] H. G. M. Harink-Snijers, "Solving the Diffusion Equation for Multi-Isotope Mixtures," in *Proceedings of the Third Workshop on Separation Phenomena in Liquids and Gases*, Charlottesville, VA, 1992.

[53] C. Ying and Z. Guo, "Some Characteristics for MultiComponent Isotope Separation," in *Proceedings of the Fourth Workshop on Separation Phenomena in Liquids and Gases*, Beijing, China, 1995.

[54] E. V. Levin and C. Ying, "Diffusion Transport Vector for Multicomponent Gas Separation in Ultracentrifuge," *Sep. Sci. Technol.,* vol. 30, no. 18, pp. 3445-3458, 1995.

[55] C. Ying, Z. Guo and H. Wood, "Solution of the Diffusion Equations in a Gas Centrifuge for Separation of Multicomponent Mixtures," *Separation Science and Technology,* vol. 31, no. 18, pp. 2455-2471, 1996.

[56] E. Von Halle, "MultiComponent Isotope Separation in Matched Abundance Ratio Cascades Composed of Stages with Large Separation Factors," in *Workshop on Separation Phenomena in Liquids and Gases*, Darmstadt, Germany, 1987.

[57] P. Migliorini, "Modeling and Simulation of Gas Centrifuge Cascades for Enhancing the Efficiency of IAEA Safeguards, PhD Dissertation," University of Virginia , Charlottesville, VA, 2013.

[58] W. Paudel and H. Wood, "The Effect of Source Function Types on Mass Flow and Isotopic Distribution Inside a Gas Centrifuge," in *Proceedings of the INMM & ESARDA Joint Virtual Annual Meeting*, 2021.

[59] "The Rome Machine, definition," in *Proceedings of the Fifth Workshop on Gases in Strong Rotation*, University of Virginia, Charlottesville, VA, June 1983.

[60] Instituto Nacional de Pesquisas Espaciai, "The Iguassu Machine," in *Fifth Workshop Proceedings Separation Phenomena in Liquids and Gases*, Foz do Iguacu, Brasil, 1996.

[61] W. Paudel and H. Wood, "Two Dimensional Multi-Isotope Separation in a Gas Centrifuge Using Finite Element Analysis," *Journal of Physics: Conf. Ser,* vol. 2147, no. 1, p. 012001, 2022.

[62] "The Rome Machine, augumentation," in *Fourth Workshop on Gases in Strong Rotation*, Oxford, England, August 1981.

[63] "Darmstadt Extension of the Rome Model Centrifuge (1987)," in *Workshop on Separation Phenomena in Liquids and Gases*, Darmstadt, Germany, 1987.

[64] "Standard Specification for Uranium Hexafluoride for Enrichment," ASTM International, West Conshohocken, PA, 2006.

[65] S. Marelli and B. Sudret, "UQLab: A framework for uncertainty quantification in Matlab," in *Proc. 2nd Int. Conf. on Vulnerability, Risk Analysis and Management (ICVRAM2014)*, Liverpool, United Kingdom, 2014.

[66] W. J. Bohnhoff, K. R. Dalbey, M. S. Ebeida, J. P. Eddy, P. D. Hough, M. Khalil, K. T. Hu, E. M. Ridgway, D. M. Vigil and J. G. Winokur, "Dakota, A Multilevel Parallel Object-Oriented Framework for Design Optimization, Parameter Estimation, Uncertainty Quantification, and Sensitivity Analysis," Sandia National Laboratories, Albuquerque, NM, 2019.

[67] W. L. Oberkampf and C. J. Roy, "Historical and modern role of modeling and simulation," in *Verification and Validation in Scientific Computing*, Cambridge, UK, Cambridge University Press, 2010, pp. 1-15.

[68] W. Paudel and H. Wood, "Two Dimensional Multi-Component Separation in a Gas Centrifuge Using Finite Element Model," *J. of Physics: Conference Series,* 2021 (In progress).

[69] S. Kemp, "Gas Centrifuge Theory and Development: A Review of U.S. Programs," *Science and Global Security,* vol. 17, pp. 1-19, 2009.

[70] S. Marelli, N. Luthen and B. Sudret, "UQLab user manual- Polynomial chaos expansions," Zurich, Switzerland, 2021.

[71] I. M. Sobol, "Sensitivity Estimates for Nonlinear Mathematical Models," *Mathematical and Computer Modelling ,* vol. 1, no. 4, pp. 407-414, 1993.

[72] S. Marelli, C. Lamas, K. Konakli, C. Mylonas, P. Wiederkehr and B. Sudret, "UQLab user manual - Sensitivity analysis," Zurich, Switzerland, 2021.

[73] B. Sudret, "Global Sensitivity Analysis Using Polynomial Chaos Expansions," *Reliability Engineering & System Safety,* vol. 93, no. 7, pp. 964-979, 2008.

[74] K. Konakli, C. Mylonas, S. Marelli and B. Sudret, "UQLab user manual-Canonical low-rank approximations," Zurich, Switzerland, 2021.

[75] International Atomic Energy Agency, "IAEA Nuclear Energy Series: International Safeguards in the Design of Enrichment Plants," IAEA, Vienna, Austria, 2019.

[76] International Atomic Energy Agency, "Strengthening the Effectiveness and Improving the Efficiency of the Safeguards System," IAEA, Vienna, Austria, 1995.

[77] International Atomic Energy Agency, "Environmental Sampling for Safeguards: STR-348 (revision 1)," IAEA, Vienna, Austria, 2011.

[78] M. Rosenthal and W. M. Stern, Deterring Nuclear Proliferation: The Importance of IAEA Safeguards, 2nd ed., Brookhaven, NY: Brookhaven Science Associates, LLC, April 2019, pp. 109-111.

[79] International Atomic Energy Agency, "How Environmental Sampling Helps Verify the Peaceful Use of Nuclear," 22 September 2021. [Online]. Available: https://www.iaea.org/newscenter/news/how-environmental-sampling-helps-verify-the-peaceful-use-of-nuclear. [Accessed 2022].

[80] W. Bush, G. af Ekenstam, J. Janov, E. Kuhn and M. Ryjinski, "IAEA Experience with Environmental Sampling at Gas Centrifuge Enrichment Plants in the European Union," IAEA, Vienna, Austria, 2001.

[81] D. Fischer and M. Ryzhinskiy, "Safeguards Environmental Sampling Signatures: Comparison of Two Enrichment Scenarios," in *Institute of Nuclear Materials Management (INMM)*, Nashville, TN, July 2006.

[82] D. Starr, "MSTAR-IAEA Enrichment Code User Guide," National Security Program Office, Oak Ridge K-25 Site, June 1996.

[83] P. Migliorini and H. Wood, "Transient Fluid Dynamics Modeling of Gas Centrifuge Enrichment Plants," in *Proceedings of the 52nd Annual Meeting of the Institute of Nuclear Material Management*, Palm Desert, CA, 2011.

[84] P. Migliorini and H. Wood, "Tranient Isotope Separation Modeling of Gas Centrifuge Enrichment Plants," in *Proceedings of the 53rd Annual Meeting of the Institute of Nuclear Material Management*, Orlando, FL, 2012.

[85] "Centrus Energy Corp. (formerly USEC Inc.) Gas Centrifuge Enrichment Facility Licensing," U.S. Nuclear Regulatory Commission (NRC), May 2021. [Online]. Available: https://www.nrc.gov/materials/fuel-cycle-fac/usecfacility.html#high. [Accessed December 2021].

[86] A. S. Krass, P. Boskma, B. Elzen and W. A. Smit, "Chapter 5. General principles of uranium enrichment," in *Uranium Enrichment and Nuclear Weapon Proliferation*, Taylor & Francis Ltd, 1983, pp. 96-98.

[87] K. Cohen, "The Theory of Isotope Separation as Applied to the Large-Scale Production of U-235," *National Nuclear Energy Series Division III,* vol. 1B, 1951.

[88] J. Schacter, R. L. Hoglund and E. Von Halle, "Diffusion Separation Methods," *Encyclopedia of Chemical Technology,* vol. 7, p. 91, 1965.

[89] B. Brigoli, "Cascade Theory," in *Uranium Enrichment*, S. Villani, Ed., New York, Springer-Verlag, 1979, pp. 13-54.

[90] E. Von Halle, "Cascade Design Considerations for Cascades Composed of Stages with Large Separation Factors," Oak Ridge Gaseous Diffusion Plant, Oak Ridge, TN, 1978.

[91] E. Von Halle, "Stage Separation Theory," in *Von Karman Institute of Fluid Dynamics 1977-1978 Lecture Series on Aerodynamic Separation on Gases and Isotopes*, 1977.

[92] P. Migliorini and H. Wood, "A Study of Multicomponent Streams in Off-Design Centrifuge Cascades," *Separation Science and Technology,* vol. 47, no. 7, pp. 921-928, 2012.

[93] D. Fischer and M. Ryzhinskiy, "Safeguards Environmental Sampling Signatures: Comparison of Two Enrichment Scenarios," in *Proceedings of the Institute of Nuclear Materials Management (INMM) Annual Meeting*, Nashville, TN, July 2006.

[94] "ASTM C 787-06: Standard Specification for Uranium Hexafluoride for Enrichment," ASTM International.

APPENDIX I: Weak form derivation of the diffusion equation

Multiply Equation. (4.1) by any arbitrary weighting function, $w(r,z)$ and integrate the product over the domain.

$$\iint w(r,z) * \left(-\rho D * \frac{\partial^2 N_k}{\partial z^2} - \rho D \frac{1}{r} * \frac{\partial}{\partial r}\left[r * \frac{\partial N_k}{\partial r} - \frac{\Omega^2 r^2}{RT}\left(M_k - \sum_{j=1}^{n} M_j N_j\right) N_k\right] + \frac{\rho V_z \partial N_k}{\partial z} = 0\right) \mathrm{rdrdz} = 0$$

i) Conduct integration by parts with respect to *z* for the first term in the integral

$$\iint_{r=0,z=0}^{r=a,z=z_H} w(r,z) * \left(-\rho D * \frac{\partial^2 N_k}{\partial z}\right) r\,dr\,dz \tag{4.1.1}$$

$$Let\ u = w \qquad\qquad dv = -\rho D * \left(\frac{\partial^2 N_k}{\partial z^2}\right) dz$$

$$du = dw \qquad\qquad v = -\rho D * \left(\frac{\partial N_k}{\partial z}\right)$$

$$\int_0^a (w * -\rho D * \frac{\partial N_k}{\partial z} \Big|_0^{z_H} - \int_0^{z_H} -\rho D * \frac{\partial N_k}{\partial z} * \frac{\partial w}{\partial z} dz)\, rdr \tag{4.1.2}$$

Rewriting the double and single integrals separately in (4.1.2) yields

$$-\iint_{z=0,r=0}^{z=z_H,r=a} -\rho D * \frac{\partial N_k}{\partial z} * \frac{\partial w}{\partial z}\, rdrdz + \int_0^a \left(w * -\rho D * \frac{\partial N_k}{\partial z}\Big|_0^{z_H}\right) rdr \tag{4.1.3}$$

ii) Conduct integration by parts with respect to *r* for the second term in the integral in Equation. (4.1)

$$\iint_{r=0,z=0}^{r=a,z=z_H} w(r,z) * (-\rho D \left(\frac{1}{r}\right)\left(\frac{\partial}{\partial r}\right)[r * \frac{\partial N_k}{\partial r} - \frac{\Omega^2 r^2}{RT} * (M_k - \sum_{j=1}^{n} M_j N_j) * N_k])\, rdrdz \tag{4.1.4}$$

$$u = w \qquad\qquad du = dw$$

$$dv = -\rho D * \frac{1}{r} * \frac{\partial}{\partial r}[r * \frac{\partial N_k}{\partial r} - \frac{\Omega^2 r^2}{RT} * (M_k - \sum_{j=1}^{n} M_j N_j) * N_k]\, rdr$$

$$v = -\rho D * \left[r * \frac{\partial N_k}{\partial r} - H_k * r^2 * N_k\right], where\ H_k = \frac{\Omega^2}{RT}(M_k - \sum_{j=1}^{n} M_j N_j) N_k]\, rdr$$

$$\int_{z=0}^{z=z_H} (w * -\rho D \left[r * \frac{\partial N_k}{\partial r} - H_k * r^2 N_k\right] \Big| \begin{matrix} r = a \\ r = 0 \end{matrix} - \int_{r=0}^{r=a} -\rho D * \left[\frac{\partial N_k}{\partial r} - H_k * r * N_k\right] * dw * rdr)\, dz \quad (4.1.5)$$

$$- \iint\limits_{z=0,r=0}^{z=z_H,r=a} -\rho D * \left[\frac{\partial N_k}{\partial r} - H_k r N_k\right] dw\, rdr\, dz + \int_{z=0}^{z=z_H} \left(w * -\rho D * \left[r * \frac{\partial N_k}{\partial r} - H_k * r^2 N_k\right]\right) \Big| \begin{matrix} r = a \\ r = 0 \end{matrix} dz \ (4.1.6)$$

Using the radial boundary conditions at $r = 0\ and\ r = a$, it can be shown that the single integral in Equation. (4.1.6) goes to zero:

$$w(a,z) * -\rho D * \left[a * \frac{\partial N_k}{\partial r} - H * a^2 N_k\right] - w(0,z) * -\rho D * \left[0 * \frac{\partial N_k}{\partial r} - H * (0)^2 * N_k\right] \qquad (4.1.6.1)$$

$$\rightarrow w(a,z) * -\rho D * a * [\frac{\partial N_k}{\partial r} - \frac{\Omega^2 a}{RT} * (M_k - \sum_{j=1}^{n} M_j N_j) * N_k] \ = 0 \ \ from\ Eq. 7\ at\ r = a \qquad (4.1.6.2)$$

iii) Finally conduct integration by parts with respect to *z* on the third term in the integral in Equation. (4.1)

$$\iint\limits_{z=0,r=0}^{z=z_H,r=a} w(r,z) * \left(\rho V_z * \frac{\partial N_k}{\partial z}\right) rdrdz \qquad (4.1.7)$$

$$u = w \qquad dv = \rho V_z \left(\frac{\partial N_k}{\partial z}\right) dz$$

$$du = dw \qquad v = \rho V_z * N_k$$

$$\int_{r=0}^{r=a} (w * \rho V_z * N_k \Big| \begin{matrix} z = z_H \\ z = 0 \end{matrix} - \int_{z=0}^{z=z_H} \rho V_z * N_k * \frac{dw}{dz} dz\ )\ r\ dr \qquad (4.1.8)$$

$$- \iint\limits_{z=0,r=0}^{z=z_H,r=a} \rho V_z * N_k * \frac{dw}{dz}\ \ rdrdz + \int_{r=0}^{r=a} (w * \rho V_z * N_k) \Big| \begin{matrix} z = z_H \\ z = 0 \end{matrix} rdr \qquad (4.1.9)$$

Now combining all of the double integrals first followed by the boundary terms leads to the following:

$$- \iint\limits_{z=0,r=0}^{z=z_H,r=a} -\rho D * \frac{\partial N_k}{\partial z} * \frac{\partial w}{\partial z}\ rdrdz\ - \iint\limits_{z=0,r=0}^{z=z_H,r=a} -\rho D * \left[\frac{\partial N_k}{\partial r} - H_k r N_k\right] dw\, rdr\, dz$$

$$- \iint\limits_{z=0,r=0}^{z=z_H,r=a} \rho V_z * N_k * \frac{dw}{dz}\ \ rdrdz + \int_0^a (w * -\rho D * \frac{\partial N_k}{\partial z} \Big|_0^{z_H} rdr$$

$$+ \int_{r=0}^{r=a} (w * \rho V_z * N_k) \Big| \begin{matrix} z = z_H \\ z = 0 \end{matrix} rdr = 0 \qquad (4.1.10)$$

Eq. (6.10) can be further simplified into:

$$\iint\limits_{z=0,r=0}^{z=z_H,r=a} -\rho D\frac{\partial N_k}{\partial z}*\frac{\partial w}{\partial z}-\rho D*\frac{\partial N_k}{\partial r}*\frac{\partial w}{\partial r}+\rho D*H_k r N_k*\frac{\partial w}{\partial r}+\rho V_z*N_k*\frac{\partial w}{\partial z}\;rdrdz$$

$$=\int\limits_{r=0}^{r=a}\left(w(r,z_H)*-\rho D*\frac{\partial N_k(r,z)}{\partial z}-w(r,0)*-\rho D*\frac{\partial N_k(r,0)}{\partial z}\right)rdr + \int\limits_{r=0}^{r=a}\big(w(r,z_H)*\rho V_z*N_k(r,z_H)-w(r,0)*\rho V_z*N_k(r,0)\big)\,rdr \tag{4.1.11}$$

Eq. (4.1.11) is equivalent to Eq. (4.9) with the right-hand side equal to zero. The detailed evaluation of the right-hand side of Equation. (4.1.11) is as follows:

1) Combine the terms related to the top and the bottom boundaries together

$$\int\limits_{r=0}^{r=a} w(r,z_H)*\left(-\rho D*\frac{\partial N_k(r,z_H)}{\partial z}+\rho V_z N_k(r,z_H)\right)rdr + \int\limits_{r=0}^{r=a} -w(r,0)*\left(-\rho D*\frac{\partial N_k(r,0)}{\partial z}+\rho V_z N_k(r,0)\right)rdr \tag{4.1.12}$$

Equation. (4.1.12) is simply a combination of the end boundary conditions given by Equations. (4.1.9) and (4.1.10) multiplied by the weighting function at each end. The first integral in (4.1.12) can be evaluated using integration by parts as follows:

Let, $u=w(r,z_H)$ $\qquad dv=\left(-\rho D*\frac{\partial N_k(r,z_H)}{\partial z}+\rho V_z*N_k(r,z_H)\right)rdr$

$du=\frac{dw(r,z_H)}{dr}$ $\qquad v=\int_0^a\left(-\rho D*\frac{\partial N_k(r,z_H)}{\partial z}+\rho V_z*N_k(r,z_H)\right)rdr=\frac{F\theta N_{P,k}}{2\pi}$

$$\left(w(r,z_H)\left(\frac{F\theta N_{P,k}}{2\pi}\right)\Big|\begin{matrix}r=a\\r=0\end{matrix}\right)-\int\limits_{r=0}^{r=a}\left(\frac{F\theta N_{P,k}}{2\pi}\right)*\frac{dw(r,z_H)}{dr}rdr \tag{4.1.13}$$

$$\rightarrow\left(\left(\frac{F\theta N_{P,k}}{2\pi}\right)*w(a,z_H)-w(0,z_H)\right)-\left(\frac{F\theta N_{P,k}}{2\pi}*w(r,z_H)\Big|\begin{matrix}r=a\\r=0\end{matrix}\right) \tag{4.1.14}$$

$$\rightarrow\left(\frac{F\theta N_{P,k}}{2\pi}\right)*\big(w(a,z_H)-w(0,z_H)\big)-\left(\frac{F\theta N_{P,k}}{2\pi}*\big(w(a,z_H)-w(0,z_H)\big)\right)=0 \tag{4.1.15}$$

Similarly, the second integral in (4.1.12) can be evaluated as:

Let, $u=-w(r,0)$ $\qquad dv=\left(-\rho D*\frac{\partial N_k(r,0)}{\partial z}+\rho V_z*N_k(r,0)\right)rdr$

$$du = -\frac{dw(r,0)}{dr} \qquad\qquad v = \int_{0}^{a} \left(-\rho D * \frac{\partial N_k(r,0)}{\partial z} + \rho V_z * N_k(r,0)\right) r dr = \frac{-F(1-\theta) * N_{w,k}}{2\pi}$$

$$\left(-w(r,0)\left(\frac{-F(1-\theta) * N_{w,k}}{2\pi}\right)\Big|\begin{matrix} r=a \\ r=0 \end{matrix}\right) - \int_{r=0}^{r=a} \left(\frac{-F(1-\theta) * N_{w,k}}{2\pi}\right) * -\frac{dw(r,0)}{dr} r dr \qquad (4.1.16)$$

$$\rightarrow \left(\left(\frac{-F(1-\theta) * N_{w,k}}{2\pi}\right) * \left(-w(a,0) + w(0,0)\right)\right) - \left(\frac{-F(1-\theta) * N_{w,k}}{2\pi} * \left(-w(r,0)\right)\Big|\begin{matrix} r=a \\ r=0 \end{matrix}\right) \quad (4.1.17)$$

$$\rightarrow \left(\left(\frac{-F(1-\theta) * N_{w,k}}{2\pi}\right) * \left(-w(a,0) + w(0,0)\right)\right) - \left(\frac{-F(1-\theta) * N_{w,k}}{2\pi}\right) * \left(-w(a,0) + w(0,0)\right) = 0 \qquad (4.1.18)$$

Therefore, both integrals in Equation. (4.1.11) are evaluated to zero using the top and bottom boundary conditions in the centrifuge domain. This completes the check for the derivation of Equation. (4.9).

$$\iint_{r=0,z=0}^{r=a,z=z_H} \frac{\partial N_k}{\partial z} * \frac{\partial w}{\partial z} + \frac{\partial N_k}{\partial r} * \frac{\partial w}{\partial r} - \frac{\Omega^2}{RT}\left(M_k - \sum_{j=1}^{n} M_j N_j\right) * r^2 N_k \left(\frac{\partial w}{\partial z}\right) - \frac{\rho V_z}{\rho D}\left(\frac{\partial w}{\partial z}\right) N_k r \, dr \, dz = 0$$

APPENDIX II: Flowchart describing the execution of *MultiPort*

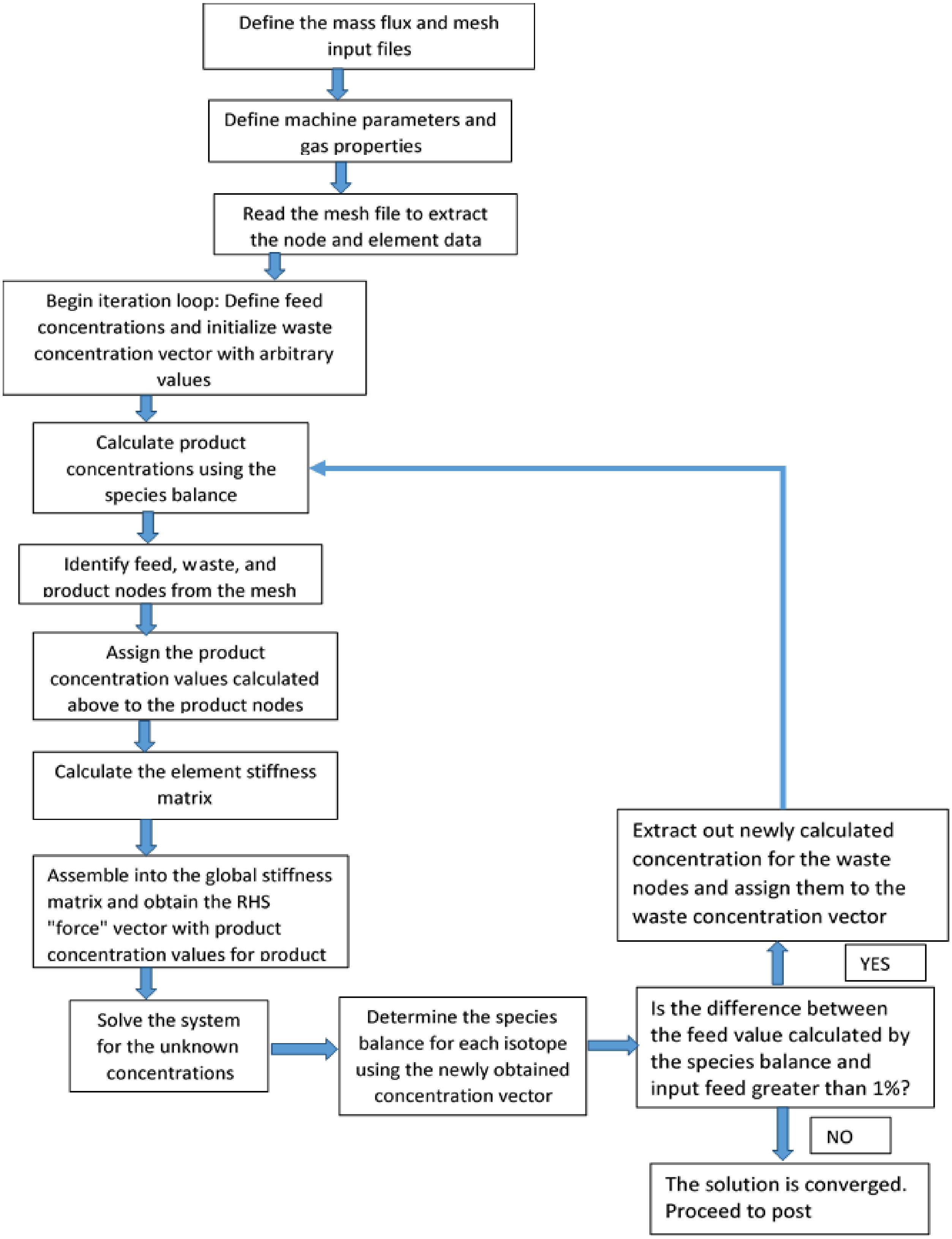

APPENDIX III: Sensitivity Analysis and Uncertainty Quantification Results for Rome

Table III.0.1: Range of independent parameter values used in the simulations of the Rome centrifuge

Parameter	Description	Lower bound	Nominal	Upper bound
ω	Rotor speed (m/s)	480	600	720
T	Temperature at the wall (K)	270	320	384
θ	Machine cut-product flow rate/ feed flow rate (non-dim)	0.4	0.5	0.6
k	Thermal conductivity (W/(m*K))	5.435E-3	6.794E-3	8.135E-3
Sc	Schmidt number (non-dim)	0.64	0.8	0.96
F	Feed rate (mgU/s)	56	70	84
ΔT	Temperature gradient (K)	5.58	6.97	8.36
D_{scoop}	Drag force exerted by the scoop on the rotating gas (Dynes)	1600	2000	2400

Table III.0.2: Few of the 80 randomized simulations developed using LHS for the above described range

Sim	ω	T_{wall}	θ	k	Sc	F	ΔT	D_{scoop}
1	659.270	332.075	0.518	0.00691	0.723	80.197	7.627	2199.545
2	632.208	328.859	0.513	0.00551	0.746	74.217	7.414	1827.314
3	641.926	333.603	0.524	0.00649	0.776	75.587	7.069	1942.607
4	621.837	326.497	0.410	0.00705	0.664	77.545	6.776	2154.171
5	574.703	275.750	0.467	0.00670	0.929	68.874	6.454	1675.726
6	567.763	348.519	0.485	0.00612	0.660	63.649	6.897	1669.975
7	677.898	382.323	0.441	0.00799	0.758	75.712	7.856	1784.664
8	543.090	306.643	0.535	0.00758	0.903	81.168	7.895	1985.934
9	676.76	379.391	0.568	0.00766	0.739	71.177	7.216	2352.904
10	662.878	305.692	0.449	0.00615	0.841	58.907	7.818	2127.45
:	:	:	:	:	:	:	:	:
80	516.198	329.559	0.459	0.00803	0.643	61.517	6.052	1719.887

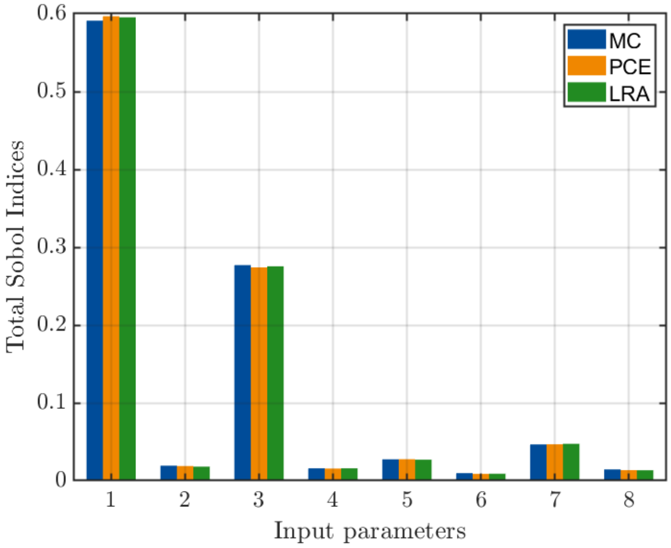

Figure III.1: Sensitivity indices for Rome simulations with uniform input parameter distributions set at +/- 20% off the nominal values

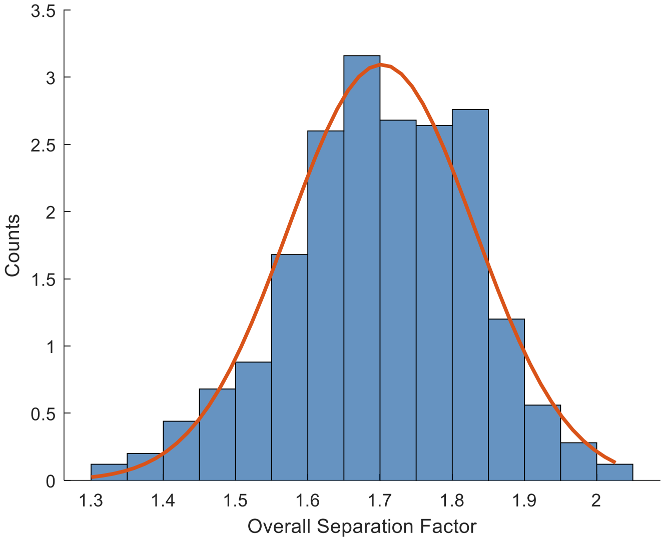

Figure III.1: Probability distribution of the overall separation factor for Rome machine with input parameters uniformly distributed within +/-20% of their respective nominal values

Table III.0.3: Statistical moments for the output function distribution for Rome simulations with uniform input distributions

Statistical Moments	Values
Mean	1.70203
Standard deviation	0.12894
Kurtosis	2.9865
Skewness	-0.30328

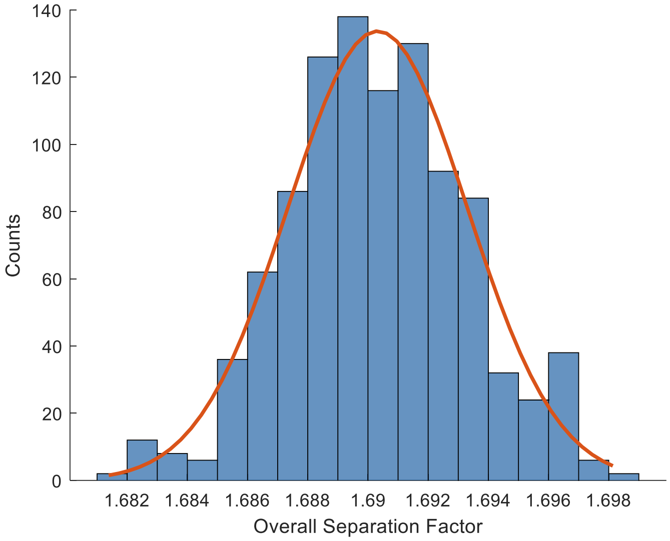

Figure III.2: Probability distribution of the overall separation factor for Rome machine with input parameters ranging within 1% of their respective nominal values

Table III.0.4: Statistical moments for the output function distribution for Rome simulations corresponding to Figure III.2

Statistical Moments	**Values**
Mean	1.6903
Standard deviation	0.002983
Kurtosis	3.00336
Skewness	0.03467